TELESEISMICALLY DETERMINED SOURCE PARAMETERS OF SEVERAL LARGE COLLISION-ZONE EARTHQUAKES

Thesis by

Lorraine J. Hwang

In Partial Fulfillment of the Requirements

for the Degree of

Doctor of Philosophy

California Institute of Technology

Pasadena, California

1991

(Submitted November 21, 1990)

Acknowledgements

Early on, I had the good fortune of working with two crazy Irishmen. Hectic summers in the field working with Walter Mooney's group was equally matched by the exasperation of classes during the school year in which I worked with Tom McEvilly. I am grateful to both for introducing and encouraging me to continue in the field. Their friendship and words of wisdom have meant much these past few years.

Coming to Caltech, I met many people who helped to make the stay more pleasant. Luciana Astiz was always a positive influence both as a roommate and as a colleague. Those who kept the computers running in the early years — John Louie, Richard Stead and Christof Stork, are as much appreciated as the current system manager, Doug Neuhauser. Mindy Brugman showed me some of the nicer trails in the San Gabriel Mountains. Skiing and sailing with Christof Stork always brought on an incredible adrenalin rush. Classmates Scott, Tom, Mike, and Alison were always there to commiserate over classes. Many enjoyable hours were spent on the court with the Seismo volleyball crowd — L. Astiz, R. and J. Graves, P. Ho-Liu, H. Kawakatsu, H. Magistrale, C. Sanders, R. Stead, C. Stork, J. Vidale, and H.W. Zhou. Jaye and Craig supplied the tape and expertise to keep me in one piece, along with their endless banter in the training room.

Lastly, thanks go to José for his love and support over the past year.

This work was supported by USGS Grant No. 14-08-0001-G1170 and by an NSF Graduate Fellowship.

To my mother and posthumously to my father, both of whom have always been proud of the accomplishments of all of their children.

TELESEISMICALLY DETERMINED SOURCE PARAMETERS OF SEVERAL LARGE COLLISION-ZONE EARTHQUAKES

Lorraine J. Hwang, Ph.D.

California Institute of Technology 1991

Understanding earthquake hazards begins with the understanding of the earthquake process itself and its effects in the near source region. Here both ends of the problem are explored. First, source parameters and rupture models for several earthquakes around the circum-Pacific are studied. Second, acceleration spectra are compared to teleseismic data. It is hoped that the extensive teleseismic data base can be used to scale acceleration spectra for large future, earthquakes.

The 7 May 1986 Andreanof Islands earthquake was a large (1.3×10^{28} dyne-cm) thrust event (strike 257°, dip 18°, rake 116°) that ruptured a 220 km segment of the Aleutian Arc. The earthquake ruptured bilaterally with the largest moment releasing subevent nucleating 75–90 km west of the epicenter in a region of low aftershock seismicity. At a distance of 100 km, the acceleration spectrum had the same amplitude as that from teleseismic data.

The 20 May (6.4 M_s, NEIC) and 14 November (7.3 M_s, 1.7×10^{27} dyne-cm) 1986 Hualien earthquakes occurred on two steeply dipping, reverse faulting events

near the Eurasian-Philippine Sea plate boundary. The amplitude of the observed spectra at a distance of 70–80 km is 5 times that from teleseismic data. This is consistent with previous observations. Comparisons between hard and soft rock recording sites indicate that the alluvial valley amplified the strong ground motion between 0.15–1.8 Hz.

The 24 November 1987 Superstition Hills earthquake (8×10^{25} dyne-cm) consisted of two spatially distinct subevents with different focal mechanisms at depths between 4 to 8 km. Rupture models along with aftershock, afterslip and geologic data suggest that the northern and southern segments of the Superstition Hills fault behaved differently during this event.

The 1987-88 Gulf of Alaska earthquake sequence consisted of three large, intraplate, strike-slip earthquakes (7.2, 7.8, 7.7 M_w), whose depths extended to 25 km. The data are modeled with multiple subevents with different focal mechanisms. In comparison with other large events, the short durations and rupture lengths of the two largest events illustrate the difference in strength between oceanic and continental lithosphere. Moment release is confined to the epicentral region and/or regions of apparent structural complexities where seismicity trends intersect.

Table of Contents

List of Tables

List of Figures

Chapter 1

Introduction to the Thesis

One of the fundamental goals of seismology is the mitigation of earthquake hazards. Earthquakes have both a major economic and social cost. In the last several years, billions of dollars of damage were done and thousands of lives were lost and many more lives disrupted by major earthquakes. In order to protect both lives and property effectively, the basic properties of an expected earthquake and its associated strong ground motion must be understood. If we knowthe magnitude, focal mechanism, and moment distribution along the fault as well as the crustal structure along the path of propagation, strong ground motion at a particular site can theoretically be modeled. Unfortunately, these parameters are often poorly known.

Studying past earthquakes gives some insight into what to expect in future earthquakes. Here the emphasis is twofold: first, on the analysis of source properties of several moderate to large recent earthquakes along the circum-Pacific as determined from inversions of body-wave seismograms and their relationship to regional tectonics; and second, on the estimation of strong ground motion from teleseismic

observations.

In the past few decades, advances in theory and computation of seismic sources have greatly improved the ability to model earthquake source parameters. First motion analyses have been augmented by waveform-modeling techniques. Current methods can be classified as *forward* or *inverse* and *frequency* or *time* domain methods. Forward modeling methods, i.e., Langston and Helmberger (1975), depend on *a priori* observations about the source based on first-motion data and aftershock patterns. However, if the focal mechanism varies with time, both first-motion data and aftershock distribution can be misleading. Frequency-domain methods, i.e., Dziewonski *et al.* (1981), invert for the centroidal properties of the source over the duration of the event. This yields the best point-source description of the source. For finite sources, inverse time-domain methods, i.e., Nábělek (1984,1985), Kikuchi and Fukao (1985), and Kikuchi and Kanamori (1990), can be used to describe both spatial and temporal variations of the source. In general, large earthquakes involve large source areas that do not rupture smoothly in time. Multiple subevents with the same or different focal mechanism may be needed to model the data. Hence, the inverse time-domain methods are primarily used here to investigate the time variations of both the focal mechanism and the moment distribution in the rupture area.

A description of the source is only part of the information needed to model strong ground motion. To describe the problem completely, path and site effects must also be known. One way to characterize them is by modeling the local crustal structure but unfortunately, this is often not known well enough for many sites. The

alternative approach explored here is to use teleseismic data to scale strong ground motion. Since few, strong ground-motion recordings exist for large earthquakes, teleseismic recordings provide an invaluable data base. The use of teleseismic records to estimate the strong-motion spectra has been previously investigated by Houston and Kanamori (1990), who showed that a relationship can be developed between the amplitude of the observed and teleseismic reference spectra. Several of the following chapters build on their work.

The earthquakes examined here are the result of collision between the Pacific and North American or Eurasian plates. Of the four events, only the 1985 Andreanof Islands earthquake lies directly on the plate boundary. The remaining events — the 1986 Hualien, 1987 Superstition Hills, and the 1987-88 Gulf of Alaska earthquakes, do not lie on major plate boundaries but along related structures. Both the 1986 Hualien and 1987 Superstition Hills earthquakes occurred on structures that lie parallel to the major plate boundary while the 1987-88 Gulf of Alaska earthquakes are classified as intraplate events. However, the Gulf of Alaska earthquakes are the result of regional stresses that are due to collision and subduction of the Pacific plate, and possibly represent fragmentation of the oceanic plate as the plate margin moves outboard of the continental margin (Lahr *et al.,* 1988).

The earthquakes studied here can also be grouped into *reverse* and *strike-slip* type events whose waveforms have different characteristics. Reverse-type events often have waveforms with simple impulsive shapes that change slowly with azimuth. Even though the source mechanism may change with time during the event, only one mechanism is necessary to model the data. On the other hand, waveforms from strike-

slip type events often have emergent beginnings and change rapidly with azimuth. These events are difficult to model because of their sensitivity to small changes in the focal mechanism and local heterogeneities in the crustal structure. The study of strike-slip earthquakes is important in understanding the behavior of future great earthquakes along the San Andreas fault.

The next two chapters examine source properties of two reverse-faulting events. The last two chapters examine four, large, strike-slip earthquakes, the difficulties in modeling this type of event, and resolutions of different methods and data sets.

In Chapter 2, the 1986 Andreanof Islands earthquake (M_w 8.0) has a very complex waveform of long duration. The long-period data can be easily modeled using a simple thrust faulting mechanism along a fault with multiple asperities. As seen later, strike-slip earthquakes of comparable complexity require source models that are more complex. Since this study was published (Hwang and Kanamori, 1986), several authors have also analyzed this event. Their studies, using different methods and data sets, are in good agreement with the results presented here (Boyd and Nábělek, 1988; Houston and Engdahl, 1989; Das and Kostrov, 1990).

In Chapter 3, only the larger of the two 1986 Hualien earthquakes is modeled. The 14 November 1986 Hualien earthquake (M_s 7.3) has a much simpler waveform than the 1986 Andreanof Islands earthquake. The data are modeled using a steeply dipping, reverse-faulting mechanism along a fault with one major asperity. In addition, this chapter explores how teleseismic observations for both the 20 May and 14 November events may be used to scale strong ground motion. Since strong ground-motion observations near the fault plane of large earthquakes are not common, comparison

between the observed acceleration spectra and the reference spectra calculated from teleseismic observations can further our understanding of expected strong ground motion in regions where no such records exist. Strong ground motion data for these events also illustrate the importance of local crustal structure on the observed strong ground-motion spectra.

Chapter 4 examines the 1987 Superstition Hills earthquake (M_s 6.6). This is a well-studied event that occurred in a heavily monitored region of Southern California. Arrays recorded strong ground motion and aftershocks, and accessibility to the region allowed detailed study of the surface rupture and afterslip of the event. This information is used to constrain the source dimensions of the model in the waveform inversions. The waveforms appear very simple at many stations; however, two subevents with different strike-slip focal mechanisms are needed to model the waveforms. Afterslip measurements, aftershock activity, local subsurface geology, strong motion and teleseismic models concur that the northern and southern segments of the Superstition Hills fault behaved differently during this event.

Chapter 5, the 1987-88 Gulf of Alaska sequence, is comprised of three complex events in a region with no previous record of seismic activity. Unlike the 1987 Superstition Hills event, not much is known about the region. The region is inaccessible to most routine observations since it is located offshore where the water depth is greater than 3 km. In addition, it is poorly covered by both geodetic and seismic arrays. Hence, not much is known about slip in the epicentral region, depth of seismicity, and absolute locations for the aftershock sequence. Teleseismic observations give the best clues to what occurred during this event. Even though teleseismic source

models are not robust, the following analyses illustrate why strike-slip earthquakes can be difficult to model.

The following chapters embrace several research projects. Chapters 2-4 have already been published (Hwang and Kanamori, 1986; Hwang and Kanamori, 1987; Hwang and Kanamori, 1989; and Hwang *et al.,* 1990). Chapter 5 is also designed as a separate paper. Hence, some redundancies exist between the chapters.

Chapter 2

The May 7, 1986 Andreanof Islands Earthquake

Abstract

Source characteristics of the May 7, 1986 Andreanof Islands earthquake (51.412°N, 174.830°W, NEIC) are investigated from WWSSN, GDSN and IDA records. First motions from over 60 stations determine one steeply dipping nodal plane. We constrained this nodal plane and inverted long-period surface waves at a period of T=256 sec and determined the second nodal plane to be dip 18°, rake 116°, and strike 257°. This shallowly dipping, thrust mechanism is consistent with plate motions in the region. The seismic moment from surface-wave inversion is 1.3×10^{28} dyne-cm, corresponding to $M_w = 8.0$. Amplitudes of body and surface waves from short-period instruments yield magnitudes of $\hat{m}_b = 6.8$ and $M_s = 7.7$. The teleseismic average P-wave moment rate spectrum from 17 short- and intermediate-period instruments is slightly lower than that of an average $M_w = 8.0$ subduction-zone event.

The reference acceleration spectrum is computed from the average teleseismic source spectra. The observed acceleration spectrum has approximately the same amplitude as the reference spectrum. We constrained the fault plane as determined above to deconvolve the first 90 secs of the long-period body wave at 11 teleseismic stations to determine the source-time function and the spatial distribution of moment release. The source-time function consists of 4 moment-releasing episodes that have a total moment release of 9.4×10^{27} dyne-cm. The fault ruptured bilaterally with the largest moment-releasing subevent occurring between 30–45 sec. This subevent nucleates approximately 75–90 km west of the determined epicenter. Regions of large moment release correspond to regions of low or no aftershock seismicity. This region corresponds to the epicentral area of the 1957 Great Aleutian earthquake, one of the largest earthquakes in recorded history.

2.1 Introduction

The May 7, 1986 Andreanof Islands earthquake (22h 47m 10.2s UTC, 51.412°N, 174.830°W, h=33 km, M_s = 7.7, NEIC) is the largest event that has occurred in this portion of the Aleutian arc since the 1957 Great Aleutian earthquake. The earthquake was felt on Atka approximately 65 km north of the epicenter and on Adak 130 km northwest, and caused damage on both islands but no fatalities (Figure 2.1).

The Aleutian arc is one of the most seismically active regions in the world, and has generated several of the largest earthquakes in recorded history. These large earthquakes are part of an earthquake sequence that ruptured most of the Alaska-Aleutian arc during the period 1938 to 1965. Areas that did not rupture during

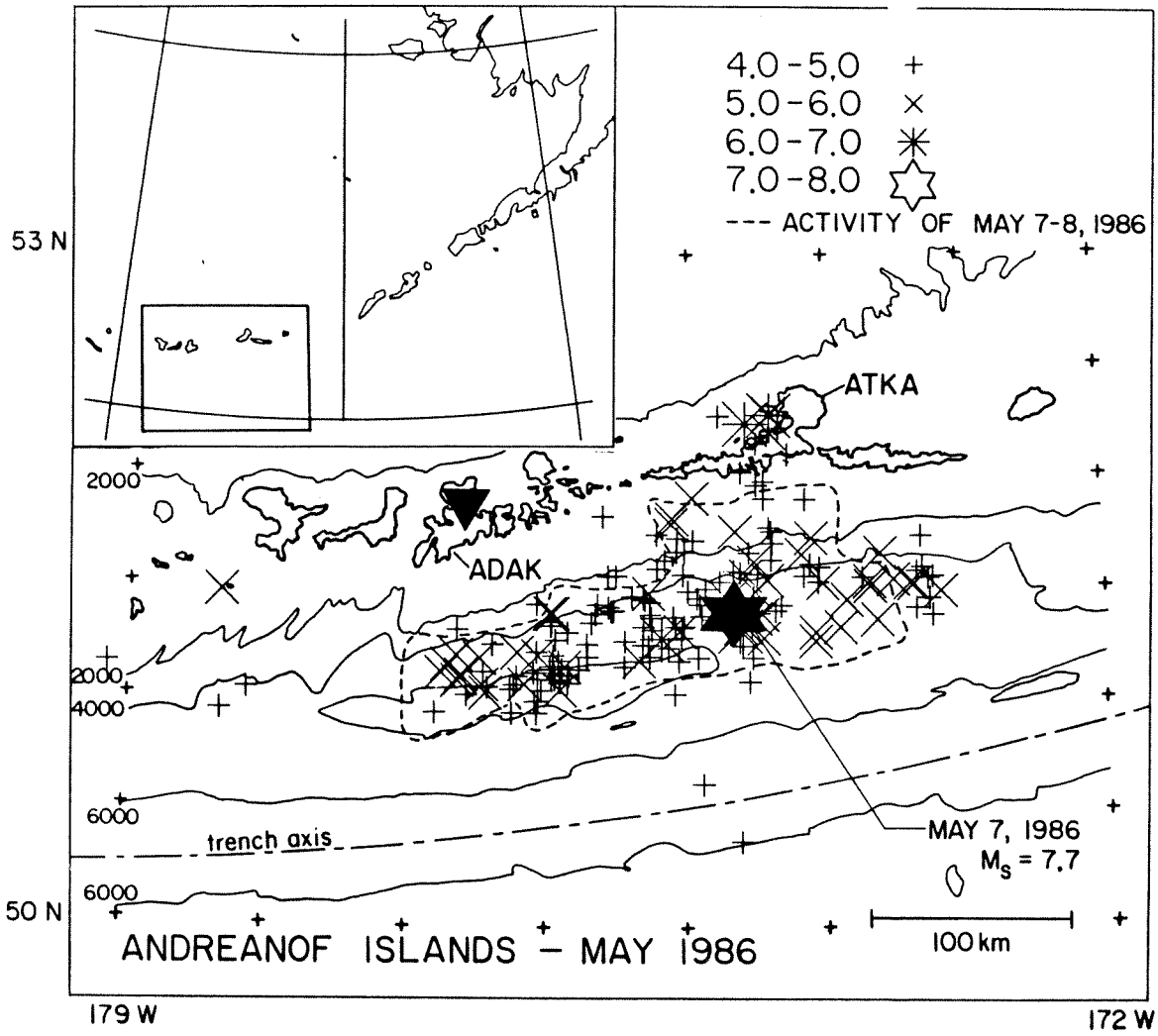

Figure 2.1: Map of a portion of the Aleutian Islands showing earthquake activity during May 1986 from the PDE catalog. The May 7, 1986 earthquake is plotted as a filled star. The aftershock area within the 24 hrs following the main event is outlined in dashed lines. A filled, inverted triangle marks the location of the strong motion instrument on Adak.

this period of increased activity have been identified as seismic gaps. These gaps, the Yakataga, Shumagin, Unalaska and Kommandorski, have not broken in at least 80 yrs. Recurrence times of great earthquakes in this region average about 80 yrs (Jacob, 1984). However, they are estimated to be as low as 50 yrs and may exceed 100 yrs (Sykes *et al.,* 1981).

The March 9, 1957 Great Aleutian earthquake, M_w = 9.1, located at 51.3°N, 175.8°W, is one of the largest earthquakes in recorded history and occurred very close to this more recent event. This earthquake ruptured a 1200 km segment of the arc. The aftershock sequence defines two segments of the rupture zone — one west of Amukta Pass (172°W) and one east (Mogi, 1968). Since the arc ruptured here just 29 years ago, seismic potential in this area has been rated very low (Sykes 1971; McCann *et al.,* 1979; Sykes *et al.,* 1981; Jacob, 1984).

The 1986 Andreanof Island earthquake occurred within the western aftershock zone of the 1957 Great Aleutian earthquake. Portions of the western aftershock zone have ruptured before in major events. Kisslinger (1985) examined the seismicity in a region between 175-178.8°W called the Adak Seismic Zone. This zone ruptured in a sequence of large earthquakes (M_s = 7.8) between 1901-1905 and in 1957. No great earthquakes occurred in this region until 1986. The 1986 earthquake is unique because of the unexpectedly short recurrence time and the partial overlap of its rupture zone with the 1957 earthquake. To better understand this earthquake and its relationship to the 1957 earthquake, we examine the source characteristics of the May 7, 1986 earthquake over a broad period range (1–256 sec).

2.2 Aftershock Area

The 1986 Andreanof Islands earthquake was preceded by several foreshocks, the largest, $M_s = 6.0$, occurring a little over two hours before the main event. Numerous aftershocks followed over the next several days (Figure 2.1), extending over a 220 km segment of the arc. The western zone of the aftershock area is bounded by Adak Canyon. The eastern zone coincides with the eastern edge of the western aftershock zone of the 1957 event, strengthening the argument for a structural discontinuity (or barrier) here as proposed by Mogi (1968). The aftershock zone grew northward toward Atka within the following weeks (Figure 2.1). Ensuing activity has been restricted primarily to within this aftershock zone.

Kisslinger (1985) forecasted an earthquake measuring $M_s = 7$ to occur in late 1985 in the immediate vicinity of Adak Island and to rupture soon after into Adak Canyon. The epicentral region of this predicted event is over 150 km from the epicenter of the 1986 earthquake. Although the immediate aftershock sequence extended into the Adak Seismic Zone, it did not break into the Adak Canyon sub-region.

2.3 Focal Mechanism

The focal mechanism for the main event was determined from 67 Worldwide Standardized Seismograph Network (WWSSN) and Global Digital Seismograph Network (GDSN) stations. The first-motion data fix one of the nodal planes reasonably well (Figure 2.2). Inversion of long-period surface waves (described below) determines the second nodal plane to be dip 18°, rake 116° and strike 257°. This thrust mechanism is consistent with the orientation of the plate boundary and plate motion in this

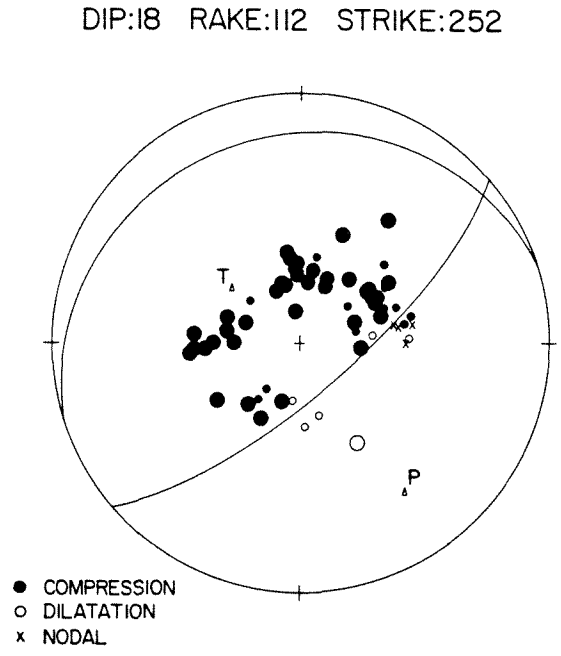

Figure 2.2: Focal mechanism for the May 7, 1986 earthquake. Sixty-seven stations are used to constrain the steeply dipping nodal plane. Large symbols are good quality and small symbols poor quality picks.

region (Minster and Jordan, 1978).

2.4 Seismic Moment and Rupture Area

Seismic moment, M_o, is determined from long-period surface waves from International Deployment of Accelerometers Network and GDSN stations, following Kanamori and Given (1981). Amplitude and phase spectral data at 256 sec are inverted using excitation functions for a source depth of 16 km. Since the source depth is less than 30 km, two elements of the seismic moment tensor cannot be resolved. We therefore use a double-couple source constraining one plane from the first-motion data. The source-time delay is varied from 10 to 80 sec. Using 48 Rayleigh waves, R2-R4, the best-fitting solution occurs at a source-time delay of 60 sec, which yields

$M_o = 1.3 \times 10^{28}$ dyne-cm, $M_w = 8.0$. Adding 12 Love waves, G2-G4, gives approximately the same seismic moment. Since this is a very large event, directivity of the propagating dislocation causes the source-time delay to be azimuthally dependent. Assuming a simple rupture propagating a distance of 150 km to the west at 3 km/sec and considering azimuth to the receiver, delay times are computed at each station. Using these times in the inversion does not alter the solution significantly. For simplicity here, we use a constant source-time delay of 60 sec.

The aftershock data within the first 24 hr of the mainshock suggest an immediate rupture zone of approximately 220 km in length and 65 km in width. Assuming that rigidity is $\mu = 5 \times 10^{11}$ dyne-cm^{-2}, the estimated slip during this event is 180 cm, corresponding to a slip rate of 6.3 cm/yr since 1957. This estimate is somewhat lower than the average plate motion calculated by Minster and Jordan (1978). The Minster and Jordan slip rate, 8.1 cm/yr, indicates a deficiency of slip of approximately 53 cm. This deficiency can be substantially reduced if aseismic slip is occurring (1.8 cm/yr) or if the rigidity of the fault plane surface is closer to crustal values.

2.5 Magnitude and Source Spectra

Amplitudes of body and surface waves from short-period, vertical component WWSSN and GDSN instruments yield a magnitude of $\hat{m}_b = 6.8$ (40 station average) and an $M_s = 7.7$ (33 station average) with a standard deviation of $\sigma = 0.34$ and $\sigma = 0.32$, respectively (Houston and Kanamori, 1986).

The average moment-rate spectrum computed from short- and intermediate-period vertical component GDSN instruments using the method of Houston and

Kanamori (1986) is slightly lower than the average $M_w = 8.0$ subduction zone event (Figure 2.3).

The strong motion spectrum is computed from a single station on Adak (see Figure 2.1). The source spectrum above is used to calculate the reference spectrum following Houston and Kanamori (1990), assuming that the strong motion consists of far-field S waves from a point source recorded on the surface of a uniform half-space. The reference spectrum thus calculated is not a realistic estimate of the acceleration spectrum at a specific site but is a standard against which the observed spectrum is compared. Comparison between the two shows that the reference spectrum has an amplitude comparable to the observed acceleration spectrum at a distance of 100 km measured between the recording site and the approximate center of the fault plane (Figure 2.4). Previous studies for other large subduction zone earthquakes (Hwang and Kanamori, 1989; Houston and Kanamori, 1990) showed that at distances of 50 km, the observed spectral amplitudes are two times larger than the reference amplitudes. This ratio increases to 10 at distances of 200 to 300 km. For the Adak site, using a larger distance such as the distance to the hypocenter ($\approx$135 km) would lower the amplitude of the reference spectrum with respect to the observed spectrum, but the difference is negligible. Larger source distances that are not physically reasonable are required to match previous observations. While the comparison for the Adak site does not agree with previous conclusions, it does fall within the error range of observations for the 1985 Valparaiso earthquake (Houston and Kanamori, 1990).

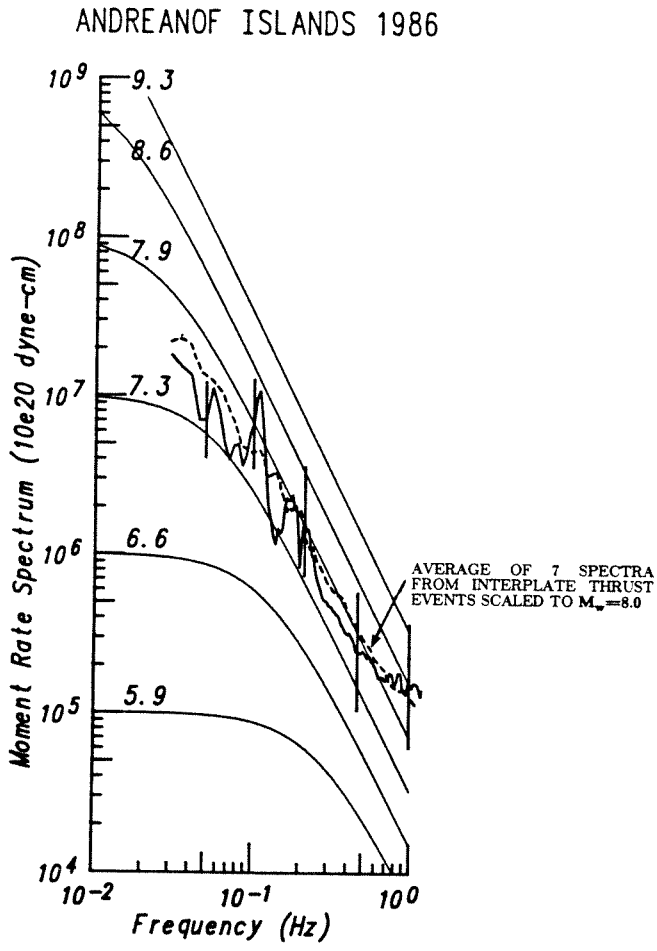

Figure 2.3: Average moment rate spectrum for the May 7, 1986 earthquake. Theoretical spectra for an ω^{-2} model are shown by thin lines. The dashed line shows the average spectrum from 7 events for an $M_w = 8.0$ subduction zone event.

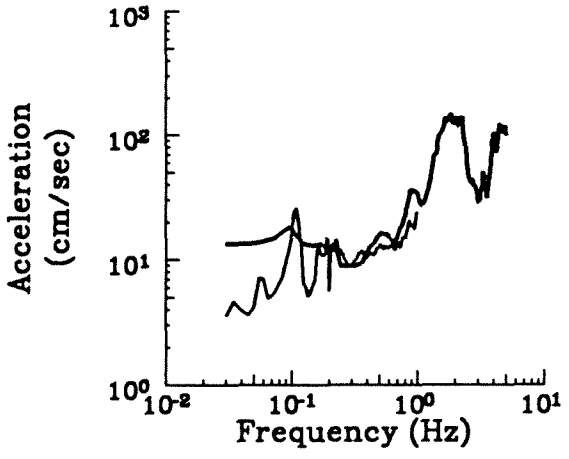

Figure 2.4: Comparison of the strong-motion spectrum (thick line) and the reference spectrum (thin line) for a distance of 100 km.

2.6 Rupture Pattern

The source-time function is determined by simultaneous inversion of the first 90 sec of the body wave from 6 long-period WWSSN and 5 intermediate-period GDSN vertical component instruments, following Kikuchi and Fukao (1985). We use the focal mechanism as determined by the surface-wave inversion and extend the fault-plane surface discussed above from the aftershock data up to the trench axis. Figure 2.5 shows the best fitting synthetics compared to the data. The source-time function of these synthetics is shown in Figure 2.6. For all models considered, the general features of the source-time function are stable. The first moment-releasing episode is of lower amplitude and duration than the second and largest episode. Moment release then falls off, with several smaller episodes occurring in the remaining 45 sec.

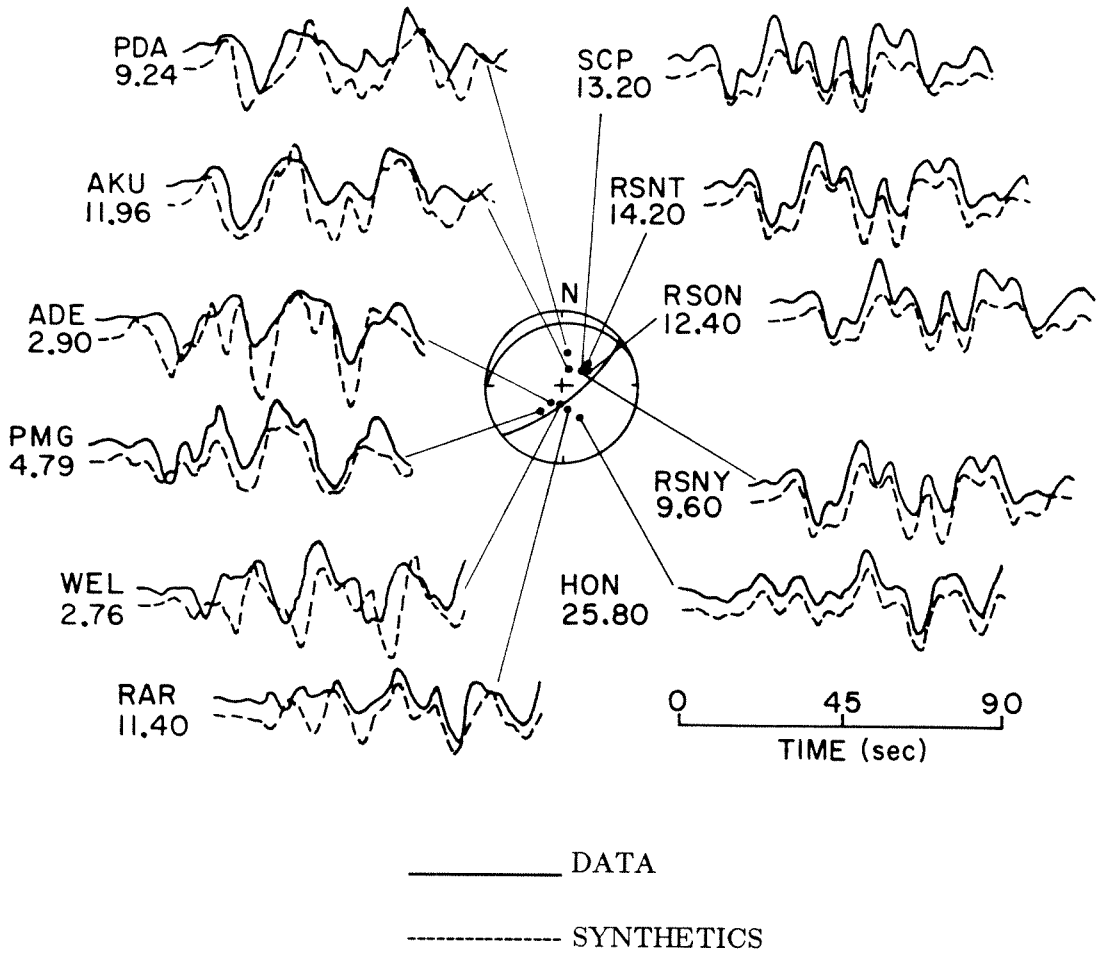

Figure 2.5: Comparison of actual (solid lines) and synthetic (dashed lines) seismograms from body-wave inversion. Peak amplitudes for the data in cm are given below each station for a long-period WWSSN instrument with a magnification of 1500. The focal mechanism and stations used in the inversion are shown.

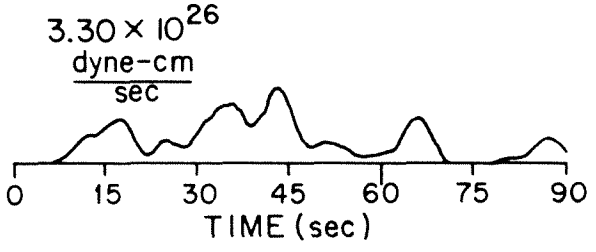

Figure 2.6: Source time function from the simultaneous body wave deconvolution. Peak moment release rate is 3.30×10^{26} dyne-cm/sec.

Total moment release for this model is $M_o = 9.4 \times 10^{27}$ dyne-cm.

With our distribution of stations, the rupture pattern (Figure 2.7) is resolved better along strike than perpendicular to strike. Moment release during the first 15 sec propagates along dip with the largest subevent located down dip towards the north. The rupture area expands bilaterally and moment release culminates in the second subevent between 30–45 sec. During this largest subevent, the point sources cluster about 75–90 km west of the epicenter. Remaining activity is diffuse.

This result is in good agreement with the results of Houston and Engdahl (1989), who used the same method but a broader band data set to study this event (Figure 2.8). In their study, they noted that mainshock moment release tended to occur in regions of low or no aftershock activity. Their largest and best-located subevent at 12 sec correlates in time and position with one of the largest subevents in our model. This subevent occurs at the corner of a rectangular, quiescent zone along the fault plane. Houston and Engdahl (1989) also noted that moment concentrated up

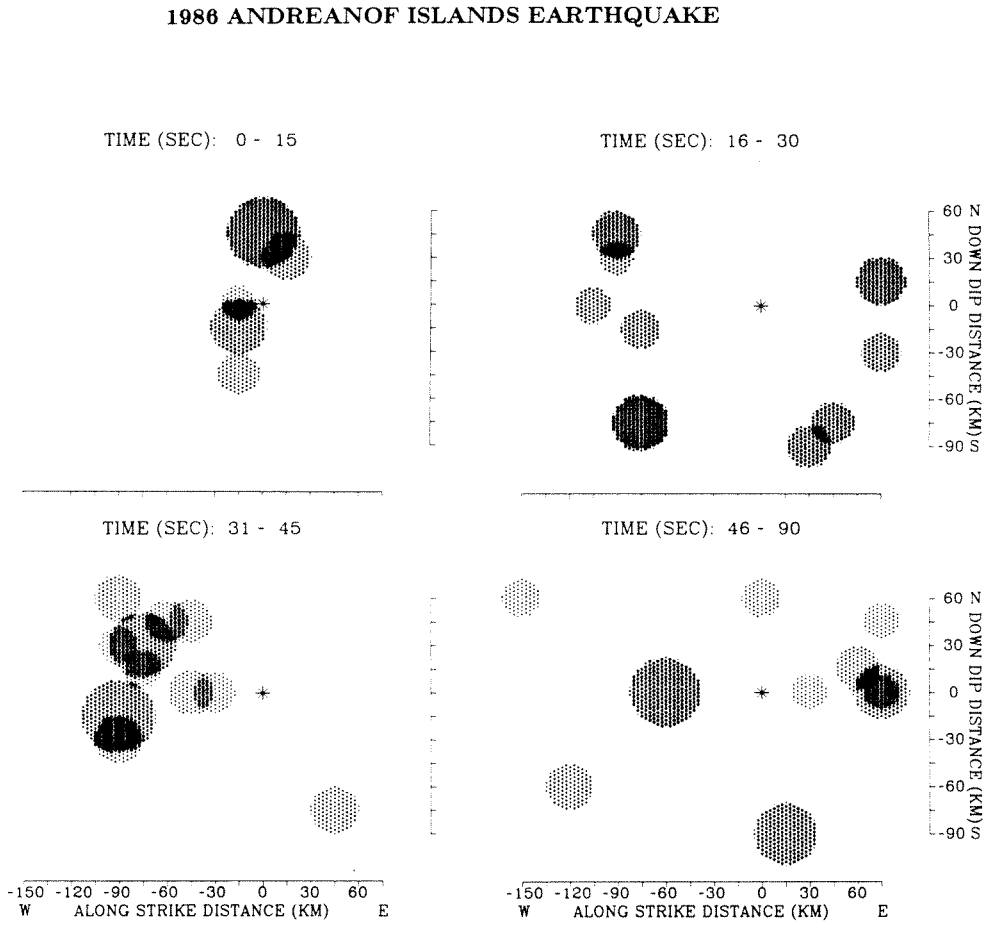

Figure 2.7: Fifteen-second time slices of the spatial distribution of moment release projected onto the fault surface. The radius of each circle is proportional to the seismic moment of the point source it represents. Shading is proportional to the amount of moment release in a given area and is normalized to the maximum value in each time slice. The asterisk marks the hypocenter.

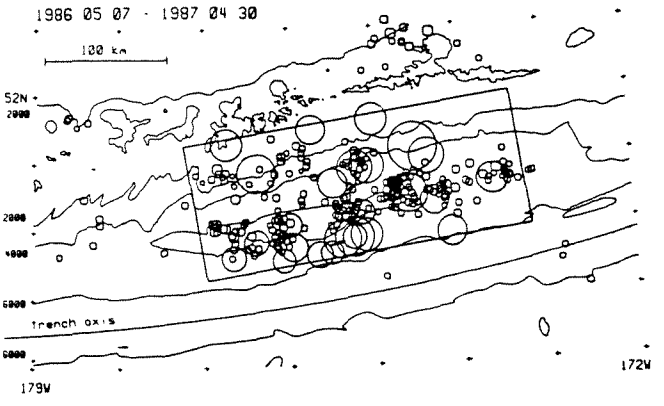

Figure 2.8: Shallow seismicity relocated by Engdahl *et al.* (1989) compared to moment release model of Houston and Engdahl (1989). Seismicity is plotted as open octagons. The mainshock is indicated by a large, filled octagon. Distribution of moment release is shown by circles that represent moment-releasing subevents. (After Houston and Engdahl, 1989.)

dip and southwest of the hypocenter along the edge of their modeled fault plane. For the same time period, our model suggests moment release clusters more towards the center of the fault plane at approximately the same distance. For both models, moment release again occurs in regions of low aftershock seismicity. These two regions can be thought of as asperities along the fault surface. The first region is associated with the initial failure of the fault surface, which perhaps triggered the failure of the second. Within the resolution of the data, the second and largest subevent corresponds to the epicenter of the 1957 earthquake.

2.7 Conclusion

The 1986 Andreanof Islands earthquake is the largest event to occur within the Islands since 1957. This great event, $M_o = 1.3 \times 10^{28}$ dyne-cm, M_w=8.0, ruptured only 20% of the arc that failed in 1957. The end points of the aftershock region are well defined by Adak Canyon to the west and the eastern terminus of the western aftershock zone of 1957 to the east. Body-wave modeling shows that this region is composed of 2 strong asperities, one associated with the 1986 epicenter and the other with the 1957 epicenter. The effect of the rupturing of these two asperities within such a small portion of the 1957 aftershock zone is unclear. Li and Kisslinger (1984/85) find that rupture in adjacent fault segments can accelerate the loading rate and cause a coseismic stress jump in neighboring segments. This possibly triggers rupture of neighboring segments if they are at a high stress state. Hence, failure of adjacent segments that is due to accelerated loading from the 1986 earthquake depends on several poorly constrained parameters: current stress state, loading rates, and failure strengths. Further modeling of both stress transfer along plate boundaries and possible accelerated plate motions following great earthquakes (Anderson, 1985; Lyzenga *et al.*, 1986) must be considered to further understand plate interaction and seismic hazard in this region.

Chapter 3

Teleseismic and Strong Motion Source Spectra from Two Earthquakes in Eastern Taiwan

Abstract

The May 20 and November 14, 1986 Hualien earthquakes occurred in a seismically active region of Taiwan. Locally determined focal mechanisms and aftershock patterns from the Taiwan Telemetered Seismographic Network indicate that both earthquakes occurred on steeply dipping reverse faults that trend NNE. This agrees with teleseismic, first-motion data for the May event, but not for the November event. This discrepancy is due to a moderate foreshock before the November event. Surface-wave analysis gives a solution for the November event of dip 57°, rake 100°, and strike 43°, which is similar to the locally reported focal mechanism. The seismic moment of the November event is $M_o = 1.7 \times 10^{27}$ dyne-cm, and the magnitudes

determined from WWSSN data are $\hat{m}_b = 6.4$, $M_s = 7.3$. Teleseismic source spectra show that the two events also have similar spectral signatures above 0.15 Hz. Reference acceleration spectra are computed from the average teleseismic source spectra and are compared to the averaged acceleration spectra computed from strong-motion stations for both events. Correlations between the spectral amplitudes of the strong-motion spectra, obtained from the main portion of the SMART 1 array, and the teleseismically estimated reference spectra are poor above 0.2 Hz. Data from the hard rock site situated outside the basin indicates that amplification of the ground motion between 0.15–1.7 Hz is due to the alluvial valley where the SMART 1 array is located. The amplitudes of the observed spectra are 5 times the reference spectra at the hard rock site. This is consistent with similar observations from the 1985 Michoacan and 1983 Akita-Oki earthquakes. The analysis of these and more teleseismic and strong-motion records will lead to a better understanding of the relationship between their spectra.

3.1 Introduction

The determination of strong ground motion for large earthquakes is a fundamental problem in earthquake engineering. To design structures that withstand large earthquakes, an engineer must consider the spectral content as well as the duration of an expected event. Only until recently have nearfield, strong-motion data become available for large earthquakes and efforts have begun to understand the regional variations of the source spectra.

Three factors determine the strong ground-motion spectra: the source, path,

and site effect. Since the source spectra at periods between 1 to 20 sec can be reliably determined from Global Digital Seismic Network (GDSN) data, path and site effects in the epicentral region can be evaluated by comparing teleseismic and strong-motion data. To do this, it is necessary to study those events for which both strong-motion and teleseismic recordings are available. One approach to estimating path and site effects is the use of numerical techniques such as the finite element or difference methods to model the local structure. However, the local structure is not always known well enough for such modeling. In addition, these techniques do not accommodate large source-receiver distances very well in the frequency range of interest.

In this paper we take an alternative, empirical approach. We compare the observed strong-motion spectra with the teleseismically determined source spectra, assuming that the strong-motion data are recorded on the surface of a uniform half-space. In most cases, this is a simplification of the real situation. However, any discrepancies between the observed and estimated spectra can be interpreted as being due to the combined path and site effect. Differences will vary as a function of distance and may also depend on source region and earthquake magnitude. The accumulation of data for a sufficiently large number of events to establish general relationships for different sites will enable the estimation of strong ground-motion spectra for different earthquakes. Houston and Kanamori (1987) used this approach to study the 1985 Michoacan, Mexico, and 1983 Akita-Oki, Japan earthquakes. The two recent earthquakes in eastern Taiwan were well recorded at both teleseismic stations and a local strong motion array and provide an excellent data set for this

study.

The island of Taiwan is located in a young, active orogenic belt on the boundary between the Eurasian and Philippine Sea plates. Collision along this boundary has formed belts of deformed NNE trending Tertiary geosynclinal sediments and metamorphics paralleling the axis of the island. Near Hualien, the boundary between the two plates changes from the south from a northeast-trending, oblique-slip, transform fault, the Longitudinal Valley fault (LVF), to an east-west trending thrust fault with the Philippine Sea plate subducting northward under the Eurasian plate along the Ryuku trench (Figure 3.1). Two major earthquakes in the Hualien region in 1951 were accompanied by reverse, oblique slip on the LVF. Both earthquakes studied here, the May 20, 1986 (05h 25m 46.9s UTC, 24.125°N, 121.619°E, h=19 km, M_s=6.4, NEIC) and the November 14, 1986 (21h 20m 10.5s UTC, 23.961°N, 121.836°E, h=34 km, M_s=7.8, NEIC) events, occurred along the very active eastern coast of Taiwan near the city of Hualien. These events were recorded both worldwide and by the SMART 1 accelerograph network on the Lanyang Plain near Lotung, Taiwan. The availability of high-quality, digital-data sets, the similarity of their focal mechanisms, and their close proximity to each other provide a good opportunity to study and compare the strong motion and teleseismic source spectra for events in this region.

3.2 The May 20, 1986 Hualien Earthquake

Seismicity and source parameters of the May 1986 event (Event 1) have been studied using data from the local array, the Taiwan Telemetered Seismographic Network

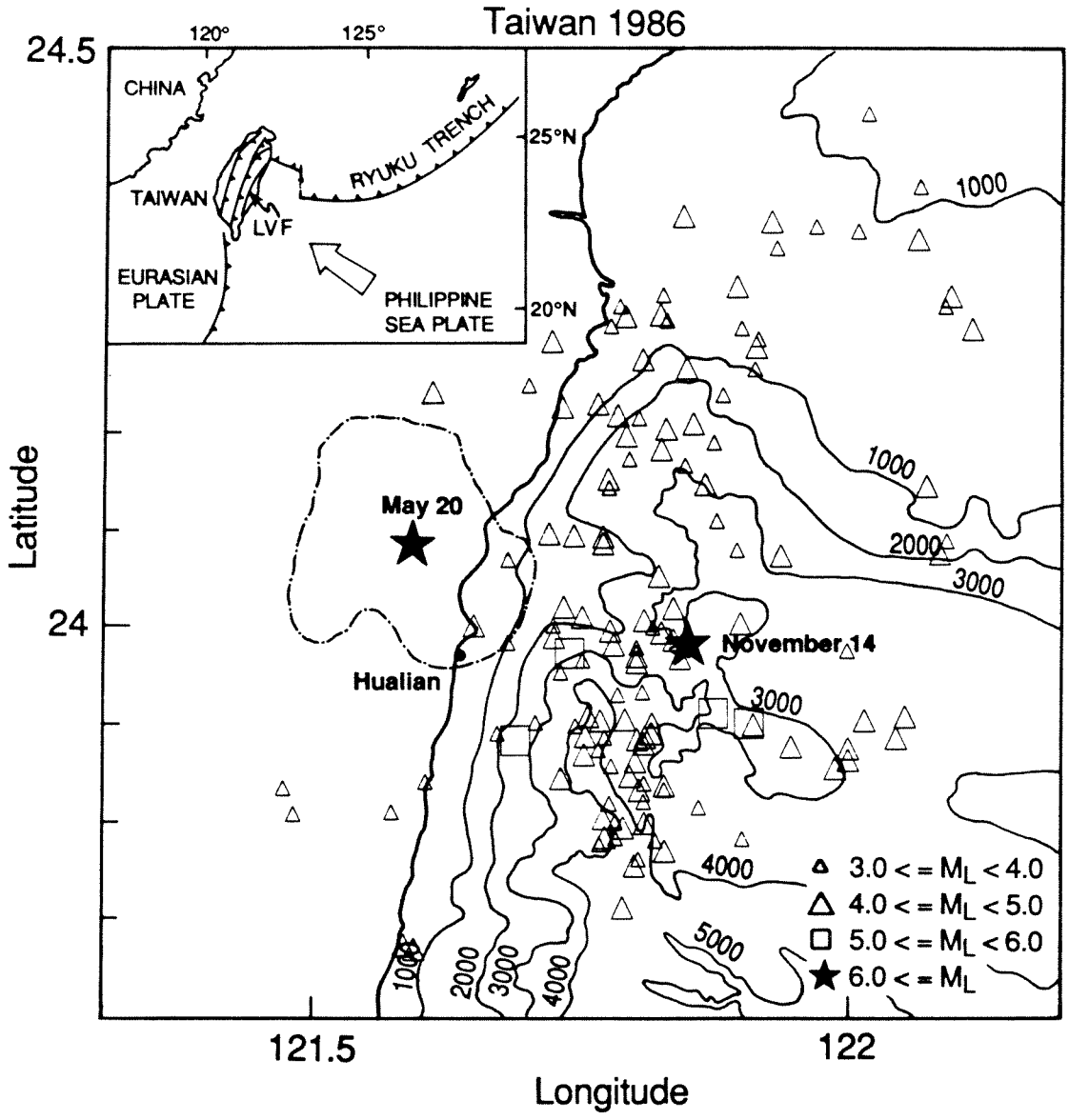

Figure 3.1: Inset shows the regional tectonics in the Taiwan region (after Ho, 1986). Symbols used are noted in the figure. LVF is the Longitudinal Valley fault. Outlined with dot-dashed lines is the aftershock region for the May 20, 1986 earthquake. Also shown is the November 14, 1986 earthquake along with the aftershocks from November 14–30, 1986 preliminarily located by TTSN.

(TTSN), as well as temporary seismic stations deployed soon after the main shock (Chen and Wang, 1986; Liaw *et al.*, 1986; Yeh *et al.*, 1988) and are reviewed briefly here. The TTSN relocated the hypocenter to 24.082°N, 121.592°E, h=15.8 km, and M_L = 6.5 ($M_o = 2.6 \times 10^{25}$ dyne-cm, NEIC). First motions from local data constrained the focal mechanism to dip 60°, rake 90°, and strike 35° (Chen and Wang, 1986). This is in good agreement with the teleseismic first motions we determined from GDSN and Worldwide Standardized Seismograph Network (WWSSN) data (Figure 3.2).

Aftershock activity associated with the mainshock occurred within a small area on two parallel, eastward, steeply dipping thrust faults. Activity migrated from the eastern to the western fault zone. Both structures are consistent with the regional tectonic setting. Aftershocks immediately following the main shock, which were relocated by Liaw *et al.* (1986) using high-quality local data, located to the northwest of the main shock and above the hypocenter located at 16 km depth. This spatial relation between the main shock and the aftershocks suggests that the rupture initiated at 16 km depth and propagated unilaterally upward to the northwest.

3.3 The November 14, 1986 Hualien Earthquake

Seismicity and source parameters of the November 1986 event (Event 2) are studied here using WWSSN, GDSN, Preliminary Determination of Epicenter (PDE) and TTSN data. The locally determined hypocenters of the mainshock (23.992°N, 121.833°E, h=13.9 km, M_L = 6.8; Yeh *et al.*, 1988) and aftershocks formed a NNE trending band of seismicity just offshore Hualien. The aftershocks were concentrated

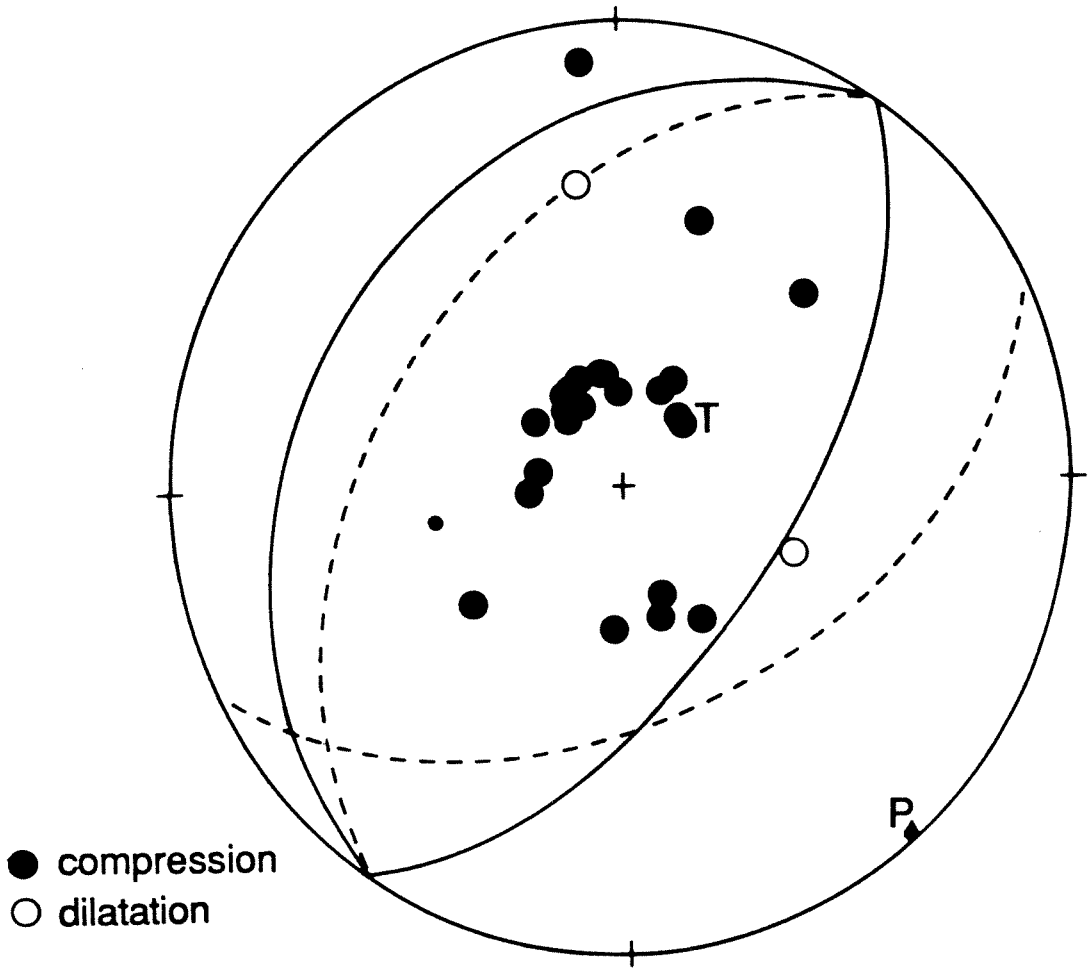

Figure 3.2: Focal mechanisms shown here and in subsequent plots are lower hemisphere projections. The solid lines show the locally determined focal mechanism for the May 20, 1986 Hualien earthquake (Chen and Wang, 1986). The dashed line shows the Harvard centroid moment tensor (CMT) solution (NEIC). Large symbols are good quality and small symbols poor quality picks.

in the upper 15 km of the crust but extended down to a depth of 37 km. Activity appeared to be confined within the non-subducted portion of the Philippine Sea plate, which is 50 km thick in this region (Tsai *et al.*, 1977). The aftershock region for this event adjoins that from Event 1 lying immediately to the west (Figure 3.1).

3.3.1 Source Parameters

Analysis of teleseismic first motions conflicts with the locally determined solution of strike 38° and dip 58° (Yeh *et al.*, 1988; Figure 3.3). This is due to a moderate foreshock (m_b = 5.4) occurring 5 sec before the main event. This foreshock can be identified on most WWSSN records. However, overall data quality for the body waves is poor. A more robust determination of the focal mechanism is made by inverting the Rayleigh and Love waves recorded by the GDSN stations over a period range of 180 to 285 sec, using a centroid moment tensor code (CMT) written by Kawakatsu (1989), which is similar to that developed by Dziewonski *et al.* (1981). Three component data from 7 stations (ANMO, BCAO, HON, KONO, NWAO, SNZO, WMQ) are used to invert Rayleigh and Love wave phases R1-R3 and L1-L3, respectively. The preferred fault parameters for the best-fit double couple in the CMT inversion are strike 43°, dip 57°, rake 100° (strike 33°, dip 57°, rake 92°, HRV) and a moment of $M_o = 1.72 \times 10^{27}$ dyne-cm. This mechanism is consistent with the structural trends in this region. The amplitudes of body and surface waves from short-period vertical component WWSSN instruments yield magnitudes of $\hat{m}_b$=6.4 (19 stations, σ=0.29) ($\hat{m}_b$ is defined after Houston and Kanamori, 1986), and M_s=7.3 (11 stations, σ=0.40). Note that this estimate of M_s is substantially smaller than the reported NEIC value.

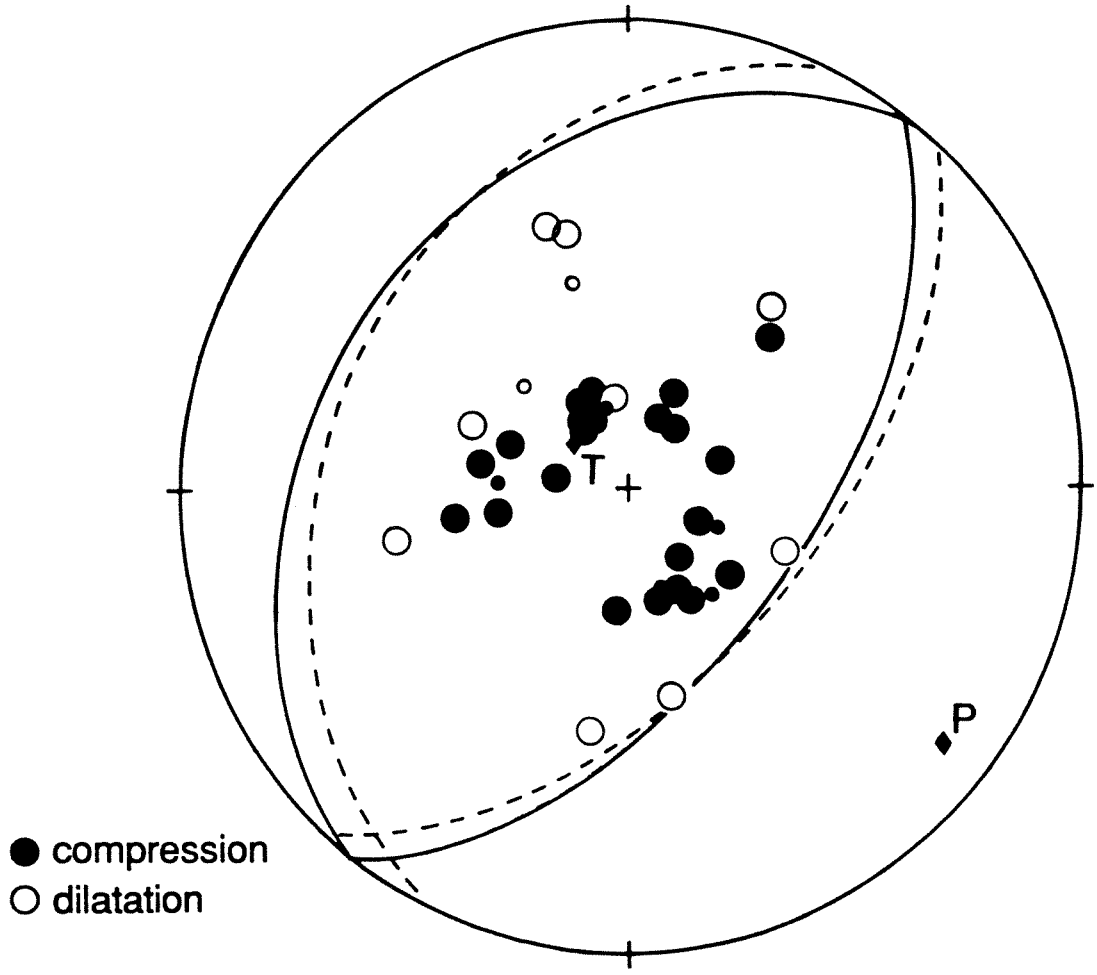

Figure 3.3: The solid line shows the locally determined focal mechanism for the November 14, 1986 Hualien earthquake (Yeh *et al.*, 1988). The dashed line shows our CMT solution. Symbols are the same as in Figure 3.2.

The source-time function and rupture pattern are determined by simultaneous inversion of the body waves following Kikuchi and Fukao (1985). We invert the first 60 sec of the body wave from four, long-period, vertical-component WWSSN stations and four vertical-component GDSN stations combining short- and long-period data to yield a WWSSN-type instrument response. The fault plane is determined by the extent of the aftershock zone within the first 24 hours of the mainshock. The focal mechanism is constrained by the surface-wave data. Distance and time are relative to the hypocenter and origin time, respectively, determined from local data.

Total moment release for our model is 1.9×10^{27} dyne-cm. Figure 3.4 shows the resulting synthetics (dashline), data (solid line) and source time function. Moment release between 0–5 sec is associated with the foreshock. It reaches its peak between 5–14 sec, followed by a smaller moment-releasing episode of long duration between 20–32 sec. Most of the moment release occurs close to the epicenter (Figure 3.5). While the long-period data cannot discriminate between individual point sources, modeling, using different parameterizations for the point sources, indicates that the source-time function and position of major moment-releasing subevents are robust.

3.4 Teleseismic and Strong Motion Source Spectra

Source spectra for the two events are calculated between the periods of 1 to 20 sec from GDSN records using, the method of Houston and Kanamori (1986). In their method, the spectrum is corrected for instrument response, geometrical spreading, radiation pattern, and the free-surface receiver effect. The density and P-wave velocity within the crust are taken here to be 2.8 gm/cm^3 and 6.5 km/sec, respectively.

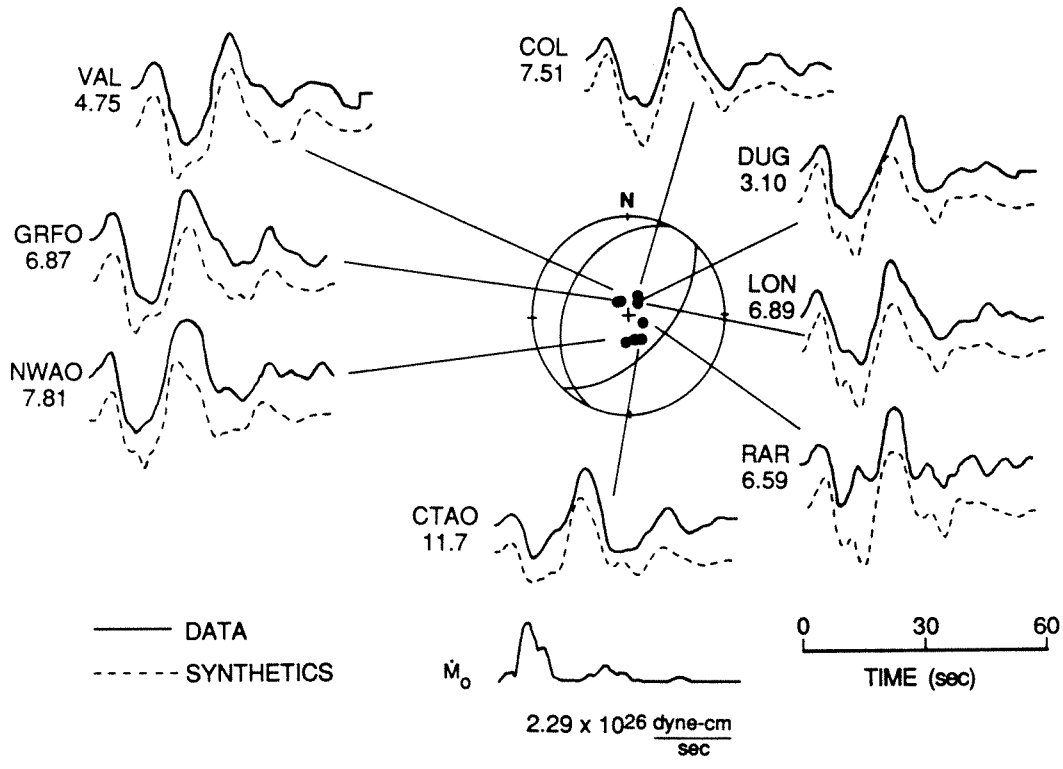

Figure 3.4: Comparison of actual (solid line) and synthetic (dashed line) seismograms from the body-wave inversion. Peak amplitudes for the data in cm are given below each station for a long-period WWSSN instrument with a magnification of 1500. The synthetics at each station are plotted to the same scale as the data. The focal mechanism and stations used in the inversion and the resulting source-time function are shown. The peak moment release rate for the source-time function is $2.29 \times 10^{26} \frac{\text{dyne-cm}}{\text{sec}}$.

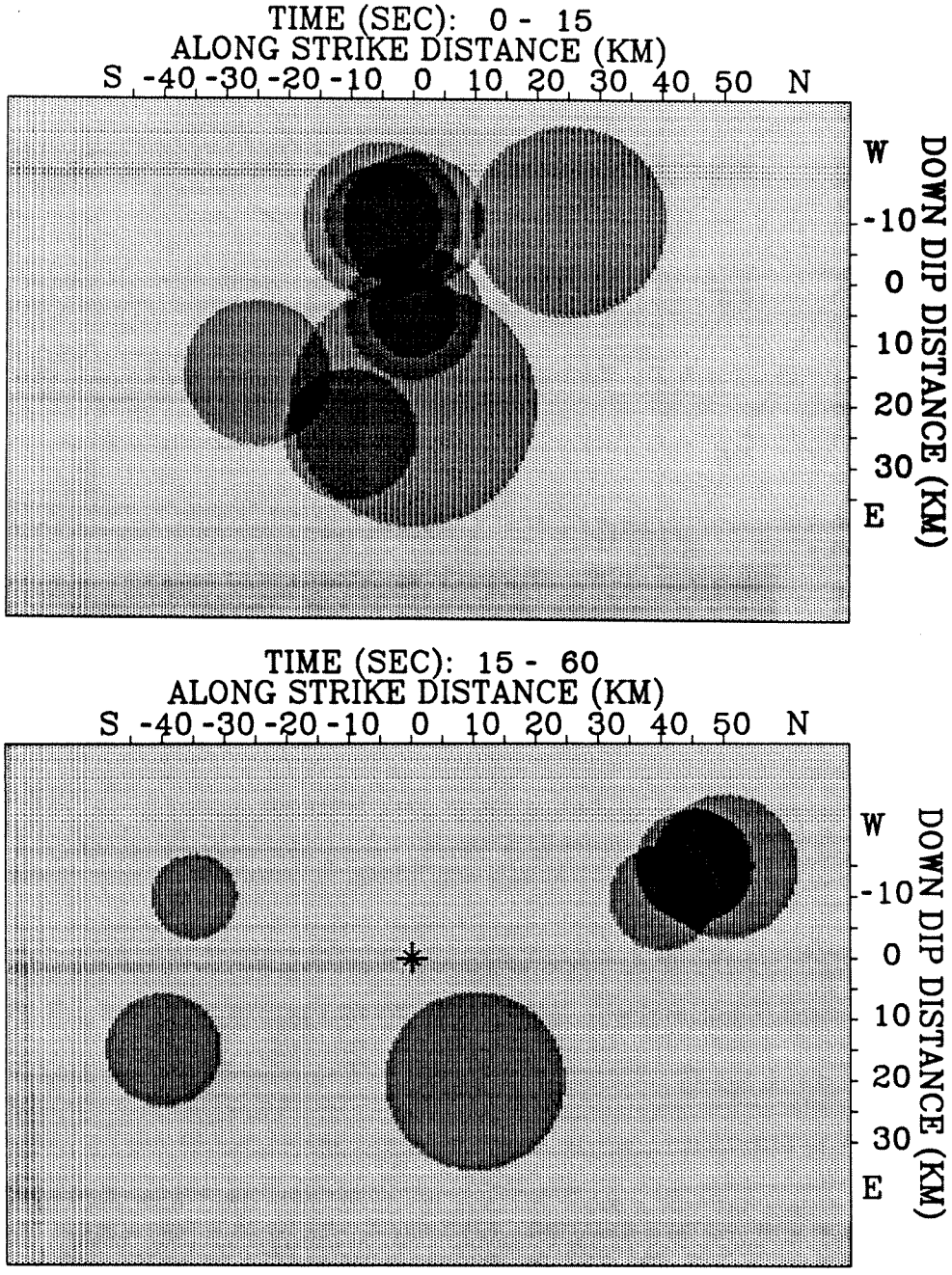

Figure 3.5: Time slices of the spatial distribution of moment release projected onto the fault surface. The radius of each circle is proportional to the seismic moment of the point source it represents. The asterisk marks the hypocenter.

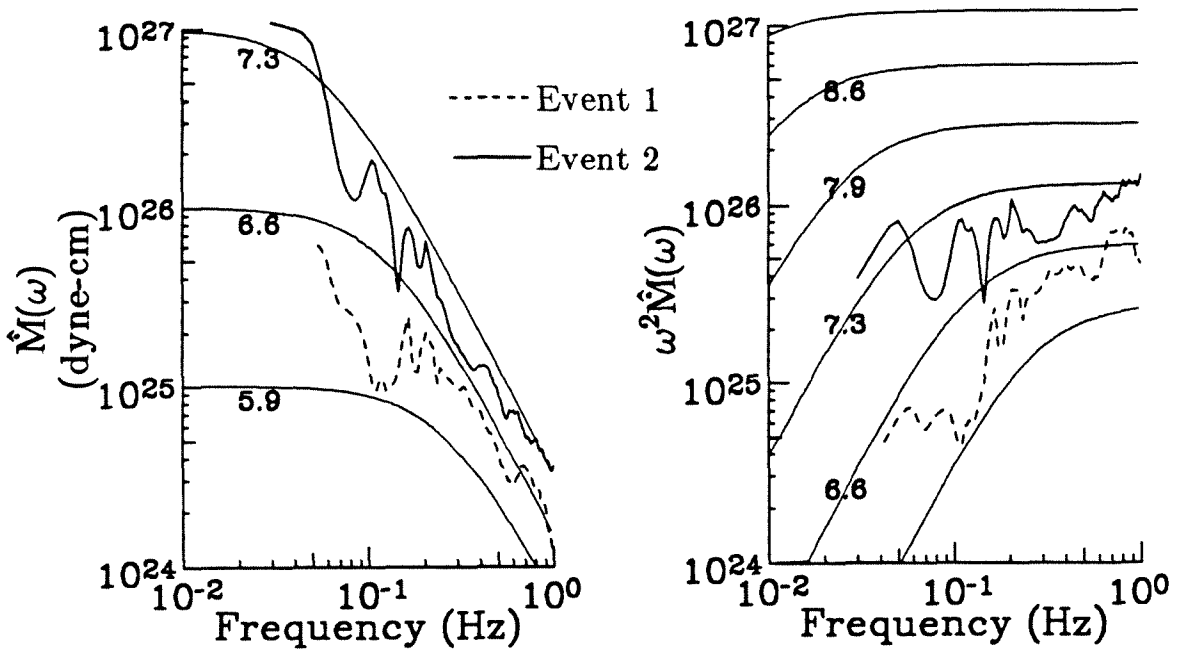

Figure 3.6: a. Average moment rate spectra and b. average acceleration spectra from teleseismic GDSN stations for Event 1 (dashed line) and Event 2 (solid line). Theoretical spectra for an ω^{-2} model are shown by thin lines.

equal to 0.7 sec. The average moment rate and acceleration spectra are computed from 6 short-period teleseismic P-wave seismograms for Event 1, and 7 for Event 2. The overall shape of the teleseismic spectrum of the two events is consistent with an ω^{-2} model, and both displacement spectra have a similar shape above 0.15 Hz (Figure 3.6). However, between 0.05–0.15 Hz, the displacement spectrum for the first event drops considerably in amplitude. This difference is more clearly seen in the acceleration spectra of the two events (Figure 3.6b). Differences in the spectra may reflect differences in the rupture pattern between the two events. Unfortunately,

may reflect differences in the rupture pattern between the two events. Unfortunately, we could not determine the rupture pattern of Event 1 because of its relatively small size.

The strong-motion spectra are computed from the data obtained from the SMART 1 array. The main portion of the SMART 1 array is comprised of 37 stations in 3 concentric rings with radii of 0.2, 1.0 and 2.0 km. Two external stations are located at distances of 2.8 and 4.8 km south of the central station of the main array. The array is situated 70 and 77 km north from the two events in an alluvial valley of recent age. The water table is either near or at the ground surface (Abrahamson *et al.,* 1987). Figure 3.7 shows the average strong-motion spectra and Figure 3.8, the spectra for the hard-rock station E02 for both events.

As shown above, the two events have similar focal mechanisms and source locations but very different magnitudes. The difference of 0.3 in M_L between the two events is consistent with the difference of about a factor of 2 in the moment-rate spectrum at 1 Hz (Figure 3.6). However, the amplitude of the strong-motion spectrum at 1 Hz for Event 1 is about the same as that for Event 2 (Figure 3.7). In addition, the overall shape of the acceleration spectrum determined from the strong motion records is very different between the two events. This discrepancy is due to the difference in magnitude, which causes a spectral shift and is probably also due to the difference in the epicentral locations of the two events with respect to the Lanyang Plain. This suggests the importance of the source-site geometry for amplification of nearfield, strong ground motions. Although the effect of different epicentral locations is small for teleseismic stations, it can be significant for local

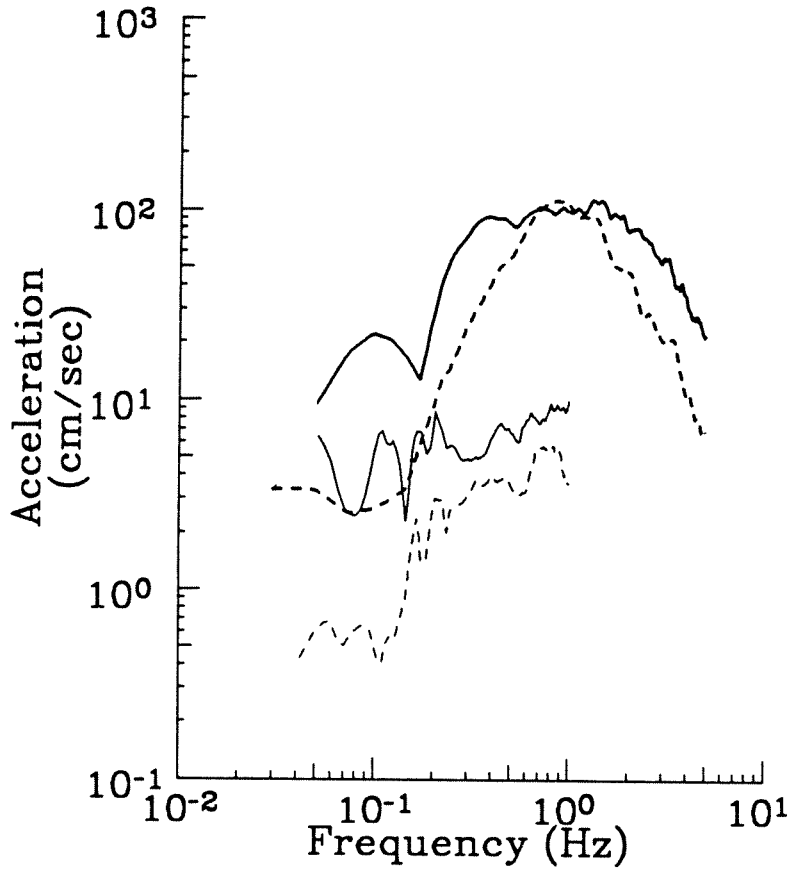

Figure 3.7: Averaged strong-motion spectra from the SMART 1 array and teleseismically estimated reference spectra for both events. Strong-motion spectra are shown in thick lines and teleseismic spectra with thin lines. Event 1 is given with dashed lines and Event 2, solid lines.

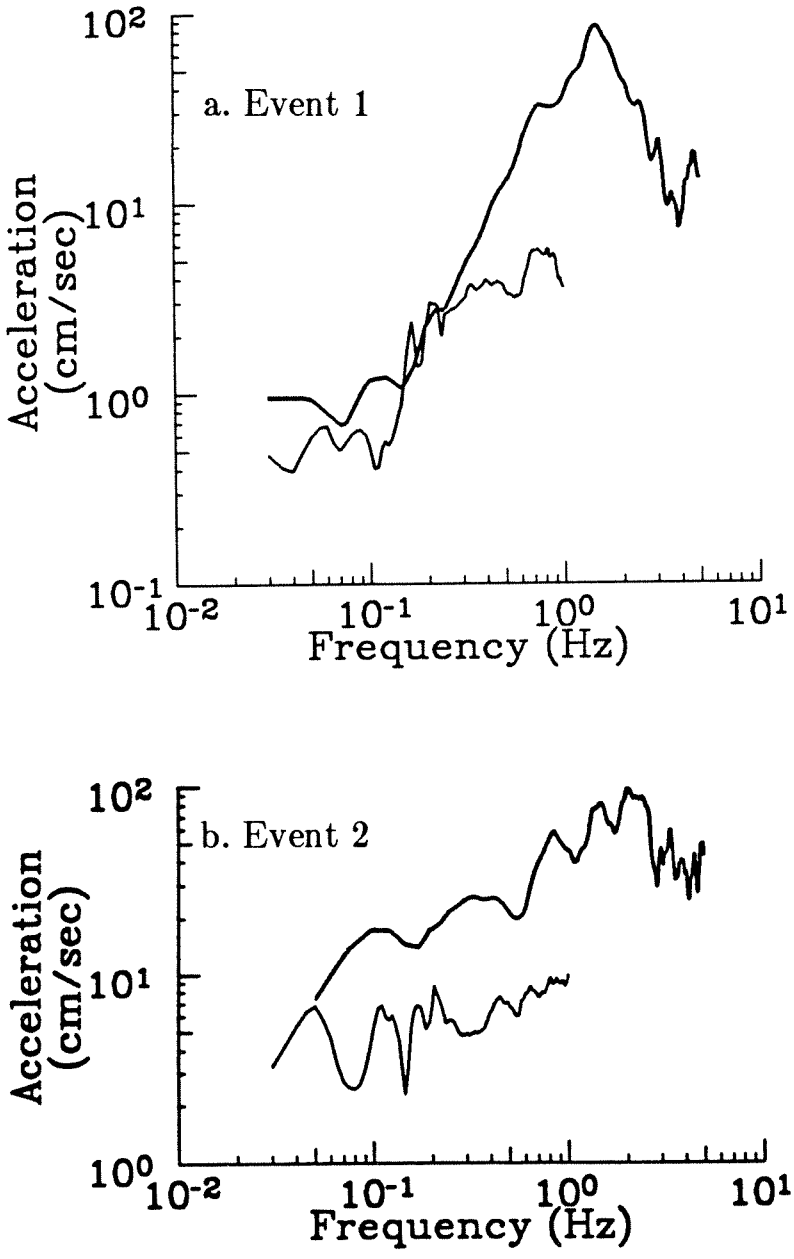

Figure 3.8: Comparison of strong-motion and reference spectra between the hard-rock site E02 and a. Event 1 and b. Event 2. Strong-motion spectra are shown in thick lines and reference spectra in thin lines.

stations.

The observed acceleration spectra cannot be directly compared with the source spectra determined from teleseismic data. Since our purpose is to estimate path and site effects, we want to compare the observed spectra with spectra that would have been observed from a simple structural model that has no significant path and site effects. Hence, following Houston and Kanamori (1987), we assume that strong ground motions consist of far-field S waves from a point source recorded on the surface of a uniform half-space, and compute the acceleration spectrum from the point-source spectrum obtained from teleseismic data. The spectra are corrected for the free-surface effect for SH waves and the S-radiation pattern averaged over the entire focal sphere. A Q of 300 is assumed. In the half-space, the S-wave velocity is assumed to be $\beta = 3.8$ km/sec, and the density, $\rho = 2.8$ g/cm^3. The distance between the source and receiver is 70 km for Event 1 and 77 km for Event 2, respectively. The spectrum thus calculated is called the reference spectrum. The reference spectrum is not a direct estimate of the acceleration spectrum at a specific site, but is a standard against which the observed spectrum is compared. Any difference from the reference spectrum is attributed to path and site effects.

A finite source was not considered. For Event 1, the low magnitude of the event indicates that a point-source approximation is reasonable. For Event 2, the point-source approximation is applied since most of the moment release occurred within the first 15 sec (Figure 3.4) in a small region close to the nucleation point (Figure 3.5).

Comparison between the reference acceleration spectra estimated from teleseismic data and the strong-motion spectra (Figure 3.7) show that beginning approximately

at 0.2 Hz, the strong-motion spectra start to differ substantially from the reference spectra. The amplitude ratio of the strong-motion spectrum to the reference spectrum increases with increasing frequency. For Event 1, the strong-motion spectrum at 0.2 Hz is 3 times the amplitude of the reference spectrum. This ratio increases to 20 at 1 Hz. Similarly, for Event 2, the strong-motion spectrum is 4 times the amplitude of the reference spectrum at 0.2 Hz and increases to 10 at 1 Hz.

3.5 Site Effect

The spectral amplitudes of the strong-motion records in this study are 10–20 times larger than the reference spectra computed from teleseismic data. This discrepancy is larger than those found for other large subduction zone events. Examples from the 1985 Michoacan and 1983 Akita-Oki earthquakes at similar distances (Houston, 1986) do not exhibit such large discrepancies as those from the Hualien events. For these events, the observed strong-motion spectrum is about 2–5 times the amplitude of the reference spectrum.

Site amplification that is due to sediment-filled basins has been studied by many authors. Both analytical (Aki and Larner, 1970; Wong and Trifunac, 1974; Bard and Bouchon, 1980; Bravo *et al.,* 1988) and finite-difference and finite-element (Boore *et al.,* 1971; Joyner, 1975; Joyner and Chen, 1975; Vidale and Helmberger, 1988) techniques have been used to study the variations in amplitudes across sediment-filled basins. Amplitudes vary with the position of the receiver in relation to the geometry of the basin. Surface amplitudes also depend on the thickness of the sedimentary layers, impedance contrast between the layers, and the frequency and

angle of incidence of the incoming waves. Analytical modeling suggests that basin effects can cause amplitude variations of up to 7 times that of an equivalent flat layer model (Wong and Trifunac, 1974). Even larger amplitude ratios with respect to rock sites are expected and have been observed. King and Tucker (1984) observed that motions on the sediments of the Chusal Valley, USSR are up to 10 times larger than the nearby rock sites. Vidale and Helmberger (1988) also observed and modeled this effect for the 1971 San Fernando, California earthquake.

The above studies show that we can expect site amplifications produced by the alluvial valley where the SMART 1 array is situated. This effect is observed in this study and by Bolt and Chiou (1987). Bolt and Chiou observed for Event 2 that in the valley the peak accelerations were up to 1.7 times and peak velocities up to 3.2 times that of the rock site. In our study, this is illustrated by comparisons of the acceleration spectrum of the rock site to the alluvial site and to the reference spectrum. Comparison of the spectral amplitudes between the external hard-rock site E02 and the soft-rock sites show that the spectral amplitude at E02 is about 3 times lower than at the soft-rock sites for Event 2 at frequencies between 0.17–1.7 Hz. For Event 1, the spectral amplitude at E02 is 2 to 5 times lower between 0.15–1.5 Hz than at the soft-rock sites. The importance of site effects is further underscored when site E02 is compared to the reference spectra (Figure 3.8). The overall spectral shape of E02 more closely matches the reference spectrum for Event 2 than the spectrum from the main portion of the array. The observed spectrum from site E02 is 5 times the amplitude of the reference spectrum. For Event 1, the observed spectrum at E02 has 3 to 6 times the amplitude of the reference spectrum

above 0.3 Hz. Amplifications of 5 times the reference spectrum are consistent with observations by Houston (1986).

3.6 Conclusion

Two recent damaging earthquakes, the May 20, 1986 and the November 14, 1986 Hualien earthquakes provided a good opportunity to compare the nearfield acceleration spectra and the source spectra determined from teleseismic data. Both events occurred in the same region of eastern Taiwan — epicenters are approximately 25 km apart, and both occurred within a short time of each other. The focal mechanisms of both events indicate faulting along NNE trending, steeply eastward-dipping, reverse faults.

Acceleration spectra from the two events are compared with the reference spectrum computed from the teleseismic source spectrum. We define the reference spectrum to be the acceleration spectrum computed from the point-source spectrum, assuming a uniform half-space. The reference spectrum is a standard to be used in comparison to the observed acceleration spectra. Differences between the two spectra can be interpreted as being due to path and site effects. The results obtained from the SMART 1 data demonstrate clearly the importance of site effects. The average amplitude spectrum computed from the main portion of the array situated on alluvium is about 20 times larger than the amplitude of the reference spectrum. For both events, the ratio of the spectral amplitude observed at a hard-rock site to the reference spectrum agrees well with those observed for the 1985 Michoacan and 1983 Akita-Oki earthquakes observed under similar conditions (Houston, 1986).

These results suggest that if similar comparisons are made for events in different tectonic provinces, teleseismically determined source spectra may be used eventually to estimate strong ground motions for different tectonic regions.

Chapter 4

Teleseismic Source Parameters and Rupture Characteristics of the 24 November 1987, Superstition Hills Earthquake

Abstract

Long-period body waves from the 24 November 1987, Superstition Hills earthquake are studied to determine the focal mechanism and spatial extent of the seismic source. The earthquake is a complex event consisting of two spatially distinct subevents with different focal mechanisms. Two consistent models of rupture are developed. For both models the second subevent begins 8 sec after the initiation of the first subevent and the preferred centroid depth lies between 4 to 8 km. Model 1 consists of two point sources separated by 15–20 km along strike of the Superstition

Hills fault. Model 2 consists of one point source and one line source with a rupture velocity of 2.5 km/sec and moment-release distributed along strike of the focal plane at a distance of 10 to 22 km from the epicenter. These moment release patterns show that a significant amount of long-period energy is radiated from the southern segment of the fault. Total moment release for both models is approximately 8×10^{25} dyne-cm. Both models also suggest a change of dip from near vertical close to the epicenter to steeply dipping southwest along the southern segment of the fault. The difference in rupture characteristics and fault dips seen teleseismically is also reflected in aftershock and afterslip data, and in the crustal structure underlying the two fault segments. The northern segment had more aftershocks and a smaller proportion of afterslip than the southern segment. The boundary between the two segments lies at a step in the basement that separates a deeper metasedimentary basement to the south from a shallower crystalline basement to the north.

4.1 Introduction

The 24 November 1987, Superstition Hills earthquake sequence occurred in the western Imperial Valley in southern California. The earthquakes took place on a conjugate fault system consisting of the right-lateral, northwest-striking Superstition Hills fault and the left-lateral, northeast-striking Elmore Ranch fault (Figure 4.1). The earthquake sequence consisted of foreshocks, an M_s 6.2 mainshock, and aftershocks on the Elmore Ranch fault followed by an M_s 6.6 mainshock and aftershocks on the Superstition Hills fault (Magistrale *et al.*, 1989). The epicenter of the Superstition Hills mainshock is located near the intersection of the two faults. The Supersti-

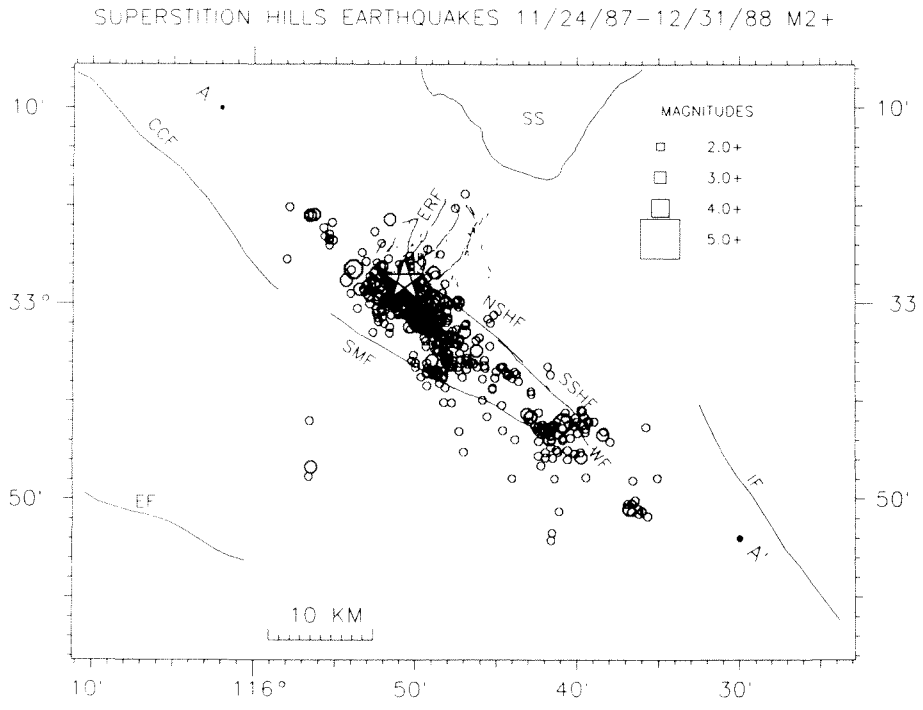

Figure 4.1: The 24 November 1987 Superstition Hills earthquake (star) and $M_L \leq 2$ aftershocks from 11/24/87 to 12/31/88. Symbol size is scaled to earthquake magnitude. AA´ is the location of the cross section shown in Figure 4.2. Earthquake location technique is described in Magistrale *et al.* (1989). The trace of the Elmore Ranch and Superstition Hills fault rupture is from Sharp *et al.*, 1989. Abbreviations: NSHF, northern segment of the Superstition Hills fault; SSHF, southern segment of the Superstition Hills fault; WF, Wienert fault; ERF, Elmore Ranch Fault; SMF, Superstition Mountain fault; CCF, Coyote Creek fault; EF, Elsinore fault; IF, Imperial fault; and SS, Salton Sea.

tion Hills fault ruptured the surface in three strands (Sharp *et al.,* 1989): the north and south segments of the Superstition Hills fault, and the Wienert fault to the south (Figure 4.1). The fault strands are separated by narrow, right steps. Previous geologic and seismologic investigations (Hanks and Allen, 1989) provide useful constraints for this teleseismic study. The strike of the surface rupture (Sharp *et al.,* 1989) constrains the plane of fault rupture, and the distribution of aftershocks (Magistrale *et al.,* 1989) indicates a depth range of moment release to investigate.

The Superstition Hills earthquake was recorded by nearby strong-motion instruments, and local and teleseismic seismic networks. Source studies of this earthquake by several authors utilize these data and provide a general picture of this earthquake over a broad frequency range. Frankel and Wennerberg (1989) inverted high-frequency, strong-motion recordings using a tomographic source-inversion technique to determine timing, location, one-dimensional extent and rupture velocity of three subevents. The effective rupture velocity between the two principal subevents, subevents 2 and 3, is very slow, but their individual velocities are greater than or equal to the shear-wave velocity of the medium, respectively. Depth was determined from waveform complexity.

Bent *et al.* (1989) forward-modeled long-period regional and teleseismic P and SH waveforms, using a method based on ray summation (Langston and Helmberger, 1975). They determined focal mechanism, depth, timing and source separation for two subevents that have different mechanisms. For their second subevent, they investigated both point and distributed source models. The solutions for the different models were not significantly different. Their preferred model explains the event as

Model	Strike (deg)	Dip (deg)	Slip (deg)	Depth (km)	Delay (sec)	Velocity (km/sec)	Distance (km)	Azimuth (deg)	Moment (dyne-cm)$\times 10^{25}$
MJK	305	90	180	2					
FW#	128	90	180	9	0				
	128	90	180	9	3	5.3	2		0.37*
	128	90	180	9	9.7	3	8		1.4*
S	303	89	-180	10	5-9		0	0	10
HRV	133	78	178	15					7.2
BHSH	305	80	175	10	0		0	0	3.6
	320	80	175	6	7.5		30	180	7.2
HMK1	120	88	194	4	0		0	0	2.4
	126	69	182	6	8.1		20	125	5.2
HMK2	122	82	194	4	0		0	0	3.1
	125	63	178	6	8.2	2.5	22.5	125	4.8

* moment at $\approx$1 Hz
\# assumed focal mechanism
MJK: Magistrale *et al.* (1989)
FW: Frankel and Wennerberg (1989)
S: Sipkin (1989)
HRV: Harvard Centroid Moment Tensor
BHSH: Bent *et al.* (1989)
HMK1: Hwang *et al.* (this study), Model 1
HMK2: Hwang *et al.* (this study), Model 2

Table 4.1: Model Parameters.

two distinct point sources separated in space and time.

Sipkin (1989) inverted teleseismic, long-period waveforms using a time-dependent, moment-tensor algorithm to resolve a time-varying moment tensor and a detailed source-time function. He modeled this earthquake with a complex source-time function consisting of two subevents, with no significant change in focal mechanism. In his model, sources were constrained to occur at the same location and focal depth. Source parameters from these studies are summarized in Table 4.1.

Several important questions are not well resolved by the above studies. No model clearly determines whether any moment release occurred on the Elmore Ranch fault

during the Superstition Hills earthquake or if all the segments of the Superstition Hills fault ruptured coseismically. Frankel and Wennerberg (1989) investigated rupture to the northeast of the epicenter along the Elmore Ranch fault. This rupture direction improved the waveform and amplitude fits to strong-motion records to the northeast, but records at other azimuths had worse or similar fits to their preferred model of rupture along the Superstition Hills fault. Wald and Somerville (1988) also propose that a subevent ruptured the Elmore Ranch fault. However, Frankel and Wennerberg (1989) point out that the lack of aftershocks along the Elmore Ranch fault following the Superstition Hills earthquake does not support rupture of the Elmore Ranch fault during the Superstition Hills earthquake. Sipkin (1989) does not consider spatial separation of subevents. Bent *et al.* (1989) placed their second subevent due south of the first subevent, but the distance between subevents is poorly resolved. If their first subevent is near the north end of the Superstition Hills fault, their preferred model would place the second subevent substantially off the surface trace of the Superstition Hills fault. Alternatively, restricting the first subevent to lie on the Elmore Ranch fault and the second subevent to lie on the Superstition Hills fault would place the first subevent at least 16 km NE from the epicenter. By using an inverse method that allows for multiple source parameterizations, we improve on the resolution of directivity, rupture velocity and spatial extent of the sources.

4.2 Method and Data Preparation

Teleseismic body waves were simultaneously inverted in a least-squares sense using the method of Nábělek (1984, 1985). This method can invert for multiple sources and

Station	Instrument	Azimuth (deg)	Distance (deg)	Type	Weight	Delay (sec)
GDH	DWWSSN	24.4	49.8	P,SH	0.70,0.60	0
KONO	ASRO	25.1	77.3	P,	0.70,	0
GRFO	SRO	31.3	85.2	P,	0.70,	1(STU)
STJ	CAND	53.2	49.0	,SH	,0.35	
GAC	SRO	55.7	33.3	P,SH	0.80,0.35	1(OTT)
SCP	DWWSSN	64.6	31.2	P,SH	0.80,0.50	*
BOG	WWSSN	116.8	48.1	P,	0.80,	1
LPB	WWSSN	129.6	67.1	,SH	,0.35	
ANT	WWSSN	136.4	71.1	,SH	,0.35	4
HON	DWWSSN	263.5	39.0	,SH	,0.60	
MAJO	ASRO	308.6	82.2	P,	1.00,	2
COL	DWWSSN	338.2	37.4	P,SH	1.00,0.60	0

* SCP had clock problems.

Table 4.2: Station list.

solves simultaneously for focal mechanism, centroid depth and source-time function for each source, as well as for the separation time, distance and azimuth between the sources. Point and line sources were investigated. Since short-period data were not well recorded for this event, only long-period data are studied. The data set consists of long-period, Global Digital Seismic Network (GDSN), Worldwide Standard Seismograph Network (WWSSN), and Canadian Network (CAND) P and SH waveforms (see Table 4.2) restricted to the distance range $30° \leq \Delta \leq 90°$ for P waves and $30° \leq \Delta \leq 80°$ for SH waves to avoid regional and core effects. WWSSN and CAND data were digitized using an optical scanner, resampled at intervals of 0.25 sec and corrected for drift.

Absolute timing of the P-wave arrival to each station is very important to resolve spatial extent and relationship between sources. Since this event was not

well recorded on short-period instruments, the 1968 Borrego Mountain earthquake (M=6.8) is used as a master event to compute travel-time delays. The 1987 Superstition Hills earthquake occurred close to the epicenter of the 1968 Borrego Mountain earthquake in a similar geologic setting. The Borrego Mountain earthquake was an impulsive event and well recorded worldwide. P-wave delay times are determined by subtracting the theoretical P-wave arrival times calculated from a Herrin earth model (Herrin, 1968) from the Borrego Mountain earthquake arrival times reported in the *International Seismic Centre Bulletin.* Since current station sites were not all occupied in 1968, arrival times to stations at similar azimuth and distance were used as noted in Table 4.2. Only one S-wave delay was available. P- and S-wave delays are given in Table 4.2. These delays are added to the theoretical travel times for the Superstition Hills earthquake. In the inversion, the calculated and observed seismograms are not allowed to shift in time with respect to one another. However, seismograms from stations for which there is no S-wave delay are allowed to shift ± 10 sec. In the final solution, the seismograms shifted no more than ± 5 sec relative to one another. For station SCP, the P-wave arrival for events during the month of November 1987 are systematically much later than the reported ± 1 sec clock error. After studying waveforms from these other events, 10 sec were added to the theoretical arrival time. It did not move from this time in the final solution.

The crustal velocity structure for the source region (Table 4.3) was taken after Fuis *et al.* (1982). This crustal velocity structure is intermediate between a velocity model of thick sediments overlying a metasedimentary basement, characteristic of the central Imperial Valley east of the Superstition Hills fault, and a velocity model

Thickness (km)	Depth (km)	P-Wave Velocity (km/sec)	S-Wave Velocity (km/sec)	Density (g/cm^3)
1.5	0.0	2.5	1.4	2.3
1.5	1.5	4.5	2.6	2.6
9.5	3.0	6.2	3.6	2.6
12.5	12.5	7.0	4.0	3.1
	25.0	7.9	4.6	3.3

Table 4.3: Velocity model.

representing thinner sediments over a granitic basement, as is typical to the northwest of the Superstition Hills fault (Fuis *et al.,* 1982). The modeling results are only mildly sensitive to the source crustal model used.

Data from the Southern California seismograph network define the source dimensions and location of this event (Magistrale *et al.,* 1989). In the inversion, the locally determined focal mechanism (strike 305°, dip 90°, slip 180°) was used as the starting mechanisms. The nucleation point of the first subevent is constrained to the locally determined hypocentral depth of 2 km, but the centroid depth is allowed to vary. Aftershock data define the bottom of the seismogenic zone at a depth of 12 km, and extend this zone to a distance of 30 km striking NW-SE along the Superstition Hills fault (Figure 4.2). Multiple sources were constrained to lie along the fault plane with rupture velocities up to the shear-wave velocity of the medium, 3.5 km/sec. Sources along the Superstition Hills and Elmore Ranch fault were investigated for Subevent 1. The depth, distance and velocity ranges given above are systematically searched for the best solution, assuming that the source-time function has a total duration of approximately 15 sec on the basis of inspection of the waveforms. A

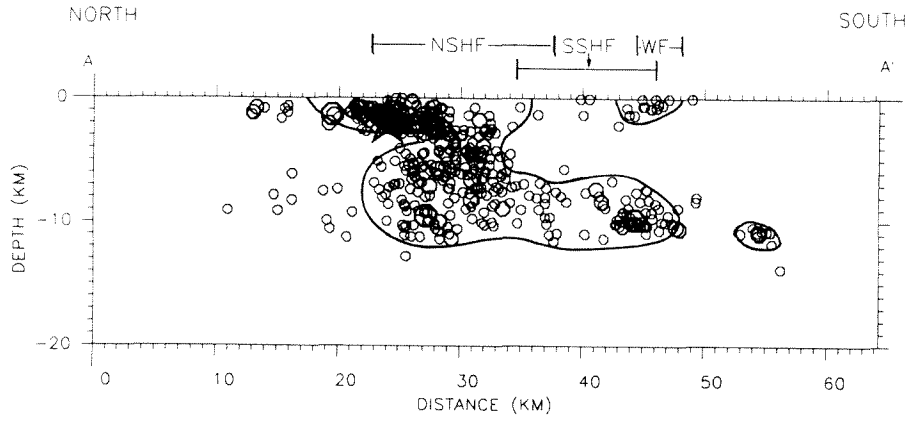

Figure 4.2: Cross section parallel to the Superstition Hills fault. All events in Figure 4.1 within 10 km of cross section are projected onto the cross section. The aftershock zone is outlined. Earthquake symbols and abbreviations are the same as in Figure 4.1.

series of overlapping triangular time functions with a 1 sec rise time was used in modeling the source-time function.

4.3 Modeling Results

The size and station distribution for this event limit the spatial resolution and resolvable detail, using long-period data. Sipkin (1989) suggests that a time-variable, single-source model may fit the long-period data as well as the two-source model proposed by Bent *et al.* (1989). However, the various single point and single line source models investigated here were unable to explain the data. A two source model provides a much better fit. For Subevent 1, centroid locations along the Elmore Ranch fault were tested. Data misfits increase as Subevent 1 is moved farther away from

the epicenter. However, a point source within 10 km of the epicenter is unresolvable from a point source at the epicenter. Either moment release along the Elmore Ranch fault during Subevent 1 was not a substantial portion of the long-period moment release, or it occurred within 10 km of the epicenter. In our final models, Subevent 1 is a point source located at the epicenter. Since the epicenter lies near the intersection of the Elmore Ranch and Superstition Hills fault, the choice of fault plane is ambiguous. For the sake of discussion, we chose the NW-SE trending fault plane.

Investigation of various double source models suggests two possible source parameterizations. Model 1 consists of two temporally and spatially separate point sources. The spatial separation of the two sources is investigated by moving Subevent 2 in 5 km intervals southeast of Subevent 1 along the strike of the fault, 305°. Model 2 consists of one point source and one delayed, propagating line source. Rupture velocity was modeled at 0.5 km/sec intervals. In Model 2, the line source remains within a specified focal plane that changes orientation during the inversion. Both final solutions for these two source models fit the waveforms adequately. Final solutions for the two models are given in Table 4.1, and waveforms are illustrated in Figures 4.3, 4.4, 4.5, and 4.6.

A summary of data misfits with respect to centroid depth for both models is given in Figure 4.7. Errors shown for Model 1 (Figure 4.7a and 4.7b) are for a fixed source separation of 20 km. Errors shown for Model 2 (Figure 4.7c and 4.7d) are for a rupture velocity of 2.5 km/sec for Subevent 2. Along each curve in Figure 4.7a and 4.7c, the centroid depth for Subevent 2 is fixed, and the depth for Subevent 1 is allowed to vary. The depth of Subevent 1 is plotted along the x-axis and the depth

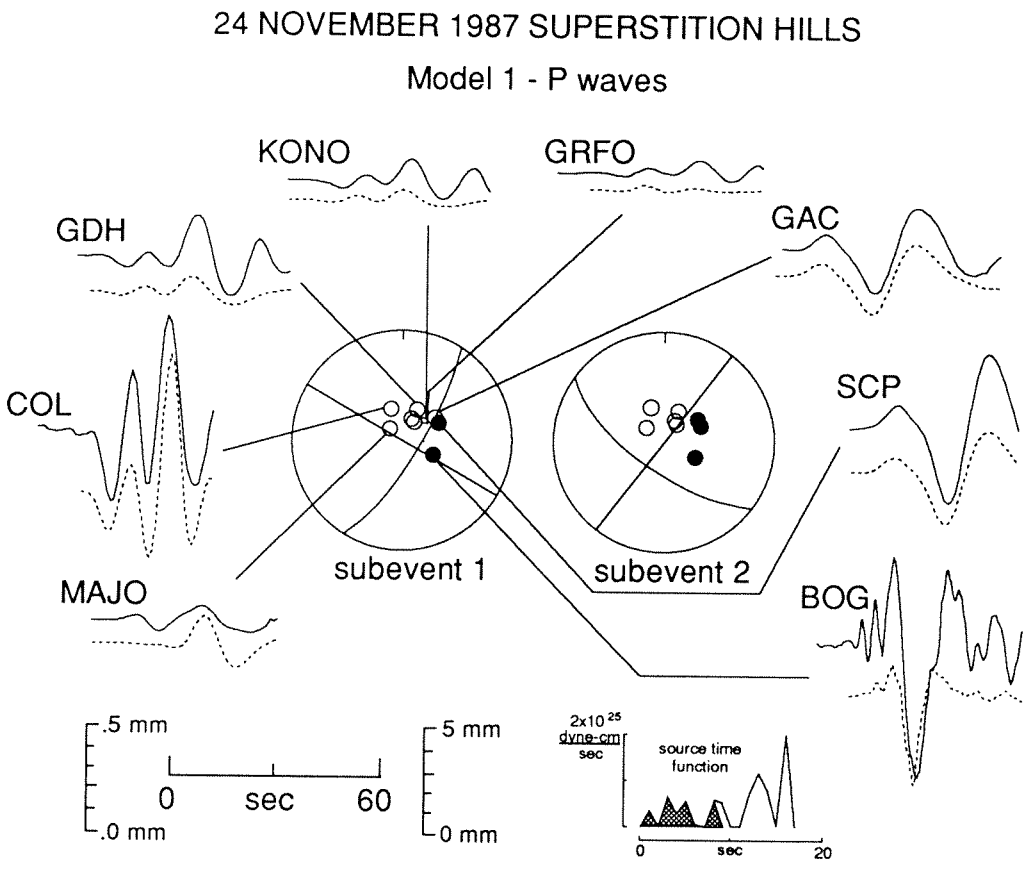

Figure 4.3: Model 1. Observed (solid lines) and synthetic (dashed lines) long-period P-wave seismograms. Shown in the center of the figure is the lower hemisphere focal mechanism for the two subevents. Solid circles represent compressional, and open circles, dilatational first motions. Focal parameters are given in Table 4.1. The combined source-time function for Subevent 1 (shaded), and Subevent 2 (unshaded) is shown at bottom right. Time and amplitude scales are shown at bottom left. Separate amplitude scales are given for analog (left) and digital (right) instruments. Amplitudes of the observed and synthetic seismograms are normalized to the identical instrument with a peak magnification of 1500 at a distance of 40°.

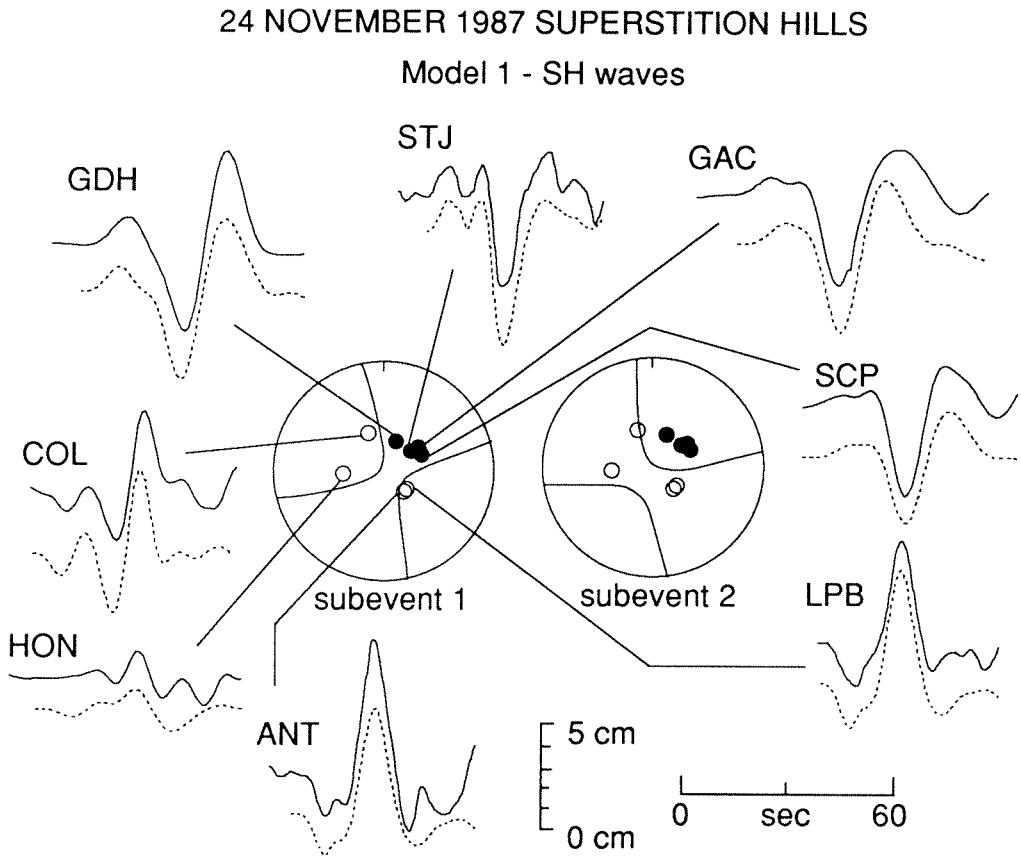

Figure 4.4: Model 1. Observed (solid lines) and synthetic (dashed lines) long-period SH-wave seismograms. Amplitude scales are the same for analog and digital instruments. Symbols are described in Figure 4.3.

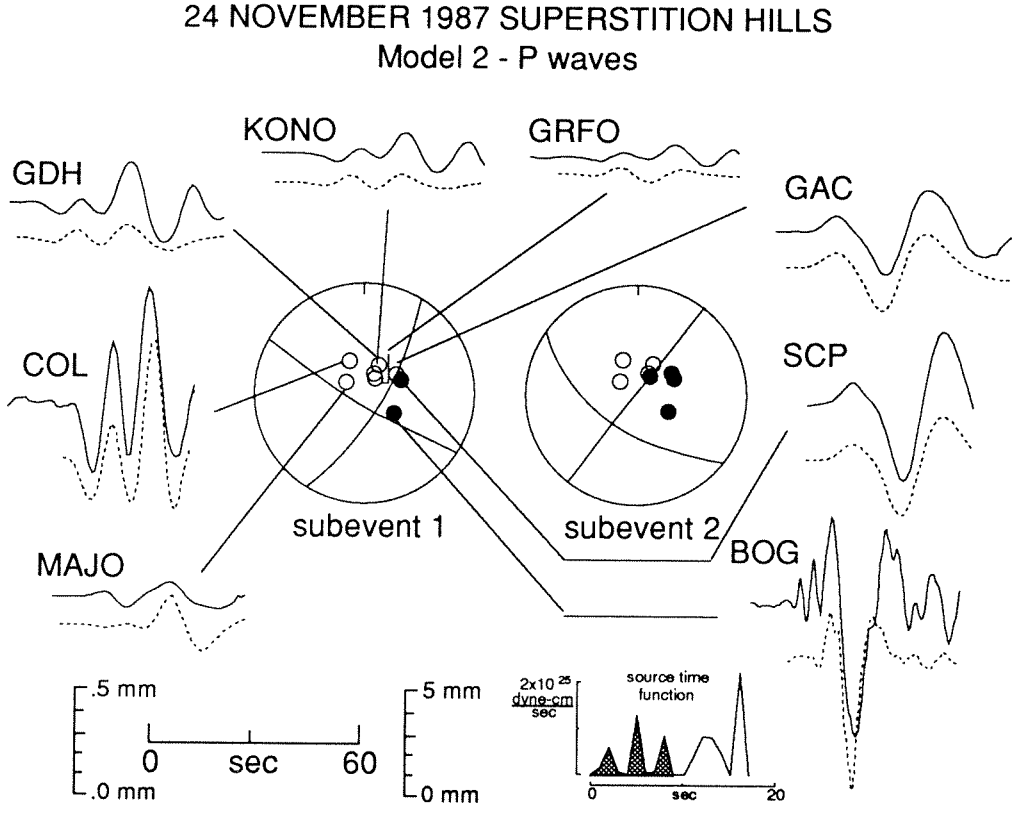

Figure 4.5: Model 2. Observed (solid lines) and synthetic (dashed lines) long-period P-wave seismograms. Symbols are described in Figure 4.3.

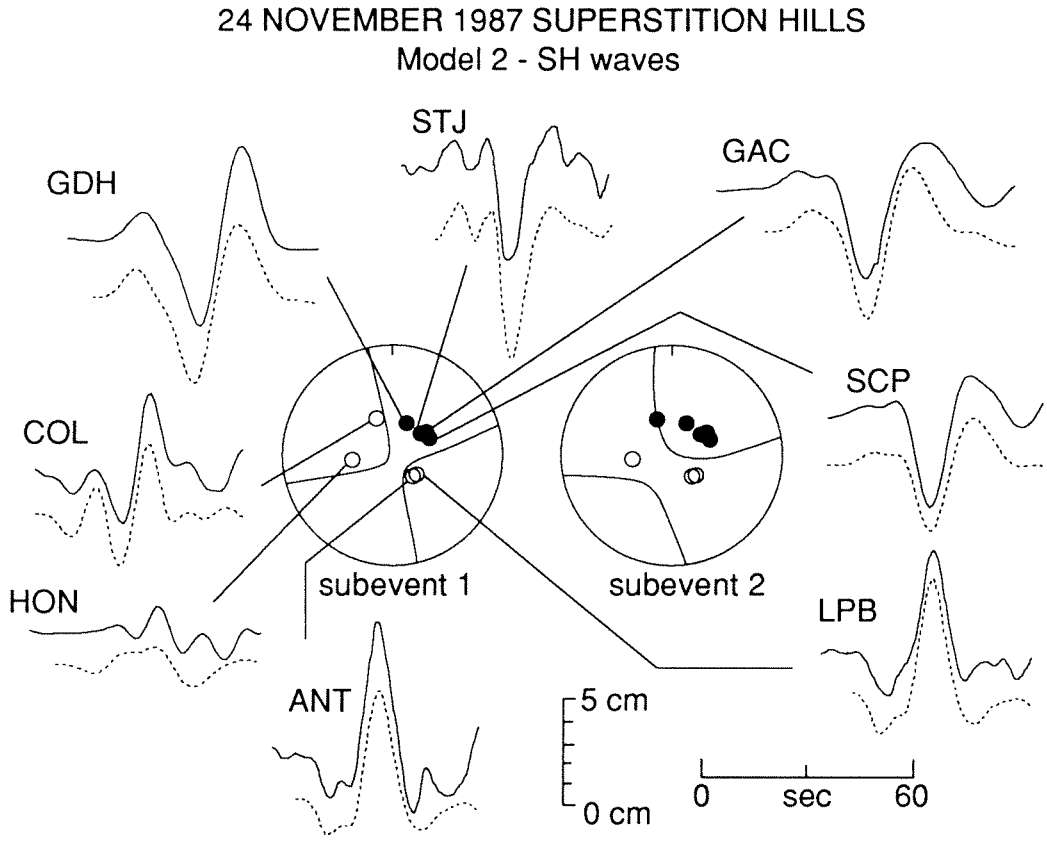

Figure 4.6: Model 2. Observed (solid lines) and synthetic (dashed lines) long-period SH-wave seismograms. Amplitude scales are the same for analog and digital instruments. Symbols are described in Figure 4.3.

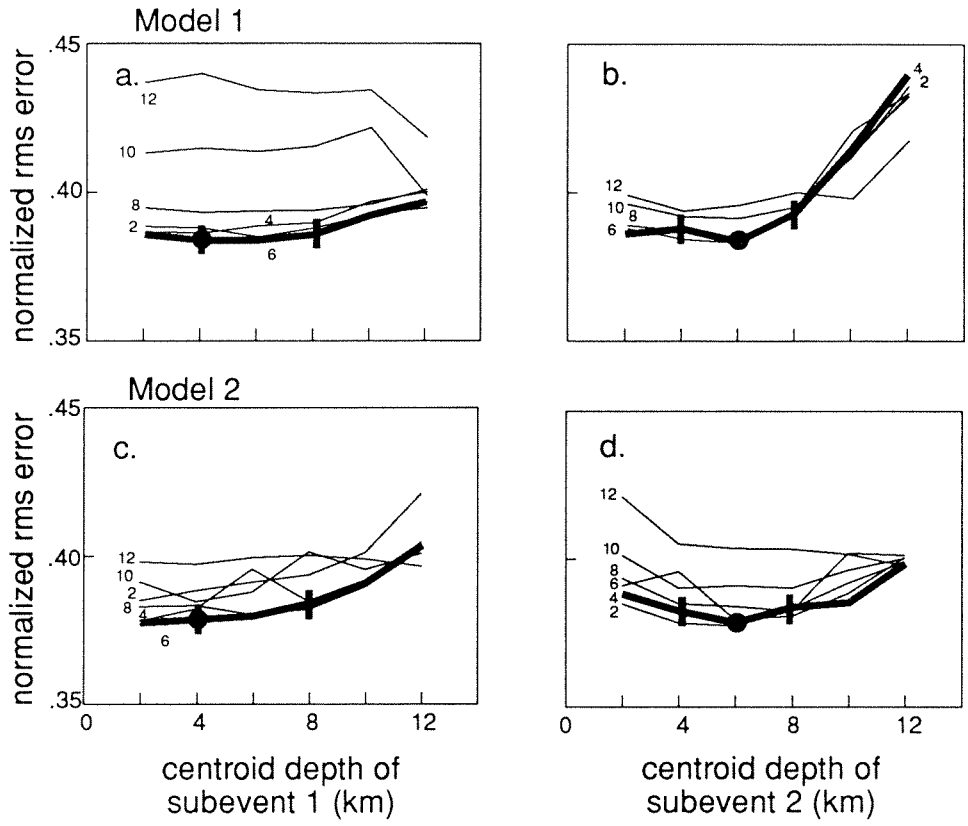

Figure 4.7: Data misfits for Model 1 and Model 2. Plotted is the normalized rms error versus centroid depth for the two subevents. Errors for Model 1 (4.7a and 4.7b) are for a source separation of 20 km. Errors for Model 2 (4.7c and 4.7d) are for a rupture velocity for Subevent 2 of 2.5 km/sec. For each curve in Figure 4.7a and 4.7c, the depth of Subevent 2 is held constant, while the depth of Subevent 1 is allowed to vary. The depth of Subevent 1 is plotted along the x-axis and the depth of Subevent 2 is as labeled on each curve. Depths for both subevents range from 2 to 12 km. Similarly, for each curve in Figure 4.7b and 4.7d, the depth of Subevent 1 is held constant, while the depth of Subevent 2 is varied. Drawn with a bold line is the curve that contains our preferred solution. In Figure 4.7a and 4.7c, this curve is for a depth of 6 km for Subevent 2 and in Figure 4.7b and 4.7d, for a depth of 4 km for Subevent 1. The large dot marks the depth of the preferred solution, and the bars delineate the acceptable depth range.

of Subevent 2 is as labeled on each curve. The depth for both subevents is fixed at 2 km intervals over a range of 2 to 12 km. Similarly, along each curve in Figure 4.7b and 4.7d, the centroid depth for Subevent 1 is fixed, and the depth of Subevent 2 is allowed to vary. Focal mechanism, source-separation time, and the source-time function are determined in the inversion.

The final solution is chosen to lie along the curve with the overall lowest error level for both subevents (bold line) in Figure 4.7. As shown in Figures 4.7a and 4.7c, the centroid depth for Subevent 1 is not a robust feature. In Figures 4.7b and 4.7d, the solutions with the smallest errors for Subevent 2 range from 4 to 8 km in depth. This is the preferred depth range for both subevents and for all source models considered. The best solution marked by a large dot in Figure 4.7 occurs when the centroid depth for Subevent 1 and Subevent 2 is 4 and 6 km, respectively. This solution has the lowest error of all solutions tested.

In the inversion, formal errors for each solution are small. A more realistic estimation of the model errors is determined from the range of acceptable least error solutions. In Model 1, Subevent 2 occurs at a distance of 15–20 km from Subevent 1. In Model 2, the rupture velocity may be as low as 1.5 km/sec, but a velocity of 2.5 km/sec is preferred since the overall level of data error is lower. This velocity is 0.7 times the shear-wave velocity in the layer. Within the above depth, distance and velocity ranges, the strike is well constrained to $\pm 1°$, and the dip and rake are resolved to approximately $\pm 5°$ for both models and subevents.

Overall waveform and amplitude match between both models and the data are good. Only HON (S wave) and MAJO (P wave) are ill-matched. Unfortunately,

these stations lie near nodes and are the only data that lie west of the Superstition Hills fault. Using a faster crustal structure more appropriate for the western side of the Superstition Hills fault has no significant effect on the waveforms or the focal mechanism solution. To further explore the range of solutions, we force a fit by overweighting HON and MAJO by 20 times the maximum weight in the inversion.

The resulting model has two main differences from our final solutions. The first difference is in fault dip. Subevent 1 now dips to the east and Subevent 2 has a near-vertical dip. Hence, stations to the west appear to prefer dips near vertical while stations to the east prefer a westward dip of 70°. A conservative estimate would place the dip between 70–80° to the west. This estimate is consistent with the magnitude and dip direction of the focal mechanism determined in the Harvard Centroid Moment Tensor (CMT) solution but opposite in direction to the model of Bent *et al.* (1989) (see Table 4.1). The second difference is the change in the source-time function. The net effect is to decrease the time between Subevent 1 and the largest moment-releasing episode in Subevent 2. That is, to explain the waveforms at HON and MAJO, the travel time between the two subevents must be less than the travel time to the remainder of the stations. This suggests that the different source structure on the opposite sides of the Superstition Hills fault has some effect on the final solution. However, since both stations are located near nodes, this possibility is difficult to explore. Additional data to the west away from P-wave nodes are needed to illustrate more clearly any crustal effects.

For both models, the source-time functions of each subevent have very little or no overlap and are very irregular. Irregularity can be attributed to the particular

parameterization used in the inversion, which does nothing to insure the smoothness of the rupture process. Source elements with a longer time duration can be used to achieve an overall smoother, source-time function with some deterioration of waveform match. The total moment for both models is less than but in good agreement with that of Bent *et al.* (1989) and Sipkin (1989) and comparable to the Harvard CMT solution (Table 4.1). Total moment corresponds to $M_w = 6.5$.

4.4 Discussion

Figure 4.8 summarizes the fault rupture models in this and previous studies along with aftershock, afterslip, and structural data. Symbols as noted in the figure represent point sources for different models. Line sources are represented by bold arrows.

In the present study, both Model 1 and Model 2 give a reasonable fit to the data. Both solutions indicate a steep, westerly dipping fault plane for Subevent 1, and a 70° westerly dipping fault plane for Subevent 2. The western dip agrees broadly with the location of the aftershocks to the west of the surface trace of the fault (Figure 4.1). In both models, the centroid for Subevent 1 lies at or near the epicenter. Subevent 1 nucleates at a depth of 2 km but has a centroid depth of 4 km. Most of the moment release for Subevent 2 lies along the southern segment of the Superstition Hills fault at a depth of 6 km. For Subevent 2, Model 1 places a point source between 15–20 km southeast of Subevent 1 along the strike of the fault. Model 2 distributes the source along a line at a distance of 10 to 22 km southeast from Subevent 1. Assuming a lower rupture velocity of 1.5 km/sec would move this to a distance of 6 to 14 km. This lower distance bound is illustrated by a bold

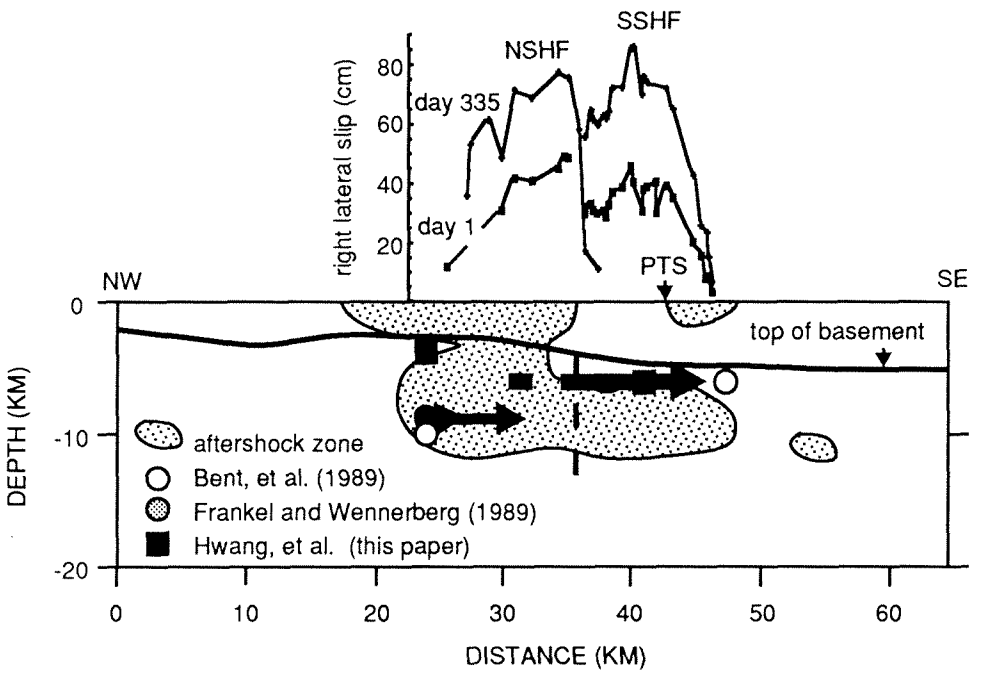

Figure 4.8: Northwest-southeast cross section parallel to the Superstition Hills fault summarizing fault rupture models and slip history along the fault. The top figure shows afterslip plotted along the fault for 1 day and 335 days after the earthquake (after Williams and Magistrale, 1989). The bottom figure outlines the aftershock area (thin line, see Figure 4.2) and basement topography (bold line, after Kohler and Fuis, 1986). The bold dashed line separates crystalline basement to the north (left) from metasedimentary basement to the south (right). Symbols as noted in the figure show source location and lateral extent for rupture models from this study and from previous studies. Abbreviations: PTS, Parachute Test Site; others are as noted in Figure 4.1. See Table 4.1 for source parameters.

dashed line in Figure 4.8. The upper distance bound, 22 km, agrees with the extent of surface rupture along the Superstition Hills fault (Sharp *et al.,* 1989). Moment release along the southern segment accounts for 2/3 of the total moment release for this earthquake. No significant moment release is seen along the Wienert fault.

The timing of the two subevents proposed by Bent *et al.* (1989) correlates with the timing of the two subevents in Model 1 and Model 2, but their locations differ substantially. Bent *et al.* place their second subevent due south of their first subevent at a preferred separation of 30 $\pm$10 km. Constraining the first subevent to lie along the Elmore Ranch fault and the second subevent to lie along the Superstition Hills fault would place their first subevent between 16 and 33 km northeast of the epicenter and their second subevent between 11 and 31 km southeast of the epicenter. A distance greater than 10 km northeast from the epicenter for the first subevent is not supported by this study. The lack of afterslip and aftershocks also does not support a large, moment-releasing, first subevent along the Elmore Ranch fault (Frankel and Wennerberg, 1989). Placing Bent *et al.'s* (1989) first subevent on the Superstition Hills fault would make a correlation of the second subevent with the surface trace of the Superstition Hills fault difficult.

The model of Frankel and Wennerberg (1989) shows some similarities to Model 1 and Model 2. Our Subevent 1 correlates with their subevent 1 and 2, where their subevent 1 represents the nucleation point of the earthquake. The timing of their subevent 3 correlates with our Subevent 2 but the two source positions differ. Slip for their subevent 3 starts at 0 km and does not extend past 8 km (see Figure 4.8), even though surface rupture went well beyond this point. Also, total moment for

their model is 1/6 of what is observed at long periods (see Table 4.1). Hence, their model may not account for all of the slip along the fault.

Model 1 and Model 2 are still consistent with the raw strong-motion data. The record from PTS located 18 km from the epicenter on the Superstition Hills fault suggests that significant moment release did not go beyond that station (Frankel and Wennerberg, 1989). Even though surface rupture continued along the trace of the fault out to 24 km, the magnitude of surface slip died off rapidly beyond PTS (see Figure 4.8). This distance falls within the range of our estimate of the position and extent of Subevent 2 in both models. If the maximum extent for Subevent 2 is 18 km, it would imply a slightly slower rupture velocity of 2.25 km/sec in Model 2. The strong-motion data also indicate directivity towards the northeast along the Elmore Ranch fault (Frankel and Wennerberg, 1989; Wald and Sommerville, 1988). Any moment release within 10 km of the epicenter along the Elmore Ranch fault is not resolvable from the long-period data.

Figure 4.8 compares the depth of moment release determined here, 4 to 8 km, to the depth distribution of the aftershocks. The aftershocks lie mostly between 1 to 11 km depth. Along the northern segment of the fault, relatively few aftershocks lie between 2.5 to 5 km depth, or in the south between 2 to 8 km. This is in agreement with studies of slip distribution along faults that find fewest aftershocks in areas of greatest slip (Doser and Kanamori, 1986: Mendoza and Hartzell, 1988) and greatest moment release (Schwartz *et al.,* 1989) on the fault plane. Here we assume that regions of greatest moment release correspond to areas of high slip. The centroid depths of both subevents in this study are generally shallower than the

depths determined in the previous studies.

The model of Frankel and Wennerberg (1989) suggests that high-frequency energy radiated predominately from the northern end of the fault. Combined with the results from Models 1 and 2, this indicates that both high-frequency and low-frequency energy radiated in the epicentral region along the northern segment of the Superstition Hills fault, while only low-frequency energy radiated from the southern segment. This also agrees with previous studies that propose a different behavior for the two fault segments. In Model 1 and Model 2, the northern segment dips near vertically and the southern segment dips steeply towards the west. The northern segment had a smaller proportion of afterslip than the southern segment (Williams and Magistrale, 1989), and more aftershocks (Magistrale *et al.*, 1989). The boundary between the northern and southern segments lies at a step in the basement. This step separates the deeper sediments (4 to 5 km thick) of the southern segment that overlie metasedimentary basement from the thinner sediments (2 km thick) of the northern segment, which overlie crystalline basement (Figure 4.8).

4.5 Conclusion

We inverted teleseismic body waves of the 24 November 1987 Superstition Hills earthquake using the method of Nábělek (1984,1985). We obtained two multiple-source models. In both models, Subevent 2 begins 8 sec after the initiation of Subevent 1 and has 2/3 of the total moment. The total moment for both models is approximately 8×10^{25} dyne-cm. In Model 1, the first point source occurs under the epicenter, followed by a second point source 15 to 20 km away, southeast along strike of the

fault. In Model 2, the first point source is followed by a line source of 8 sec duration, rupturing southeast at 1.5 to 2.5 km/sec. Sources for both models are between 4 to 8 km depth. The fault dip changes from near vertical near its northern end to about 70° near its southern end.

Moment release for Subevent 1 occurs in the epicentral region and radiates both short- and long-period energy. A small portion of the Elmore Ranch fault (<10 km) may have reruptured during Subevent 1, or alternatively, all moment release for both subevents was confined to the Superstition Hills fault. The second subevent ruptured the southern segment of the Superstition Hills fault, radiating a substantial portion of the long-period energy resolved in this study. The difference in rupture characteristics and fault dips seen teleseismically is also reflected in aftershock and afterslip data, and crustal structure underlying the two fault segments.

Chapter 5

The 1987-88 Gulf of Alaska Sequence

Abstract

Three large earthquakes occurred in the Gulf of Alaska during 1987-88: one on 17 November 1987 (M_w = 7.2), the second one on 30 November 1987 (M_w = 7.8), and the third one on 6 March 1988 (M_w = 7.7). These major intraplate, strike-slip oceanic events occurred along conjugate trends in a region of no previous seismicity. Body-wave modeling places their centroid depths in the upper mantle. The depth of the first two events is approximately 20 km and the third is 15 km. As compared to other large events, the body-wave models for the two largest earthquakes have short rupture lengths, 110 km and 40 km, respectively, and short duration times, 36 and 20 sec, respectively, for their magnitude. The latter of the two events has a rupture length much shorter than that inferred from aftershock seismicity. The short rupture lengths and source durations may reflect differences between the strength of oceanic and continental lithosphere and suggest that events in oceanic lithosphere have a higher moment release per unit area than similar continental events. Most of the

moment release occurred near the epicenter and/or regions of apparent structural complexities where seismicity trends intersect.

5.1 Introduction

The 1987-88 Gulf of Alaska sequence consists of 3 large earthquakes with magnitudes of 6.9, 7.6 and 7.6 M_s (NEIC), respectively, occurring during November 1987 to March 1988 that were felt throughout southern Alaska. All three earthquakes lie within the Pacific plate outboard of the continental shelf margin and the Aleutian trench axis, in a region with no previous seismic activity (Figure 5.1). In general, large oceanic intraplate events are not common and usually involve normal or thrust faulting away from the trench within the unsubducted portion of the plate. This earthquake sequence is unique because of its mode of faulting — conjugate strike-slip along cross-cutting fault planes and its position away from major structural boundaries within oceanic crust.

Large strike-slip earthquakes along plate boundaries often have rupture lengths on the order of several hundred kilometers. Surface rupture for the 1976 Guatemala earthquake (7.5 M_s) was observed along 230 km of the fault (Plafker, 1976); the 1958 southeast Alaska earthquake (7.9 M_s) had a rupture length of at least 280 km (Plafker *et al.*, 1978); and the 1972 Sitka earthquake (7.6 M_s), a length of approximately 200 km (Perez and Jacob, 1980). One exception is the 1989 Macquarie Ridge (M_s=8.2) earthquake, which had a relatively short rupture length of < 200 km. In comparison, the two largest Gulf of Alaska earthquakes also had relatively short rupture lengths. As inferred from aftershock seismicity, the two largest Gulf of Alaska

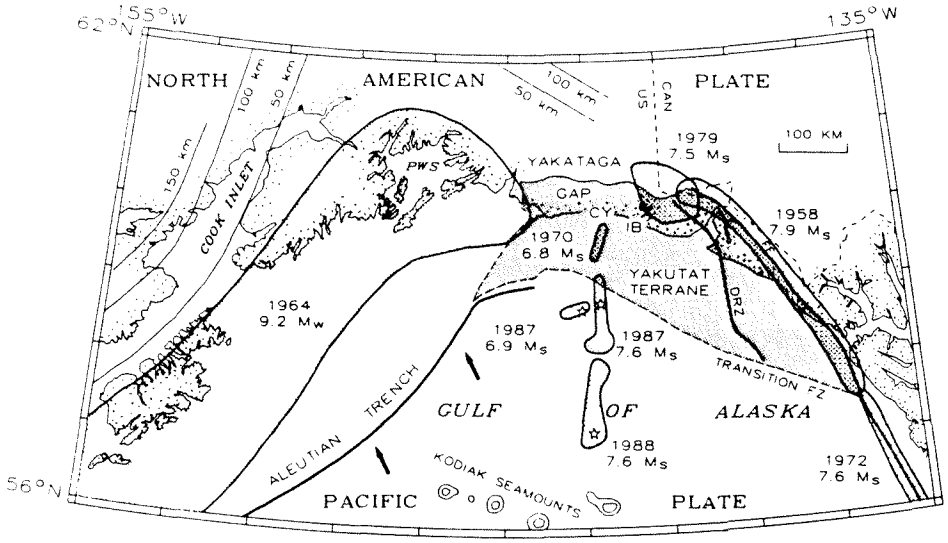

Figure 5.1: Map of the Gulf of Alaska region showing locations of recent shocks (epicenters shown as stars) in relation to the Pacific and North American plates, Yakutat terrane (dark shading), rupture zones of large historic earthquakes (light shading), Yakataga seismic gap, and Aleutian and Wrangell Wadati-Benioff zones (depth contours on top of zone). Heavy arrows show relative motion of Pacific plate with respect to North American plate (Minster and Jordan, 1978). PWS = Prince William Sound; DRZ = Dangerous River zone (Plafker, 1987); IB = Icy Bay; CY = Cape Yakataga; FF = Fairweather fault. (From Lahr *et al.,* 1988.)

events both activated zones less than 140 km in length. This suggests that these intraplate events have either relatively larger amounts of slip and/or a deeper extent of faulting.

Large strike-slip earthquakes in oceanic crust are rare and their depth of faulting is poorly understood. Estimates of depth for the 1989 Macquarie Ridge earthquake, a large oceanic interplate strike-slip event, vary from 10 to 50 km (Anderson and Zhang, 1990; Braunmiller and Nábělek, 1990; Dziewonski and Zwart, 1990; Ekström and Romanowicz, 1990; Kedar and Tanimoto, 1990; Tichelaar and Ruff, 1990). In general, seismicity for interplate strike-slip faults in both continental and oceanic environments is quite shallow and does not extend below 15 km. Hence, rupture is assumed to be restricted to the crust. Some intraplate oceanic events have been observed at greater depths (Wiens and Stein, 1983; Engeln *et al.*, 1986) suggesting failure of the upper mantle in some regions as well. For oceanic intraplate earthquakes, the maximum depth of seismicity is approximately equal to the flexural elastic thickness of the lithosphere (Wiens and Stein, 1983). On the basis of the lithospheric cooling model of Parsons and Sclater (1977), an age range of 25-50 My determined from magnetic anomalies suggests source depths of up to 30 km in the northern Gulf of Alaska. Hence, an assumed depth of 10 km (Lahr *et al.*, 1988) for these events may be too shallow. Both depth and lateral extent of faulting are important parameters in the investigation of crustal processes and the assessment of future seismic hazard in the northern Gulf of Alaska region.

Strike-slip earthquakes within populated regions have caused enormous casualties and economic damage. The 1976 Tangshan earthquake (7.7 M_s) virtually de-

stroyed the city and killed over 250,000 people. The 1976 Guatemalan earthquake (7.5 M_s) caused extensive damage and loss of life — over 22,700 people were killed (Espinosa *et al.,* 1976). Both of these events had complex multiple sources and long source durations best described using multiple subevents with different mechanisms (Butler *et al.,* 1979; Kikuchi and Kanamori, 1990). The Gulf of Alaska events fortunately occurred well offshore, causing minimal damage to structures and no loss of life (NEIC). Knowledge of the temporal-spatial distribution of heterogeneities along strike-slip faults such as the San Andreas is important in understanding the damage caused by strong ground motions during large, strike-slip earthquakes.

The large number of investigations of the 1976 Guatemalan earthquake illustrate how difficult it is to resolve source parameters for large strike-slip earthquakes reliably (Kanamori and Stewart, 1978; Kikuchi and Kanamori, 1982; Young *et al.,* 1989; Kikuchi and Kanamori, 1990). In comparison to normal or reverse faulting events, the radiation pattern for strike-slip earthquakes changes rapidly with azimuth. Hence, many teleseismic stations lie near nodes of the P-wave radiation pattern. Since amplitude changes the most rapidly near nodes, waveforms from these stations are very sensitive to position of the nodal lines with respect to the station. The P-wave radiation from strike-slip earthquakes is also more sensitive to lateral variations in the crustal structure (Langston, 1977). If azimuthal coverage is not good, arrivals that are due to crustal heterogeneities can be mistaken for source effects. When available, S-wave data help to constrain the focal mechanism of the source. Unfortunately, for large earthquakes, S-wave data are not always available, since S-wave amplitudes often exceed the dynamic range of the instruments.

Since large strike-slip earthquakes are not common within the modern instrumental records, studying the 1987-88 Gulf of Alaska sequence is important in understanding strike-slip earthquakes as well as in evaluating modern inversion techniques. Here, two multiple-source inversion techniques are used to analyze the waveform data. As described later, the techniques of Nábělek (1984, 1985) and Kikuchi and Kanamori (1990) are used to study the tradeoffs and resolution of each method in resolving the source parameters of the Gulf of Alaska events and their relationship to regional tectonics and seismicity.

5.2 Regional Setting and Seismicity

The northern Gulf of Alaska lies near a major change in the plate boundary between the Pacific and North American plate (Figure 5.2). Along this boundary the North American plate, the Pacific plate, and a series of accreted terranes interact (Perez and Jacob, 1980). The Queen Charlotte Islands-Fairweather fault system marks the active eastern plate boundary between the North American and Pacific plates. Right-lateral movement between these plates along the Queen Charlotte Islands fault trends northwest, following the oceanic-continental interface offshore the coast of British Columbia and southeastern Alaska. Near Cross Sound, the active plate margin continues onshore as the Fairweather fault. Movement along the Queen Charlotte Islands-Fairweather fault system ranges between 4.8-5.8 cm/yr (Minster and Jordan, 1978; Plafker *et al.,* 1978; Perez and Jacob, 1980) along with a small component of convergence (Lahr and Plafker, 1980; Perez and Jacob, 1980).

The northern plate boundary follows the Aleutian trench. Along this margin, the

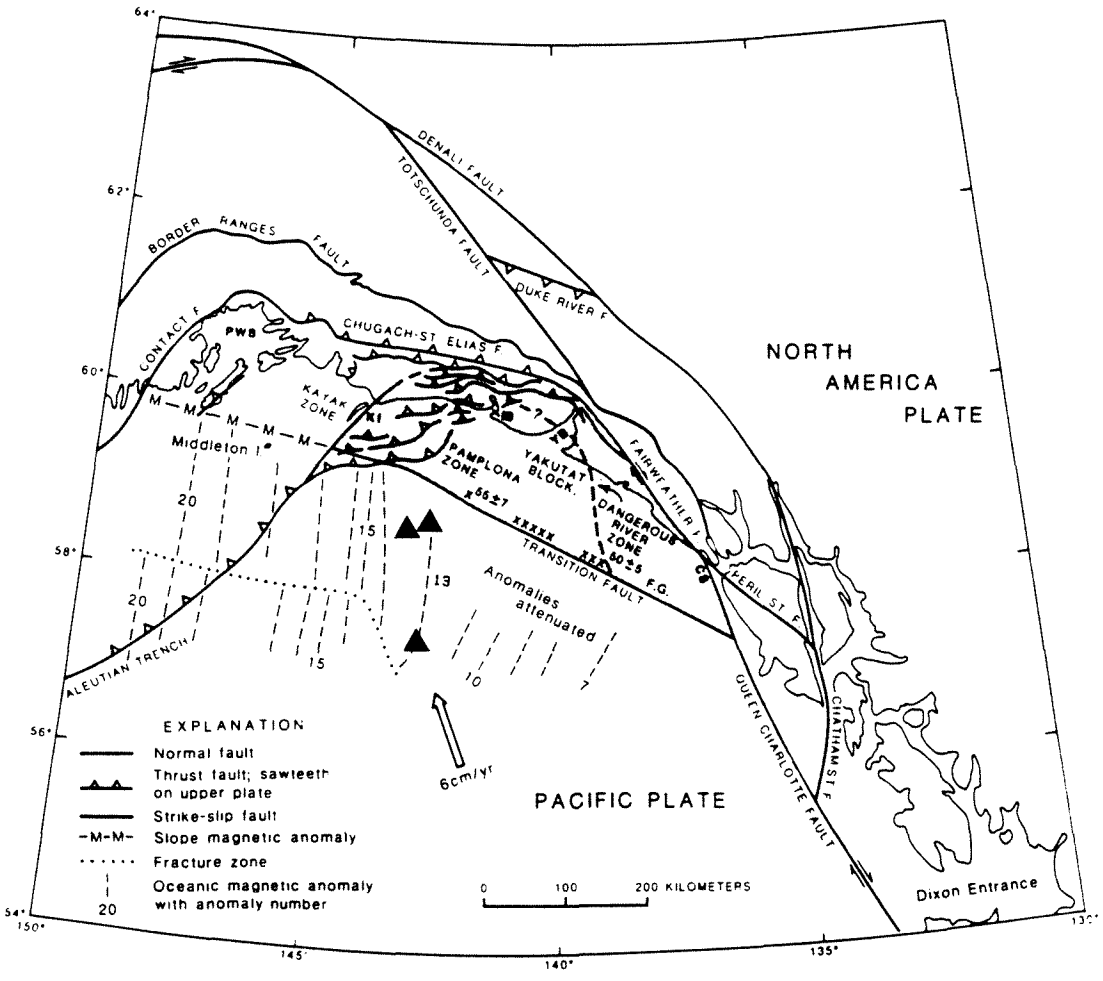

Figure 5.2: Tectonic setting of the northern Gulf of Alaska showing magnetic anomalies, major structural features and the three largest earthquakes in the 1987-88 Gulf of Alaska sequence. Stippled area shows the extent of the Yakutat block. Slope magnetic anomaly shows south edge of subducted block. X's indicate where basalt has been dredged from the continental slope; ages from Pflaker *et al.* (1980). Large arrow indicates current Pacific-North America relative convergence vector (Minster and Jordan, 1978). CS = Cross Sound; FG = Fairweather Ground; IB = Icy Bay; KI = Kayak Island; PWS = Prince William Sound; YB = Yakutat Bay. After Bruns (1983).

Pacific plate subducts under the North American plate at a rate of about 6 cm/yr in the southern Alaska region (Minster and Jordan, 1978). Movement occurs along a complex zone of northward dipping thrust faults called "the Aleutian megathrust" (Plafker, 1969).

In between these two regions, the plate boundary becomes diffuse. It is represented by a series of thrust faults belonging to the Chugach-St. Elias fault system (Plafker *et al.,* 1978; Lahr and Plafker, 1980; McCann *et al.,* 1980; Perez and Jacob, 1980). These faults join the Aleutian megathrust along the Kayak zone to the south (Bruns, 1979; Schwab *et al.,* 1980; Bruns and Schwab, 1983) and intersect the Fairweather fault near Yakutat Bay to the west. Collision of buoyant borderland terranes onto the North American plate along a series of thrust and reverse faults in southern Alaska results in major orogenies (Perez and Jacob, 1980). The Chugach-St. Elias fault zone represents a region of major crustal shortening and uplift (Stoneley, 1967; Plafker, 1971). Currently, the Yakutat block is actively accreting onto the North American plate along this margin (Plafker *et al.,* 1978; von Huene *et al.,* 1979; Lahr and Plafker, 1980; Perez and Jacob, 1980).

The Yakutat block is a composite oceanic and continental terrane (Bruns, 1979, 1983; Plafker *et al.,* 1980; Bruns and Schwab, 1983). It is bounded by the Chugach-St. Elias fault system, Fairweather-Queen Charlotte Islands fault system, the Transition fault, and the Kayak zone (Plafker *et al.,* 1978; von Huene *et al.,* 1979; Bruns, 1979, 1983; Bruns and Schwab, 1983; Plafker, 1983). The Yakutat block has moved with the Pacific plate during the Pliocene and Quaternary (Von Huene *et al.,* 1979; Schwab *et al.,* 1980; Bruns, 1979, 1983; Bruns and Schwab, 1983). Continued move-

ment thrusts the leading edge of the Yakutat block under the North American plate along the Kayak zone (Schwab *et al.,* 1980; Bruns, 1983). The accompanying shortening by active folding and thrusting in the Pamplona zone is minor (Bruns, 1983). The Transition fault forms the southern edge of the Yakutat block and marks the edge of the continental shelf. Perez and Jacob (1980) propose that thrusting of the Pacific plate under the Yakutat block along this boundary at 1 cm/yr is decoupling the two pieces. However, geologic evidence suggests that this boundary has been inactive or weakly active during Pliocene and Quaternary time (Plafker *et al.,* 1978, Von Huene *et al.,* 1979; Bruns, 1979, 1983).

The boundary between the Pacific and the North American plates marks one of the world's most active earthquake belts. Most of this boundary has broken in major earthquakes this century. Along the eastern side of the Gulf of Alaska, the 1958 Fairweather earthquake (8.2 M_w) (Kanamori, 1977) broke the length of the Fairweather fault from Palma to Yakutat Bay (Tocher, 1960; Sykes, 1971; Plafker *et al.,* 1978). The 1979 St. Elias earthquake (7.2 M_s, 7.5 M_w) (Buland and Taggart, 1981) ruptured an adjacent region to the north from Yakutat Bay to Icy Bay. West of this zone, the boundary from Kodiak to Kayak Island (Plafker, 1969) broke in 1964 in one of the largest instrumentally recorded earthquakes (8.4 M_s, 9.2 M_w) (Kanamori, 1977). The region between the 1979 and 1964 earthquake zones has been identified as a seismic gap (Lahr and Plafker, 1980; McCann *et al.,* 1980; Sykes *et al.,* 1981). (See Figure 5.1.)

The Yakataga seismic gap lies approximately between Icy Bay and Kayak Island. Major earthquake activity shook the region near and within the gap in 1899. The

two largest shocks (4 September 1899, 8.5 M_s; 10 September 1899, 8.4 M_s) occurred within days of each other. Instrumental records poorly control the epicenters to lie in the Icy Bay and Yakutat Bay regions, respectively (Gutenberg and Richter, 1954). Evidence from eyewitnesses, recent uplift of shorelines and surface faulting suggest that both events combined ruptured the segment between Yakutat Bay and Kayak Island (Tarr and Martin, 1912; McCann *et al.*, 1980). Rupture from the 4 September 1899 event probably extends from Kayak Island to Icy Bay, while rupture from the 10 September 1899 event was probably concentrated around the vicinity of Yakutat Bay.

The only significant offshore activity prior to 1987 in the northern Gulf of Alaska took place along the Pamplona zone in the western portion of the Yakutat block where a sequence of large thrust earthquakes occurred in 1970 (Figure 5.1). Recent activity in 1987-88 activated a 3200 km^2 area in what was previously considered non-seismic oceanic crust just south of the Yakataga seismic gap (Figure 5.3). Network coverage for this region is not good. Aftershocks shown in the following figures have been relocated by Lahr *et al.* (1988) with depths fixed at 10 km. The events have maximum relative location errors of 20 km with the east-west direction better constrained than the north-south direction. The first motion solutions are from J. Lahr (personal communication) and include readings from local and global networks. Inversion results are also briefly summarized below.

Event 1, the first event of the sequence on 17 November 1987: 08h 46m 51s, 58.80°N, 143.11°W, 6.9 M_s (Lahr *et al.*, 1988), ruptured an east-west trending zone 40 km in length (Figure 5.4). Moment release was confined to a small region near

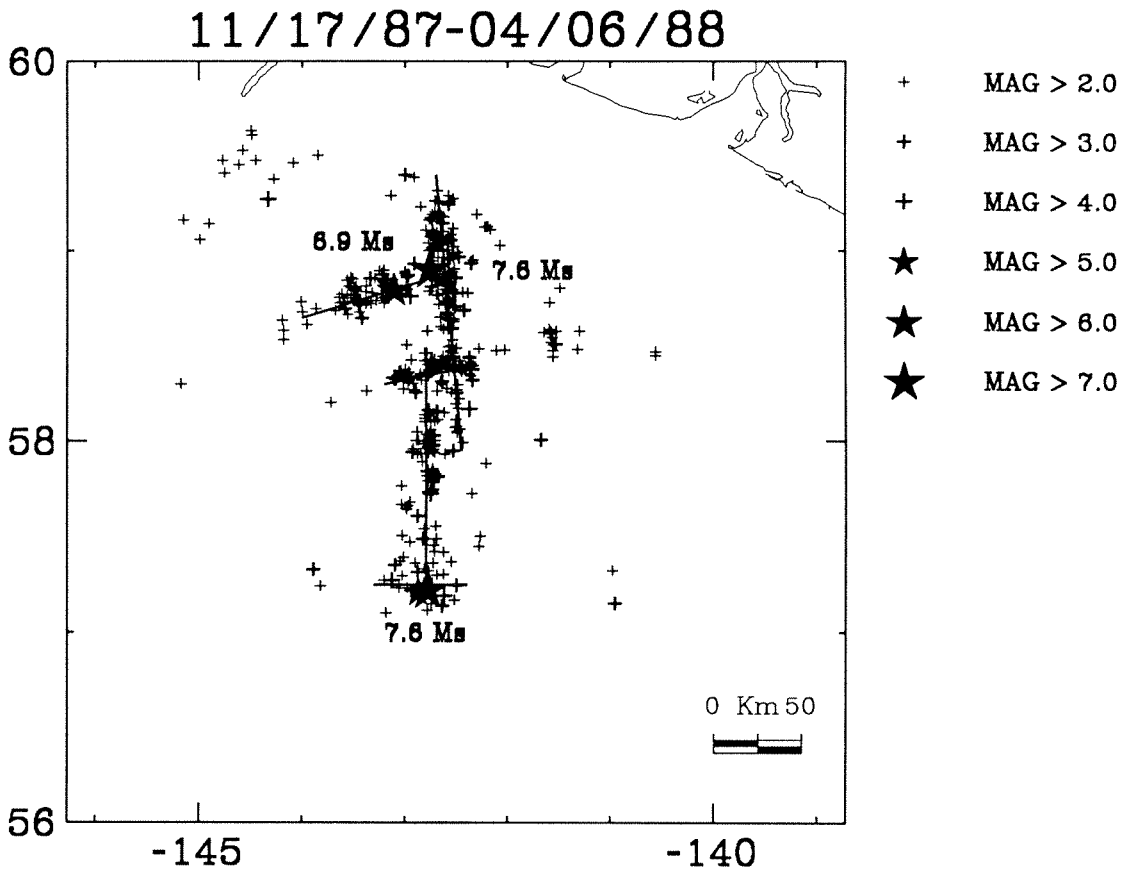

Figure 5.3: Earthquake activity in the northern Gulf of Alaska from 17 November 1987 through 06 April 1988. Events have been relocated by Lahr *et al.* (1988). Faults as inferred from seismicity are shown with a solid line. Symbols are as given in the figure. All magnitudes are M_L unless otherwise noted.

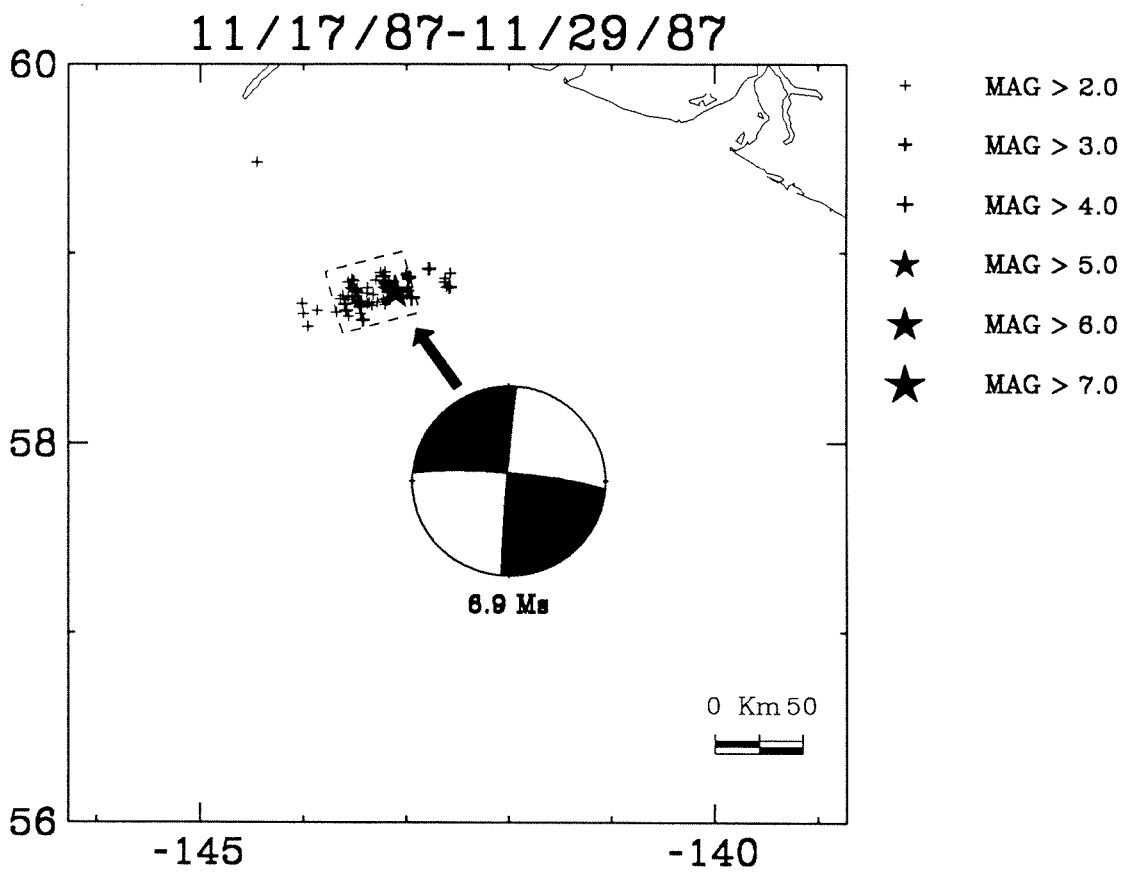

Figure 5.4: Plotted are the mainshock of the 17 November 1987 earthquake and its aftershocks from 17 to 30 November 1987. Outlined is the aftershock zone during the first 24 hrs. Symbols are as given in the figure. All magnitudes are M_L unless otherwise noted.

the epicenter. Aftershock data along with first motion data and body-wave modeling results indicate left-lateral movement within the Pacific plate.

Event 2, the second event of the sequence on 30 November 1987: 19h 23m 16s, 58.91°N, 142.76°W, 7.6 M_s (Lahr *et al.,* 1988), ruptured a primarily north-south trending zone 140 km in length (Figure 5.5). This event was preceded by a 4.5 m_b shock located 30 km ENE of Event 1. Rupture for Event 2 initially nucleated at

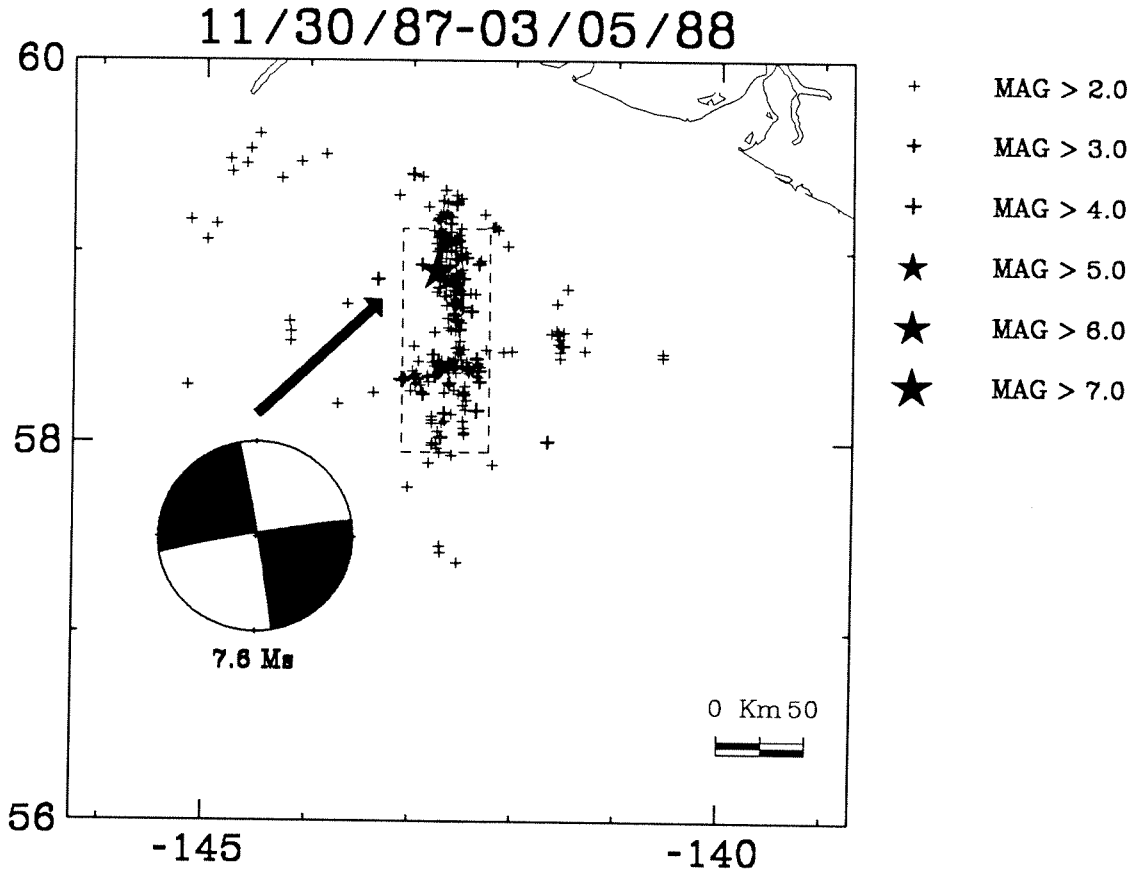

Figure 5.5: Plotted are the mainshock of the 30 November 1987 earthquake and its aftershocks from 30 November 1987 to 05 March 1988. Outlined is the aftershock zone during the first 24 hrs. Symbols are as given in the figure. All magnitudes are M_L unless otherwise noted.

the eastern edge of the aftershock zone from Event 1. Aftershocks within the first 24 hrs suggested bilateral rupture 40 km to the north and 100 km to the south of the epicenter. Seismicity was concentrated from the epicentral region towards the north and along a roughly east-west trending zone 60 km to the south (see Figure 5.3). These regions of high seismicity roughly correspond to regions of high moment release. Farther south, activity was more diffuse. In combination with seismicity associated with Event 3, their pattern suggests two parallel north-south trending fault zones. At the northernmost end, very little or no activity crossed over into the Yakutat block.

Event 3, the third event of the sequence, occurred 3 months later on 6 March 1988: 22h 35m 36s, 57.23°N, 142.78°W, 7.6 Ms (Lahr *et al.,* 1988), and predominantly ruptured unilaterally 110 km to the north on a zone offset from the initial trend of activity from Event 2 but continuous with the seismicity between Events 2 and 3 (Figure 5.3 and 5.6). Many aftershocks clustered tightly around the region of the largest aftershock (m_b = 6.2), about 70 km to the north. Aftershocks just north of the mainshock formed a cluster 50 km wide in the east-west direction. Models of moment release for this event do not indicate a large lateral extent of rupture; instead, moment release is confined to the epicentral region.

5.3 Data

The data used in the inversions are Global Digital Seismic Network (GDSN), GEOSCOPE, and Worldwide Standard Seismograph Network (WWSSN) P and SH waveforms. The distance ranges are restricted to the region $30° \leq \Delta \leq 90°$ for P waves

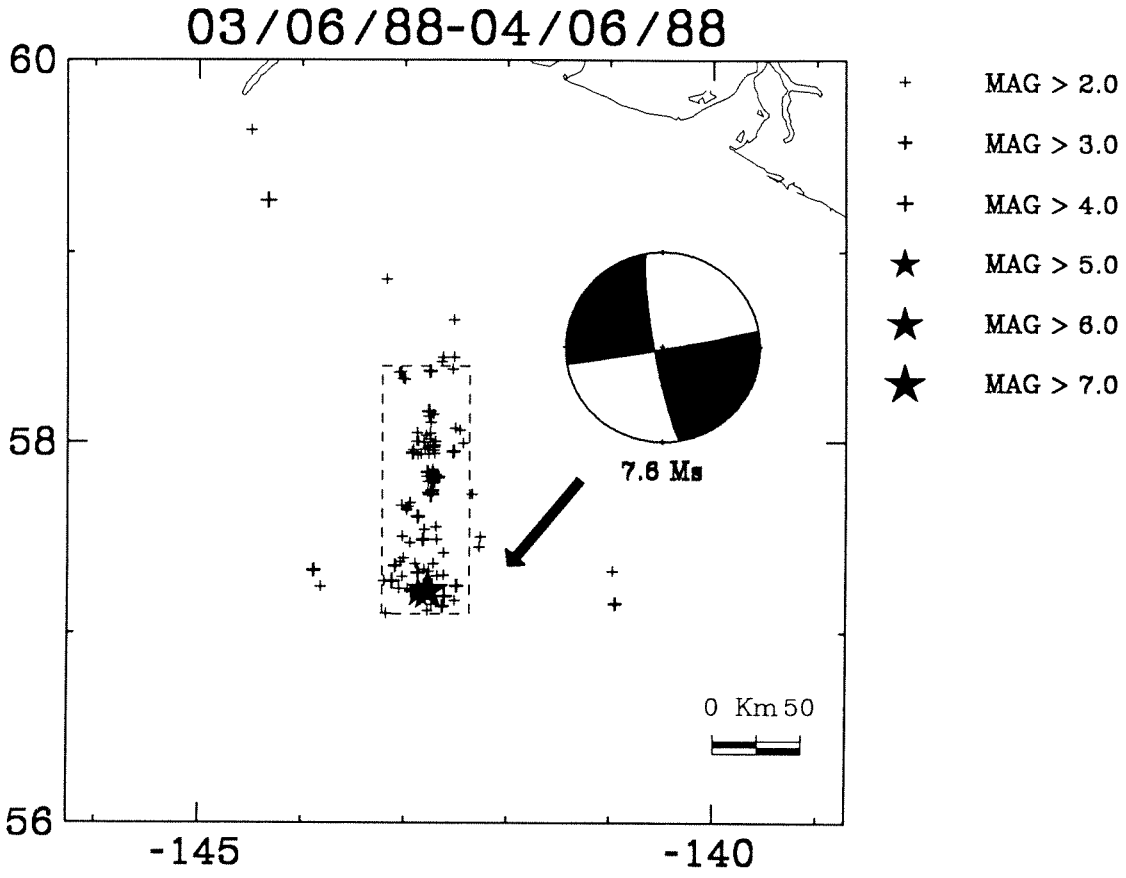

Figure 5.6: Plotted are the mainshock of the 06 March 1988 earthquake and its aftershocks from 06 March to 05 April 1988. Outlined is the aftershock zone during the first 24 hrs. Symbols are as given in the figure. All magnitudes are M_L unless otherwise noted.

and $30° \leq \Delta \leq 85°$ for SH waves to avoid regional and core effects. WWSSN data are digitized, using an optical scanner, resampled at an interval of 0.25 sec, and corrected for drift and curvature for known pen arm lengths.

Since the data from each network have different instrument responses, records are reconvolved to a standard response. Two data sets with different responses and overlapping bandwidths are modeled, a long-period GDSN and a long-period WWSSN-type data set. This allows us to test their stability and resolution. For the long-period GDSN data set, the data have either standard, long-period, network instrument responses or are modified to a standard, long-period DWWSSN-type (SCP) response. Data from the CDSN, SRO, ASRO, and DWWSSN stations retain their original instrument responses. GEOSCOPE and some DWWSSN stations have much broader-band instrument responses so their data are reconvolved to a long-period SCP instrument response and bandpass filtered between 0.01–0.3 hz. On the other hand, the long-period CDSN instrument response has a very narrow bandwidth. In general, the waveforms for the CDSN stations do not appear as complex as those for the rest of the stations and can be easily modeled. While the CDSN long-period data do little to help resolve the source-time history of the event, the data do provide constraints on the long-period focal mechanism.

The WWSSN-type data set has a broader bandwidth than the long-period GDSN data. For this data set, a combination of broadband, long, intermediate, and short period digital data is reconvolved to a standard WWSSN long-period response and bandpass filtered between 0.01–1 hz or are high-pass filtered with a low-frequency cutoff of 0.01 hz.

Thickness (km)	Depth (km)	V_p (km/sec)	V_s (km/sec)	Density (g/cm^3)
3.5*	0.0	1.5	0.0	1.0
2.5	3.5	2.4	1.4	2.1
6.0	6.0	6.5	3.8	2.9
	12.0	8.1	4.7	3.4

* 3.5 km 11/17/87; 3.2 km 11/30/87; 3.8 km 03/06/88

Table 5.1: Velocity Model.

The GEOSCOPE data used here were not corrected for clock errors. Stations that required large time corrections in the modeling procedure are noted in tables later. In the following models, the records are initially aligned on the first arrival for the P waves or the onset of the SH arrival as determined from broadband or short-period records when available. Otherwise, the theoretical arrival times are used.

The lateral fault dimensions and the range of possible models to investigate are constrained by the aftershock patterns described above. The crustal model is taken after von Huene *et al.* (1979) (Table 5.1). The total thickness of the oceanic crust is 8.5 km. The thickness of the water layer and hence, the depth to the top of the crust, varies for each earthquake as noted.

5.4 Methods

Two different methods are used to investigate the source characteristics of the Gulf of Alaska earthquakes. Both the long-period GDSN (LP) and broader band WWSSN-type (WWS) data sets are inverted using the method of Nábělek (1984, 1985) and Kikuchi and Kanamori (1990), hereafter referred to as method N and K, respectively.

In method N, teleseismic body waves are simultaneously inverted in a least-squares sense. This method can invert for multiple sources and solves simultaneously for the focal mechanism, centroid depth, and source-time function for each source. Both point and line sources can be investigated where line sources are restricted to rupture at a fixed velocity and a single depth.

In the following inversions, the LP data are initially used to estimate the gross source parameters, and the WWS data are then used to refine the model. Either the first motion or the centroid moment tensor (CMT) solution is used as a starting focal mechanism that is allowed to vary. For events with multiple subevents, subevent 1 is always constrained to start at the first motion time. The delay times of additional subevents are allowed to vary. Depths between 5 to 40 km and velocities up to 3.5 km/sec are systematically investigated by holding both parameters fixed in the inversion. The least-error solution for the different combinations of velocity and depth gives the final model.

In method K, the source-time function is built from a series of point sources that lie on a two-dimensional fault plane. The moment tensor for each individual point source can be inverted for or held fixed. The speed of the rupture front cannot exceed the specified maximum rupture velocity. Subevents can occur anywhere on or inside the rupture front. As used here, the moment tensor is constrained to be a double-couple source that is allowed to vary in time. Maximum rupture velocity is 3.5 km/sec, and the fault modeled extends from 10 to 50 km in depth. The best-fit focal mechanisms and their correlation functions are examined on the $\tau - l$ plane, where τ and l are time lag and distance of the subevents from the epicenter, to

determine the complexity of the event and the resolution of the focal mechanism, timing, and subevent positions. The first and largest subevent solved for in the inversion corresponds to a peak in the correlation function and is the most robust. As the waveform from each subevent is subtracted from the original data, each successive subevent tends to have less moment, is less reliable, and depends on the source parameters of the previous subevents. Hence, the first several iterations give the most robust solutions.

The final model results for the three earthquakes investigated here are summarized in tables in the next section. The first motion (J. Lahr, personal communication) and the CMT solution (Dziewonski *et al.*, 1989a; Dziewonski *et al.*, 1989b) are also shown for comparison. The last column gives the moment for the subevent(s) as described. Total moment, if different, is given in parentheses. For solutions with a time-varying source in method K, the focal mechanisms and the total moment given represent the best double-couple sum of the subevents comprising the event.

5.5 Inversion Results

5.5.1 17 November 1987

Tables 5.2 and 5.3 summarize the data modeled. This is a relatively simple event with an emergent first arrival most noticeable at the northern stations. For method N, the LP data are initially used to investigate various single and multiple source models. Neither single-line or point source models could explain both the initial and the main arrival. Different combinations of line and point sources indicate that the best parameterization consists of a point source at the epicenter and a line source

Station	Azimuth (deg)	Distance (deg)	Bandpass (Hz)	Type	Weight
KEV	4	52	0.01-0.3	P,SH	1.00,0.40
KONO	16	60		P,SH	1.00,0.40
GDH	36	37		P	1.00
WFM	78	46	0.01-0.3	P,SH	1.00,0.40
SCP*	84	44		P	0.70
CAY	87	86	0.01-0.3	P	0.70
HDC	112	66	0.01-0.3	P	1.00
PPT	186	76	0.01-0.3	SH	0.40
HON	202	39		P	1.00
KIP	202	39	0.01-0.3	SH	0.40
MAJO	282	54		P,SH	0.70,0.40
TATO	288	72		P	0.70
BJI	301	62		P,SH	0.70,0.35
HIA	306	53		P,SH	0.70,0.35

* timing problems

Table 5.2: 17 November 1987. Stations for LP models.

propagating towards the west. Triangular source elements with duration and rise times of $\tau_r = \tau_d = 2$ sec are used to model the LP data, while shorter source elements, $\tau_r = \tau_d = 1$, are used to match the higher-frequency content seen in the broader band data.

The inversion of the LP and WWS data with the above parameterization is used to determine the rupture velocity and centroid depth of this event. Figure 5.7a shows the misfits between the observed and calculated seismograms for a centroid depth of 25 km (justified later) as a function of rupture velocity. For the LP data (dashed line), the errors are roughly independent of velocity for velocities less than 2.5 km/sec and increase slightly for higher velocities. Over the depth range investigated, errors

Station	Azimuth (deg)	Distance (deg)	Bandpass (Hz)	Type	Weight
NUR	7	61		P	1.00
DAG	17	40		P	0.07
STU	19	70		P,SH	0.70,0.50
VAL	31	63		P,SH	0.70,0.35
PTO	34	74		SH	0.45
GDH	36	37	0.01	P	0.80
WFM	78	46	0.01-1	P,SH	0.70,0.50
CAY	87	86	0.01-1	P	0.70
LUB*	114	37		P	0.70
PPT	186	76	0.01-1	SH	0.50
HON	202	39	0.01	P	1.00
KIP	202	39	0.01-1	SH	0.50
HNR	237	82		P	1.00
GUA	262	69		P,SH	1.00,0.50
INU*	282	56	0.01-1	P,SH	0.70,0.50
ANP	288	72		P	0.70
HKC	292	78		SH	0.50
BJI	301	62	0.01	P	0.70
HIA	306	53	0.01	P	0.70

* timing problems

Table 5.3: 17 November 1987. Stations for WWS models.

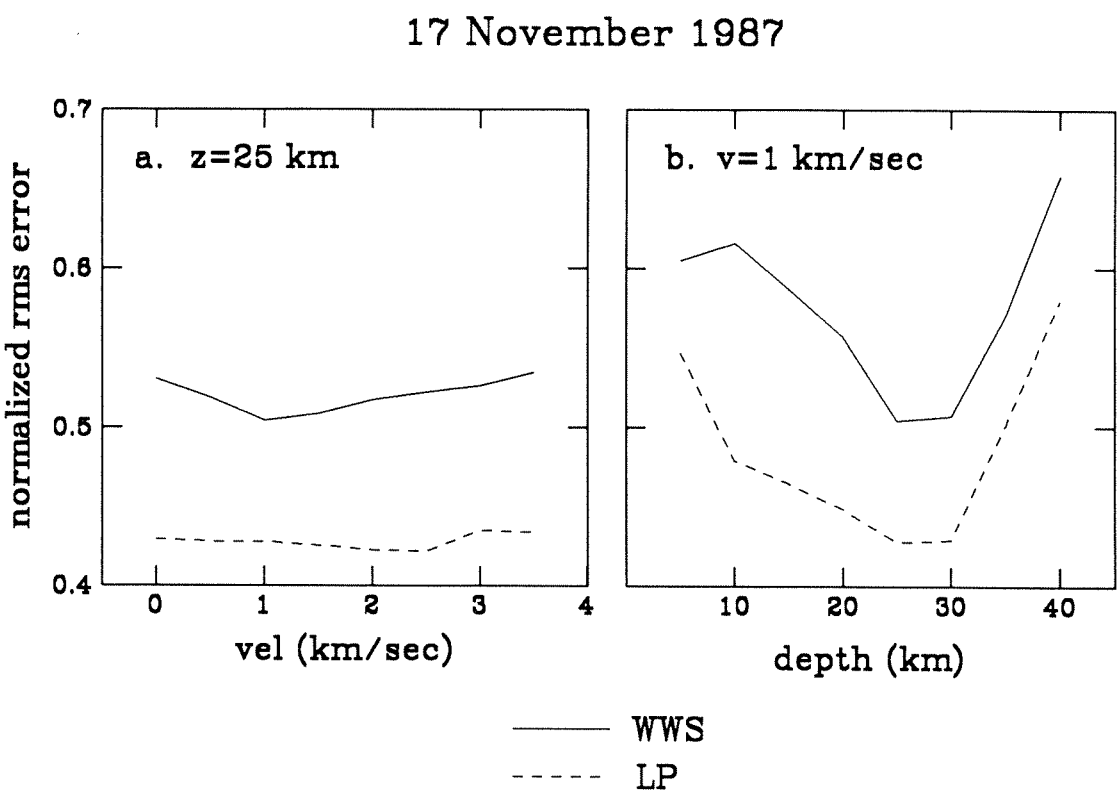

Figure 5.7: Data misfits for the LP (dashed line) and WWS (solid line) data for method N. Plotted are the normalized rms errors versus: a. velocity for a fixed centroid depth of 25 km, and b. centroid depth for a fixed velocity of 1 km/sec.

change little with velocity at any given depth. The WWS data (solid line), however, yield a minimum rupture velocity at 1.0 km/sec. Figure 5.7b shows the misfits between the observed and calculated seismograms as a function of centroid depth for a constant rupture velocity of 1.0 km/sec. For all velocities examined, the errors for both data sets indicate that the best solution lies between 25–30 km with, the lowest errors at 25 km. Final models have a rupture velocity of 1.0 km/sec and a centroid depth of 25 km.

Figures 5.8 and 5.9 show the resulting focal mechanism for the main subevent,

Model	Strike (deg)	Dip (deg)	Rake (deg)	Depth (km)	Delay (sec)	Velocity (km/sec)	Dist (km)	Azi (deg)	Moment (dyne-cm)$\times 10^{26}$
FM	275	83	2	10*					
CMT	262	57	-6	15*					6.6
1NLP	265	74	2	25	4	1.0			5.3 (6.4)
1NWWS	266	75	-2	25	2.3	1.0			6.7 (8.0)
1KLP	260	84	-8	20	4	3.5#	10-20	80	9.6
							40	260	1.0 (8.4)
1KWWS	275	78	0	20	4.0	3.5#	0-40	270	8.4 (6.3)

* fixed
# maximum rupture velocity
Abbreviations: FM: first motion solution (J. Lahr, personal communication).
CMT: Centroid Moment Tensor (Dziewonski *et al.*, 1989a, 1989b).
For others, see text.

Table 5.4: 17 November 1987. Model parameters.

the data and synthetics, and the source-time function for the LP solution — model 1NLP. Model 1NLP fits the observed, long-period waveforms well. The first subevent (not shown), 1NLP.1, is primarily a normal faulting event (strike 184°, dip 44°, rake -73°). However, it is poorly resolved. Over the complete depth and velocity range investigated, the estimates of its strike vary by up to 80°. The low moment (1.3×10^{26} dyne-cm) of 1NLP.1, combined with the interference from the second subevent, contributes to the poor resolution. On the basis of aftershock seismicity, the second subevent, 1NLP.2, has a left-lateral strike-slip mechanism on an east-west trend. Estimates of the strike fall within ±5° of the final solution. For a depth of 25 km, the estimates of dip and rake vary by ±2°. Hence, the focal mechanism of the second subevent is well resolved at strike 265°, dip 74°, and rake 2°. 1NLP.2 has roughly five times more moment than 1NLP.1. Combined, the total moment is 6.4×10^{26} dyne-cm. Source parameters for 1NLP.2 are given in Table 5.4.

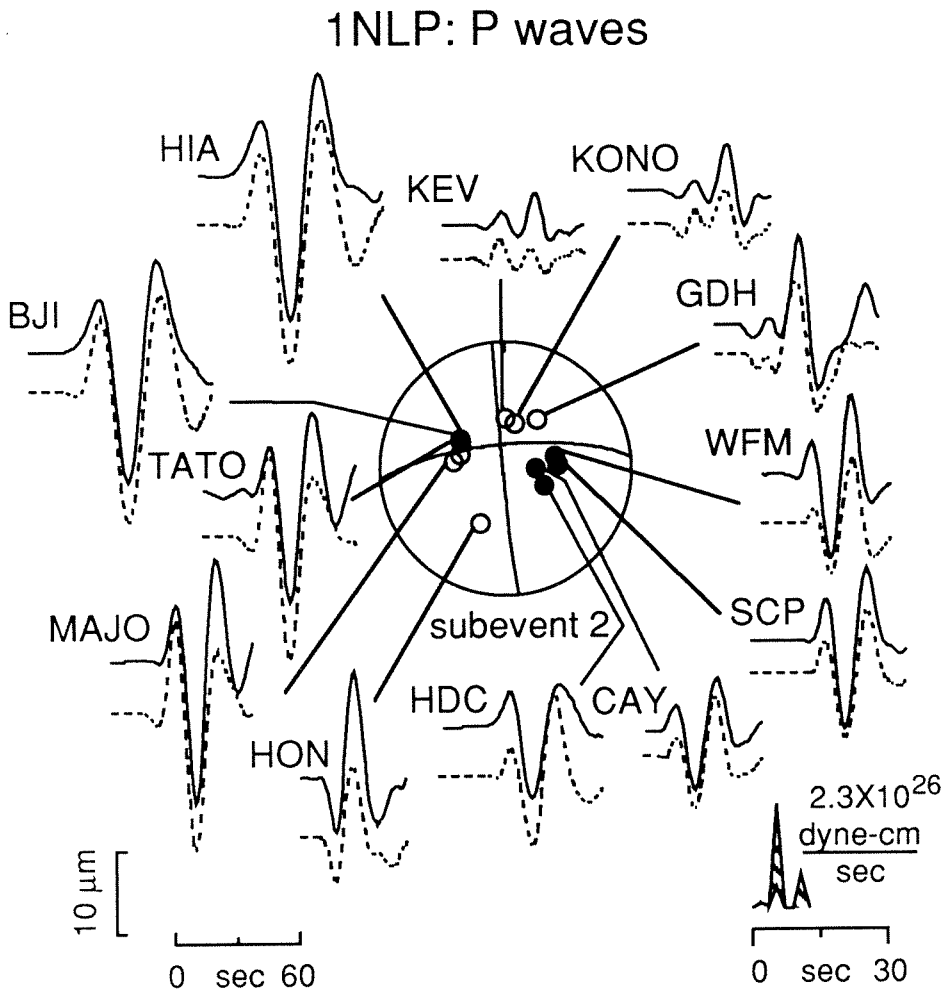

Figure 5.8: 1NLP. Observed (solid line) and synthetic (dashed lines) LP P-wave seismograms. Shown in the center of the figure is the lower hemisphere focal mechanism for the largest subevent. Solid circles represent compressional, and open circles, dilatational first motions. Source parameters are given in Table 5.4. The combined source time function is shown at bottom right. The unhatched regions represent the percentage of moment contributed by 1NLP.1 and hatched regions by 1NLP.2. Time and amplitude scales are shown at bottom left. Amplitudes of the observed and synthetic seismograms are normalized to the identical instrument at a distance of 60° with a peak magnification of 1.

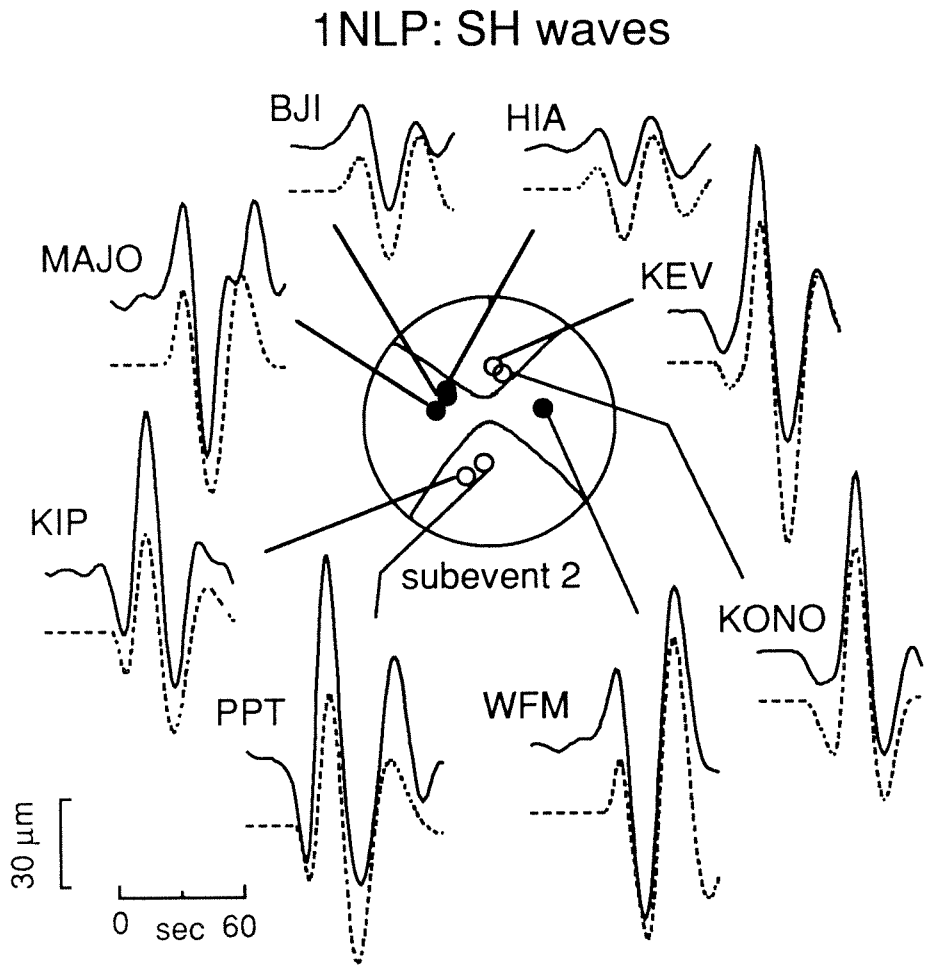

Figure 5.9: 1NLP. Observed (solid line) and synthetic (dashed lines) LP SH-wave seismograms. Symbols are described in Figure 5.8.

Figures 5.10 and 5.11 show the results for the WWS data, model 1NWWS. The synthetics for model 1NWWS overall fit the observed waveforms well but do not model all of the detail seen in the high frequency energy. The focal mechanism of the first subevent in the final model, a NNW-SSE striking, normal faulting event (strike 160°, dip 40°, rake -62°), is again not well resolved. The mechanism for the second subevent is almost identical to that in model 1NLP. Its focal parameters are: strike 266°, dip 75°, rake $-2°$. The resolution of the focal parameters for 1NWWS is the same as for 1NLP. Total moment is 8.0×10^{26} dyne-cm. Source parameters for 1NWWS.2 are given in Table 5.4.

Model 1NWWS is consistent with 1NLP. Both the source-time functions and focal parameters are similar. Model 1NWWS can also be used to explain the long-period waveforms. Total source duration is approximately 12–18 sec. A duration time of about 14 sec for 1NWWS.2 suggests only 14 km of the fault ruptured towards the west. This is considerably smaller than the aftershock dimensions.

The LP and WWS data are also modeled using method K to investigate possible time variations in the focal parameters. The fault plane spans a distance of 50 km to the west and 20 km to the east of the epicenter. Inversions using the LP data constrain the best-fitting, single-source element to have a duration time of approximately 16 sec, where $\tau_r = 2$ sec and $\tau_d = 14$ sec (Figure 5.12). This source lies at a depth of 10 km and has a delay time of 4 sec. Its focal mechanism is in good agreement with the above results. While this solution fits most of the waveforms well, it does a poor job of fitting the initial arrival at the northern stations (Figure 5.13b). A second and third iteration add two smaller subevents at 10 and 7 sec with a

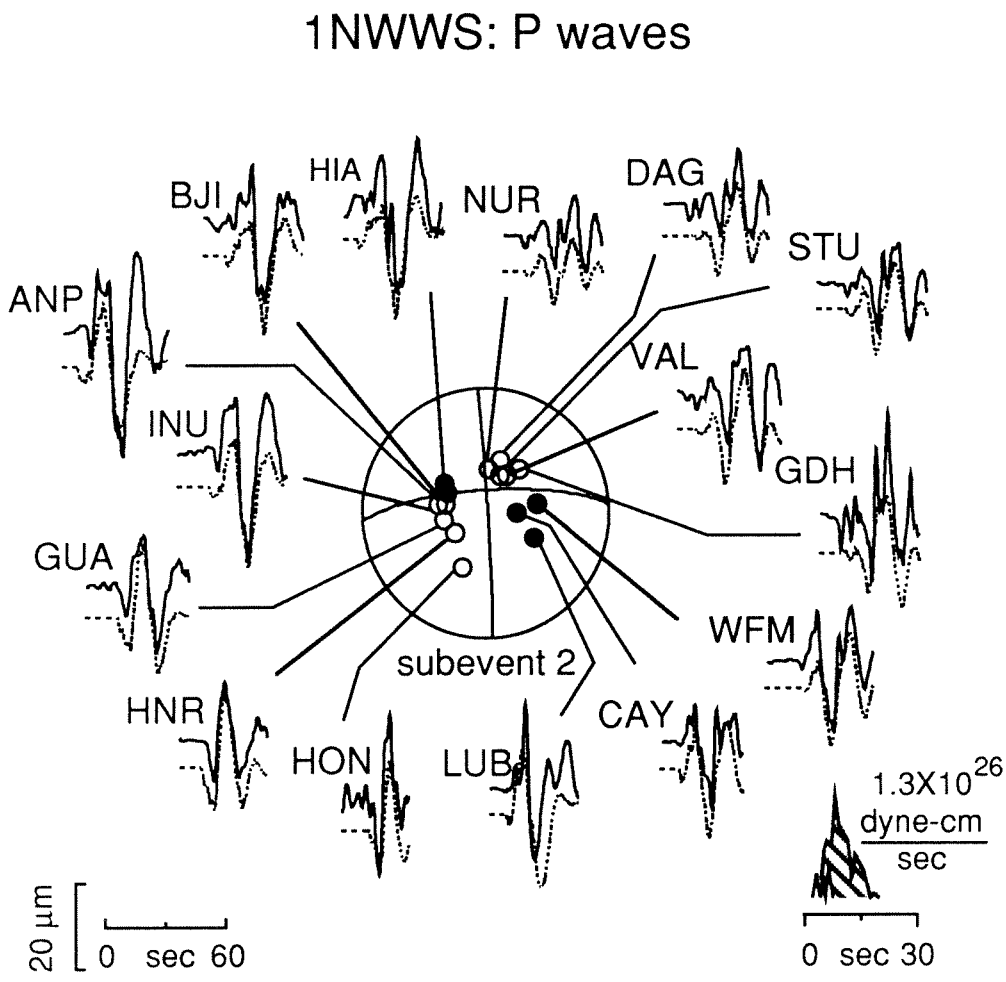

Figure 5.10: 1NWWS. Observed (solid line) and synthetic (dashed lines) WWS P-wave seismograms. Symbols are described in Figure 5.8.

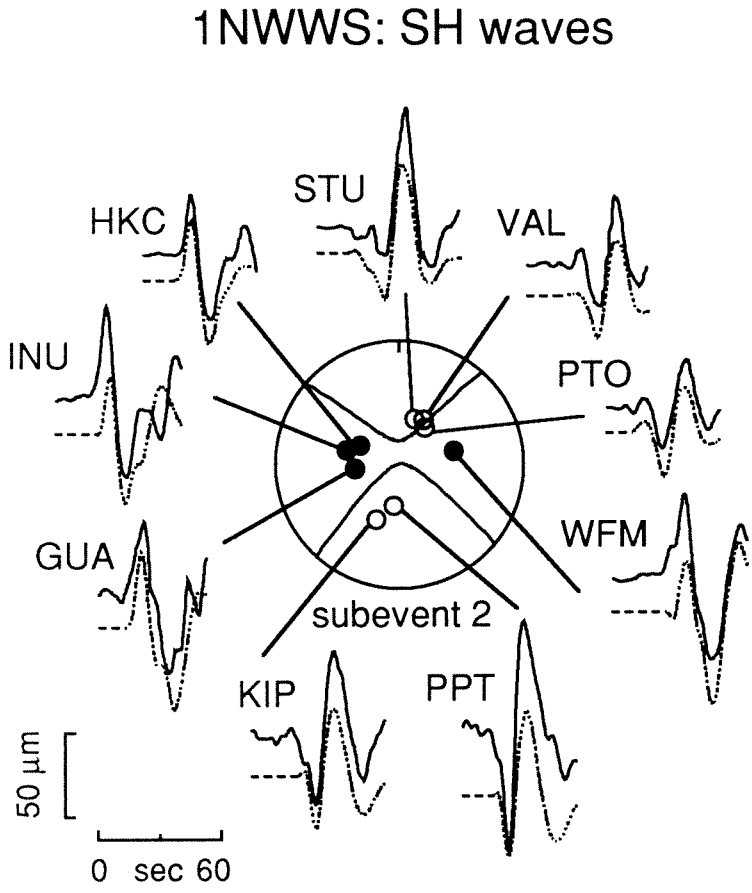

Figure 5.11: 1NWWS. Observed (solid line) and synthetic (dashed lines) WWS SH-wave seismograms. Symbols are described in Figure 5.8.

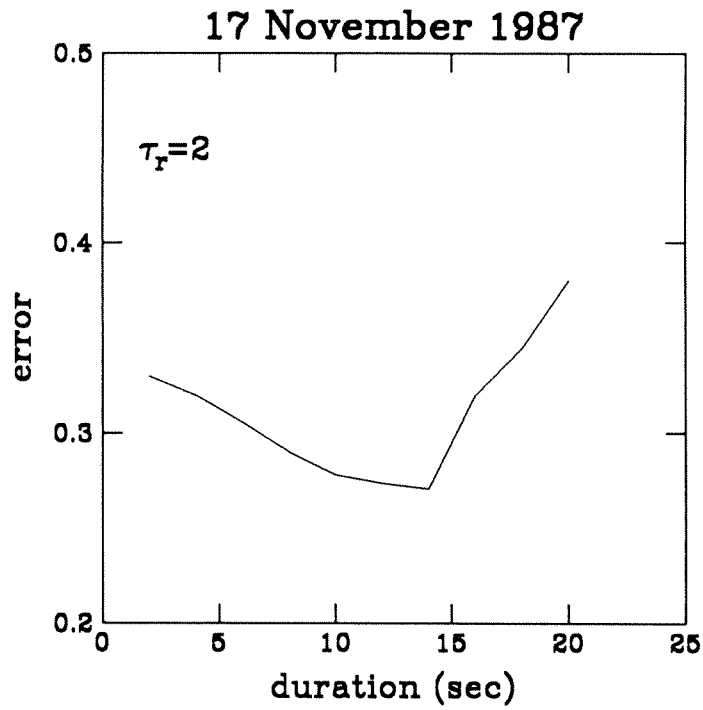

Figure 5.12: Data misfits for the LP data in method K. Plotted is the error versus τ_d of the single best fitting trapezoidal source function where $\tau_r = 2$.

high-angle reverse and thrust faulting mechanisms, respectively. These additional subevents improve the match in waveform shape (Figures 5.13c)

The above model can satisfactorily explain most of the data set. However, to model the complex waveforms to the north, three subevents with very different focal mechanisms are used. Because of the long duration of the source element and overlap in time of each subevent, the rapid change in the focal mechanisms is not too surprising, since the duration time trades off substantially with the focal as well as

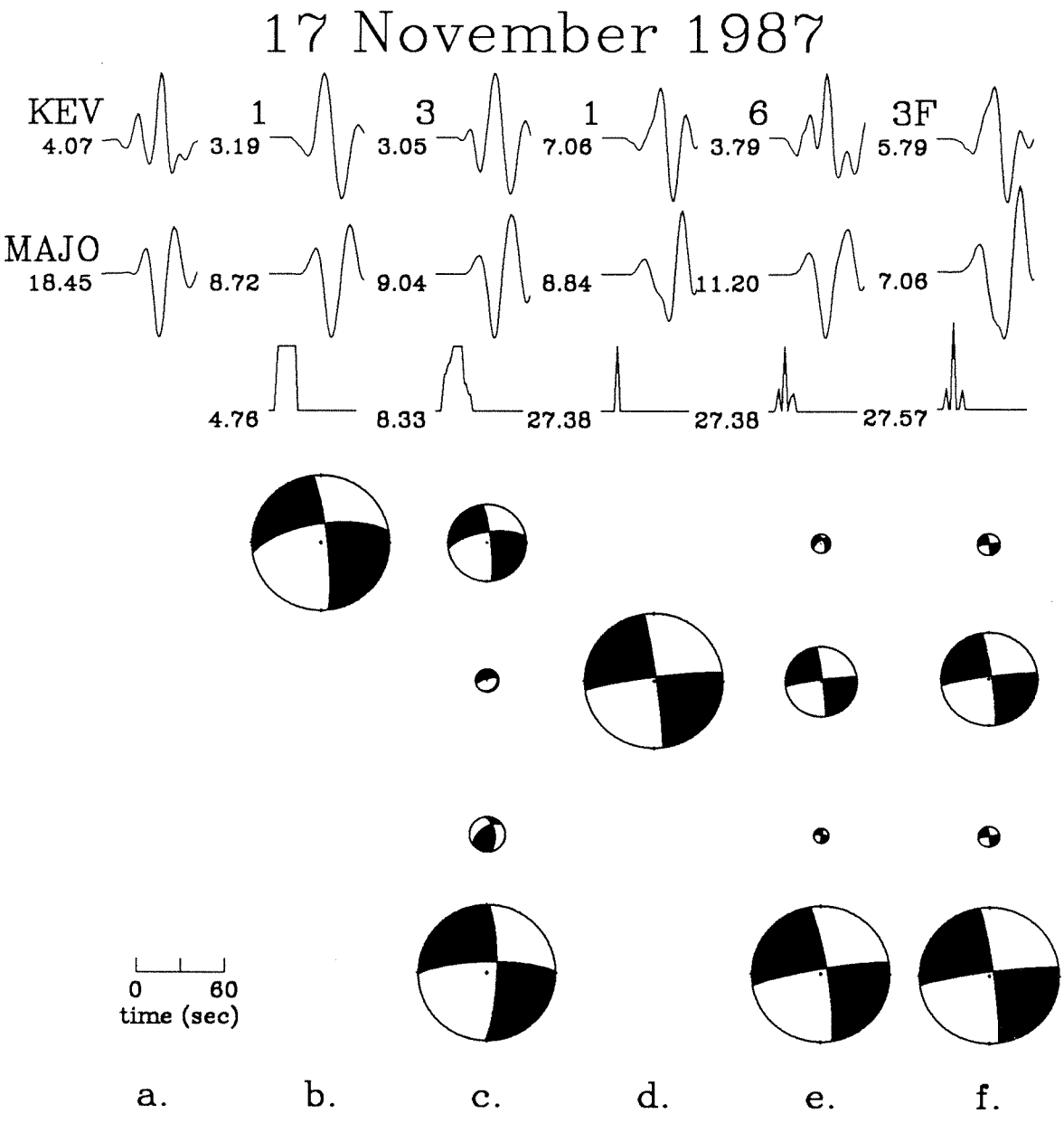

Figure 5.13: Modeling of LP data using method K. Shown are the data and synthetic P-waves for two stations (first and second row) and the source-time function of each model (third row). The above are trace-normalized to the amplitude in microns given to the left of each trace. The remaining columns show the focal mechanism(s) of the subevent(s) comprising each model. The size of each subevent reflects its contribution to the total moment and is normalized to the size of the best double-couple sum of the subevents shown in the last row. Subevents are ordered with respect to time. Shown are: a. data for stations KEV and MAJO; synthetics for models with time-varying focal mechanisms and $\tau_r = 2$ and $\tau_d = 14$ sec for b. 1 and c. 3 iterations, and $\tau_r = \tau_d = 2$ sec for d. 3 and e. 6 iterations; and f. synthetics for a fixed focal mechanism and 3 iterations.

other source parameters. However, thrust and reverse faulting mechanisms are not necessary to explain the data. By shortening the source element, this event can be modeled by predominantly strike-slip subevents.

Figure 5.13d shows the results of one iteration using a shorter source element where $\tau_r = \tau_d = 2$ sec. Figure 5.14 contours the correlation functions and the corresponding best-fit focal mechanisms. The correlation functions form one well-isolated peak, suggesting that this is a relatively simple event. This peak corresponds to the location and time of the largest subevent. The correlation deteriorates rapidly in time away from the peak, but not as rapidly in the along strike directions. The focal mechanisms along the ridge that represents the best correlated subevents are remarkably stable over the length of the fault and in the following 5 sec time period. During these 5 seconds, the focal mechanism is not very sensitive to position along the fault plane or position in time. Subevents outside this time period have focal mechanisms that are still strike-slip but have strikes that vary with position along the fault.

The correlation functions suggest that this is a simple event and that one mechanism should be able to explain most of the data. To test how well a single focal mechanism can explain the data, it is constrained in the inversion to be identical to the initial subevent for three iterations. The resulting synthetics fit the overall features observed in the waveforms at many stations. However, they fail to match the initial arrival at the northern stations and do not match the waveforms to the west (Figure 5.13f). Subsequent iterations have very little moment and do little to improve the fit. This suggests that the initial focal mechanism is different from the

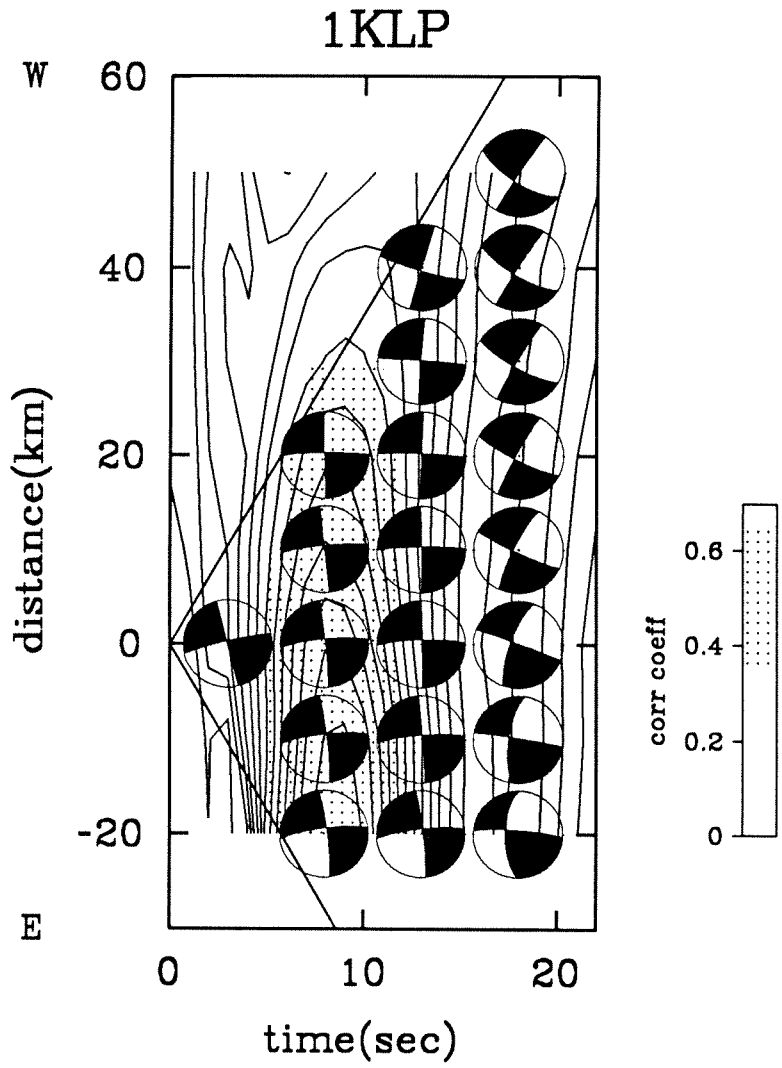

Figure 5.14: 1KLP. Correlation coefficients and corresponding best-fit double-couple focal mechanisms in the $\tau - l$ plane. Mechanisms are plotted at time intervals of 5 sec at each grid point along strike.

mechanism of the main subevent and that at least 2 subevents are needed to model this event.

The final model, 1KLP, allows the focal mechanism to vary in time for 6 iterations. Focal mechanisms of the three largest subevents along with the best double-couple sum of the 6 subevents comprising the solution are shown in Figure 5.13e. The focal mechanisms are predominantly strike-slip with considerable differences in the focal parameters among the largest subevents shown above. The next two smaller subevents, not shown, have focal mechanisms similar to the largest subevent.

Figures 5.15 and 5.16 show all of the data and synthetics for model 1KLP. The focal mechanism shown and given in Table 5.4 is the best double-couple sum of its 6 subevents. Overall matches to the waveforms are good. P-waveform shapes in the beginning of the record for KONO and GDH to the north are not as well fit as KEV, but are better fit than the initial model, which used a longer source element. Amplitude matches have also been improved. A slightly longer duration of the synthetics and the mismatch in the amplitudes at stations TATO and MAJO suggests that westerly rupture propagation could improve the fit.

In model 1KLP, the largest and best resolved subevent accounts for over 50% of the total moment. It lies at a depth of 20 km and at a distance of 20 km east of the epicenter at the edge of the modeled fault plane. Extending the fault plane farther towards the east showed that this is a stable position. Most of the subevents lie east of the epicenter between a depth of 10–20 km. One subevent does lie to the west, but it accounts for less than 10% of the total moment. Comparison with 1NLP suggests that the LP data can resolve moment release only to a lateral distance of ± 20 km of

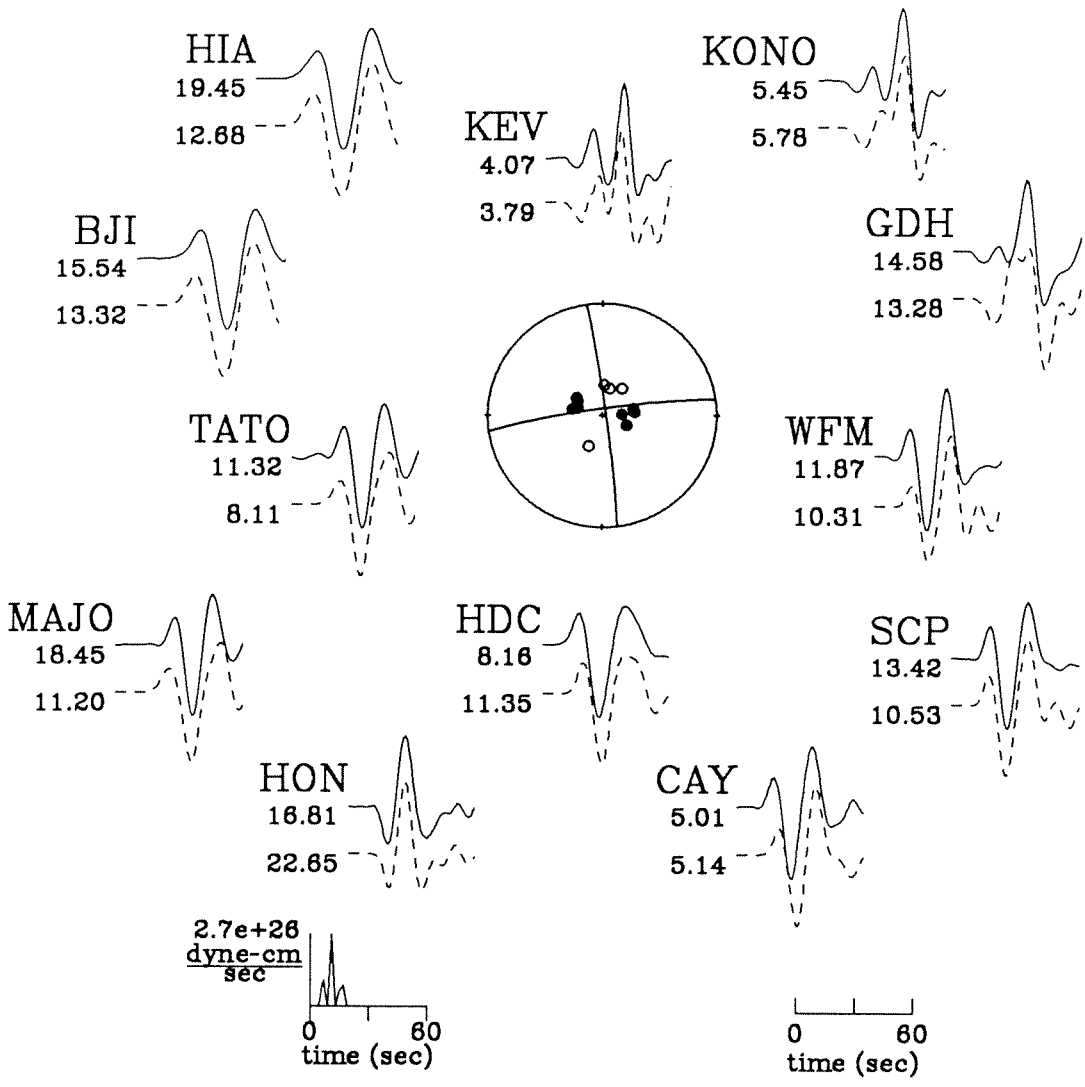

Figure 5.15: 1KLP. Observed (solid line) and synthetic (dashed lines) LP P-wave seismograms. Shown in the center of the figure is the lower hemisphere focal mechanism of the best double-couple sum of the subevents comprising the model. Solid circles represent compressional, and open circles, dilatational first motions. Source parameters are given in Table 5.4. The combined source-time function is shown at bottom left. Amplitudes of the observed and synthetic seismograms are trace-normalized to the amplitude in microns given to the left of each trace.

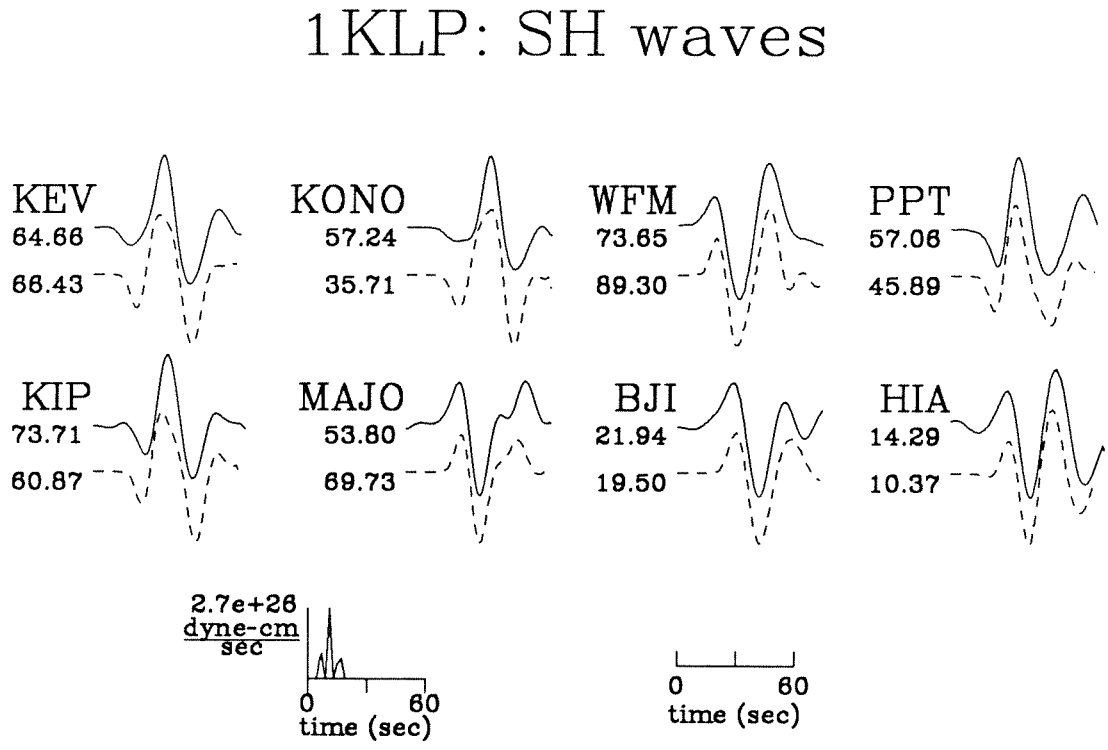

Figure 5.16: 1KLP. Observed (solid line) and synthetic (dashed lines) LP SH-wave seismograms. Symbols are described in Figure 5.15.

the epicenter. The best double-couple sum has a scalar moment of 8.4×10^{26} dyne-cm with a very small nondouble-couple component (<1%).

The WWS data are modeled using the same source and model parameterization as above. The correlation functions for the WWS data are similar to those for the LP data (Figure 5.17). For the first 10 sec, the focal mechanisms of the corresponding subevents are stable. Even though the correlation functions have one well isolated peak, as above, a single focal mechanism cannot explain the data. Again, at least two subevents with different focal mechanisms are needed to model the data. Figures 5.18 and 5.19 show the data and synthetics for the final WWS model using a time-varying focal mechanism, model 1KWWS. The focal mechanism shown and given in Table 5.4 is the best double-couple sum of the 4 subevents comprising the solution. Stations with relatively simple P-waveforms are well matched but the details in the data, especially for stations to the NNE, are difficult to model.

In model 1KWWS, the largest subevent lies 10 km to the west of the epicenter at a depth of 20 km. Its shallower dip as compared to the LP results is a robust feature (Figure 5.17). Focal mechanisms for the individual subevents are consistently left-lateral, strike-slip on an ENE-WSW trending fault plane. Their strikes differ by up to 36° from the strike of the largest subevent. Most of the subevents occur at a depth of 20 km and are distributed to the west of the epicenter. The best double-couple sum has a scalar moment of 6.3×10^{26} dyne-cm with a small nondouble-couple component (<1%).

Table 5.4 summarizes the source parameters for all the above models. Models are in good agreement with one another. This earthquake consisted of multiple

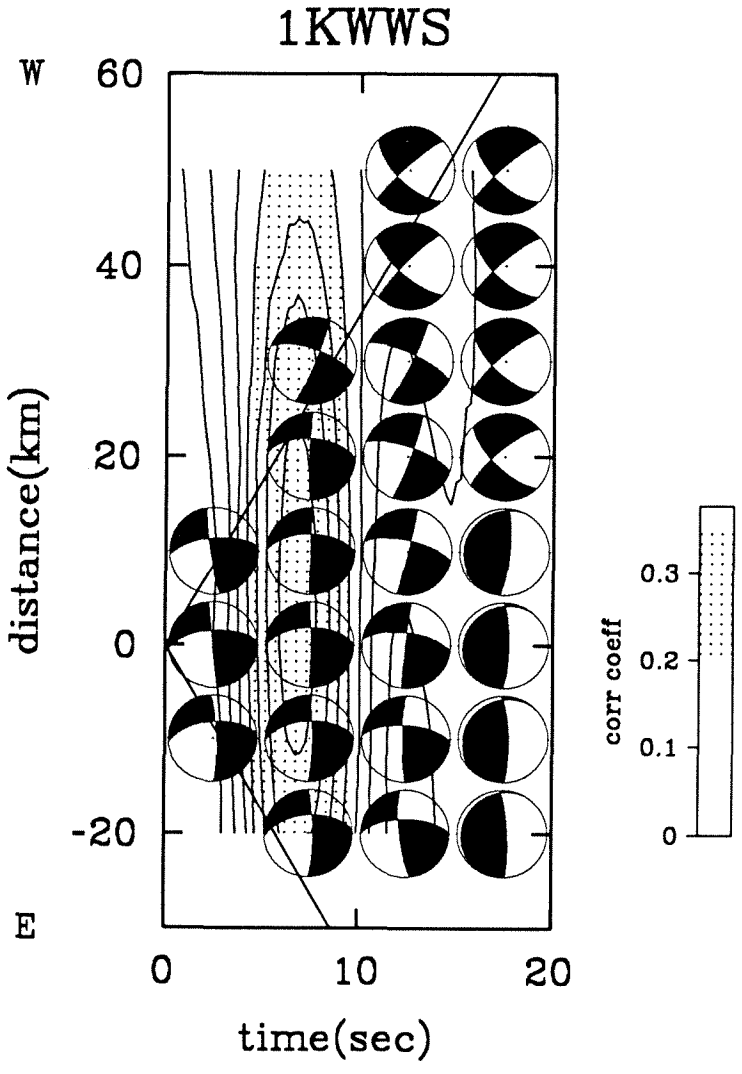

Figure 5.17: 1KWWS. Layout is described in Figure 5.14.

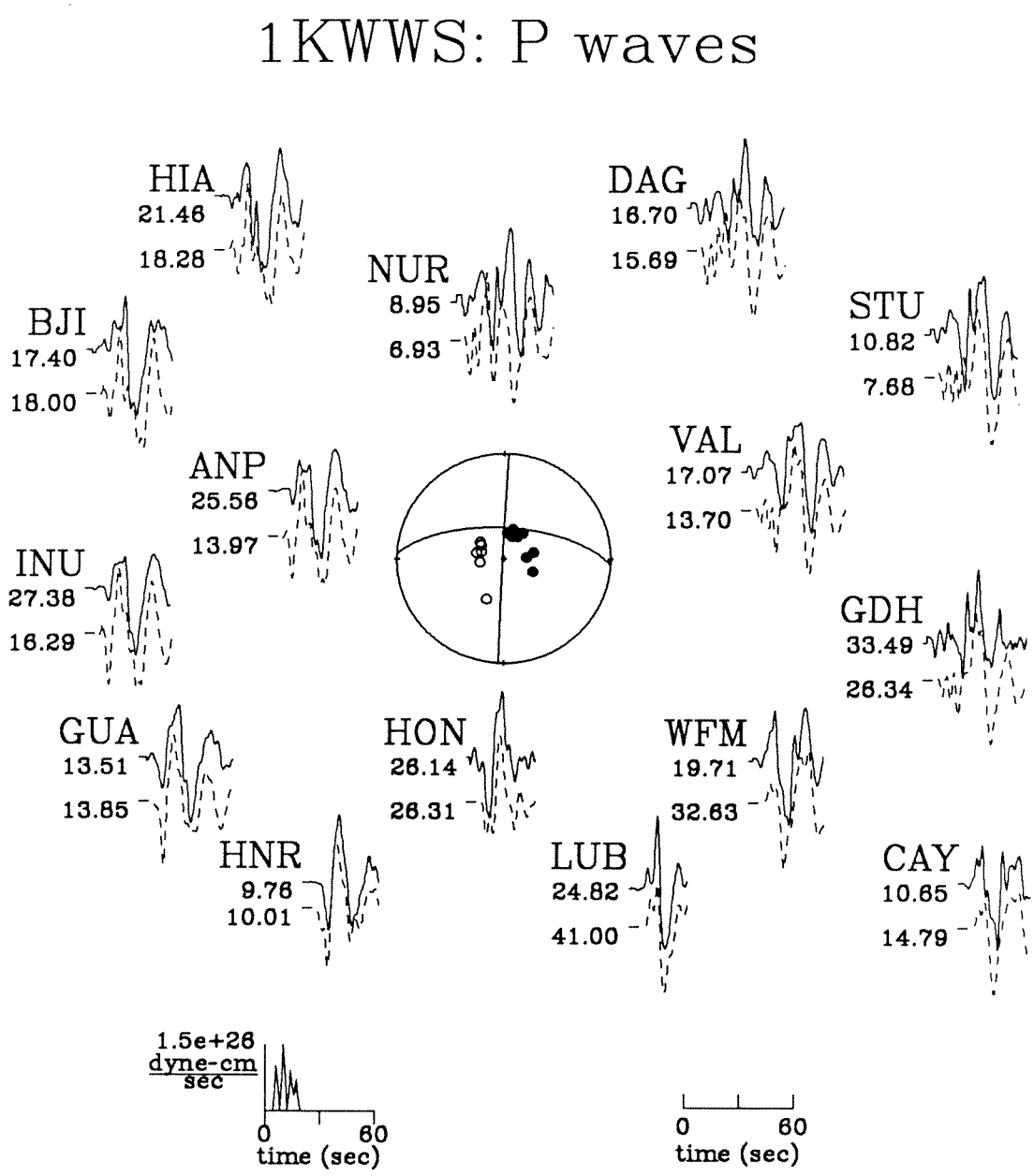

Figure 5.18: 1KWWS. Observed (solid line) and synthetic (dashed lines) WWS P-wave seismograms. Symbols are described in Figure 5.15.

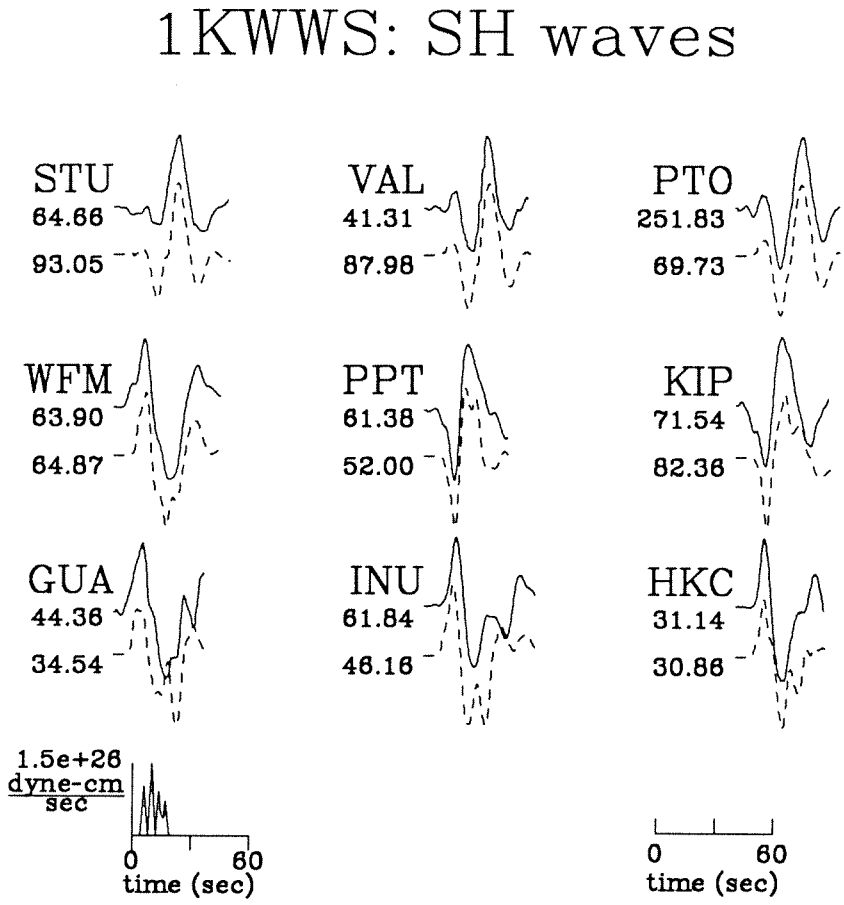

Figure 5.19: 1KWWS. Observed (solid line) and synthetic (dashed lines) WWS SH-wave seismograms. Symbols are described in Figure 5.15.

subevents. The largest subevent has a left-lateral, strike-slip mechanism on an east-west trending fault plane that dips steeply towards the north and lies at a centroid depth of 20–25 km. Most of the moment release occurs in the epicentral region within 20 km of the epicenter (Figure 5.20). Moment release begins slowly. The main sequence does not initiate until approximately 4 sec after the first arrival and has a duration of approximately 14–16 sec. Estimates of the total moment release vary and correspond to $M_w = 7.2$. This is larger than the reported surface wave magnitude ($M_s = 6.9$, NEIC).

Only the models using the WWSSN-type data set indicate any directivity of the source. In Model 1NWWS, rupture propagates towards the west at a velocity of 1.0 km/sec. This model also suggests the rupture front propagates at about the same slow rate. However, errors for 1NLP do not suggest that directivity effects are necessary to explain the data (Figure 5.7a) even though, as observed in model 1NLP and noted above for 1KLP, rupture propagation towards the west helps match waveforms at the westerly stations.

This event initiated with a small moment releasing subevent. Modeling using a single focal mechanism cannot explain the beginning of all of the waveforms. Hence, the initial mechanism is not the same as that for the largest subevent. Models 1KLP and 1KWWS allow the focal mechanism to vary but do not solve for any moment release before 4 sec. Hence, these models cannot match the timing or shape of the first arrival very well. Constraining moment release to begin earlier fits the early portion of the waveforms better at the northern station but at considerable expense to the remainder of the waveform and to the waveform matches at other stations. In

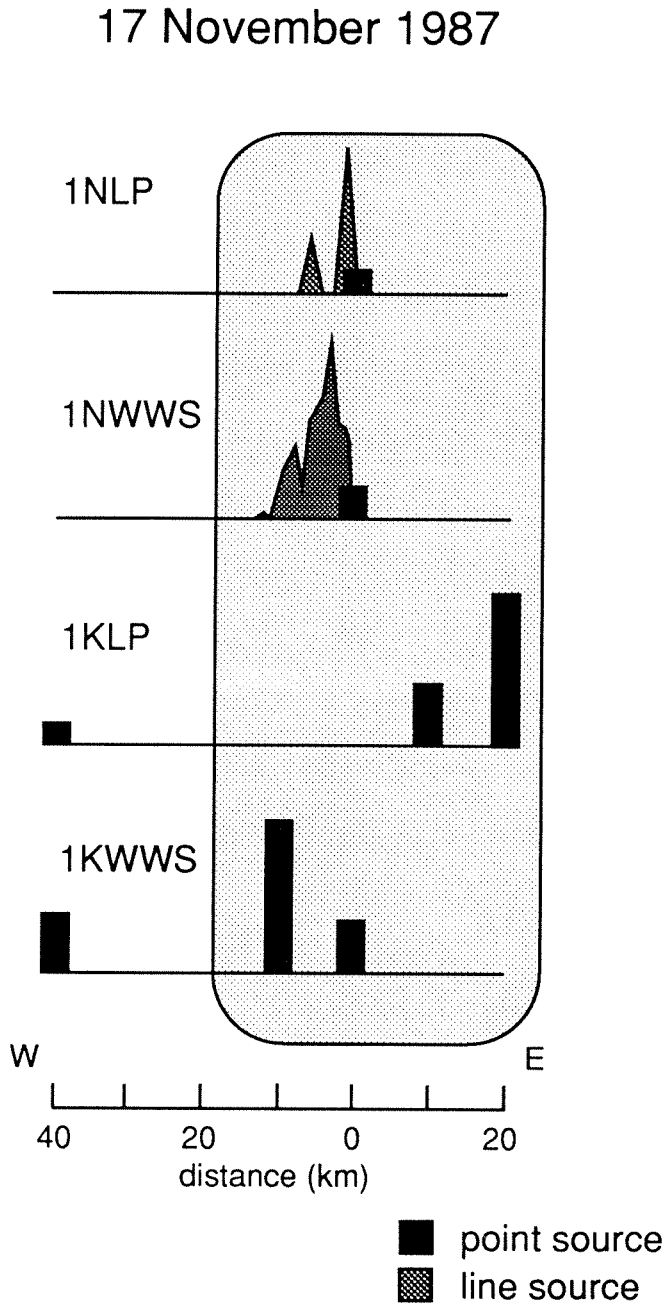

Figure 5.20: Event 1. Comparison of spatial moment distribution for each model. The height of each subevent is proportional to its moment and is normalized to the largest subevent in each model. Filled rectangles show the position of the point sources, and shaded figures represent the moment distribution of the line sources along the fault. Stippled region marks the lateral bounds of moment distribution and corresponds to the shaded region in Figure 5.52.

contrast, constraining moment release to begin at the first arrival time for the first subevent in models 1NLP and 1NWWS can explain the data. This constraint results in a roughly north-south striking, normal faulting subevent with less than 20% of the total moment.

The main moment releasing portion of the waveforms can be well modeled by a single source. Estimates of the strike of the second subevent fall within 15° of each other. For this second subevent, a strike rotated counterclockwise from due west agrees better with the overall trend of the aftershock data. However, even the most southerly striking fault plane solution still differs from the trend of the aftershock data by approximately 10°. Estimates of dip range from 57 to 84°. The shallower fault dip estimated by the CMT method is probably due to the preassigned source depth. Source depths of 15 km using method N produce comparable dips. On the basis of the above models, a more realistic dip would be approximately 75 to 85°.

5.5.2 30 November 1987

Tables 5.5 and 5.6 summarize the data modeled. Inspection of the long-period and broadband waveforms indicates that this is a complex event. As seen on the broadband records, this event begins emergently with most of the energy not arriving until 15 sec after the first arrival. In method N, the models are parameterized with multiple subevents. Different single and multiple point and line-source parameterizations investigated indicate that at least three subevents are needed to model the data. This agrees with the analysis of Deschamps *et al.* (1988). The first subevent is modeled as a point source of short duration, located at the epicenter. Both line and point sources are examined for subevents 2 and 3. As suggested by the after-

Station	Azimuth (deg)	Distance (deg)	Bandpass (Hz)	Type	Weight
KONO	16	60		P	0.70
SBB	24	73	0.01-0.3	P,SH	0.70,0.20
TOL	32	76	0.01-0.3	P,SH	0.70,0.20
WFM	78	46	0.01-0.3	P,SH	0.58,0.25
SCP*	85	44		P	0.58
CAY	87	86	0.01-0.3	P	0.58
HDC	112	66	0.01-0.3	P	1.00
PPT*	187	76	0.01-0.3	P	1.00
KIP	203	39	0.01-0.3	P	1.00
GUMO	262	69	0.01-0.3	P	1.00
MAJO	283	54		P	0.70
TATO	288	72		P	0.70
KMI	303	80		P	1.00

* timing problems

Table 5.5: 30 November 1987. Stations for LP models.

shock seismicity, the fault length initially investigated extends 40 km to the north and 100 km to the south of the epicenter.

The LP data are initially used to investigate different source models. Various combinations of multiple point and line sources were tried, including bilateral rupture and unilateral rupture models. The best parameterization of the data is the multiple-point source model using triangular-source elements with $\tau_r = \tau_d = 2$. In this model, the depths of all three subevents are systematically varied over the fault width. The location of subevent 1 is fixed at the epicenter and the positions of subevents 2 and 3 are varied over the length of the fault.

Figure 5.21 contours the normalized rms errors for a depth of 25 km (justified later). The results of this modeling are not robust. Subsequent modeling indicated

Station	Azimuth (deg)	Distance (deg)	Bandpass (Hz)	Type	Weight
SBB	24	73	0.01-1	P,SH	0.60,0.50
AKU*	27	49	0.01-1	P	0.60
GDH	36	37	0.01-1	P	0.60
WFM	78	46	0.01-1	P,SH	0.80,0.50
CAY	87	86	0.01-1	P	0.80
HDC	112	66	0.01-1	P	1.00
PPT#	187	76	0.01-1	P	1.00
KIP	203	39	0.01-1	P	1.00
GUMO	262	69	0.01-1	P	1.00
INU	283	56	0.01-1	P	1.00
KMI	303	80	0.01-1	P	1.00

* analog station
# timing problems

Table 5.6: 30 November 1987. Stations for WWS models.

possible moment release farther north than the initial model for subevent 3. Hence, errors for subevent 3 are shown extended to 80 km north of the epicenter. As illustrated by the shaded region in Figure 5.21, the errors indicate that subevent 2 occurred south of the epicenter (0–80 km south) and subevent 3 north of the epicenter (20–70 km north). The exact position is not well determined.

The WWS data are used to further constrain the positions of the subevents. As suggested by the LP modeling, only southern positions are investigated for subevent 2, and only positions up to 40 km north of the epicenter for subevent 3. Since the trend of the errors for many of the solutions was still decreasing at this point, additional positions up to 80 km north of the epicenter were also investigated. Figure 5.22 shows the errors for the final model. The least error for a centroid depth of 25 km occurs when subevent 3 is 60 km north of the epicenter and subevent 2 is 70 km

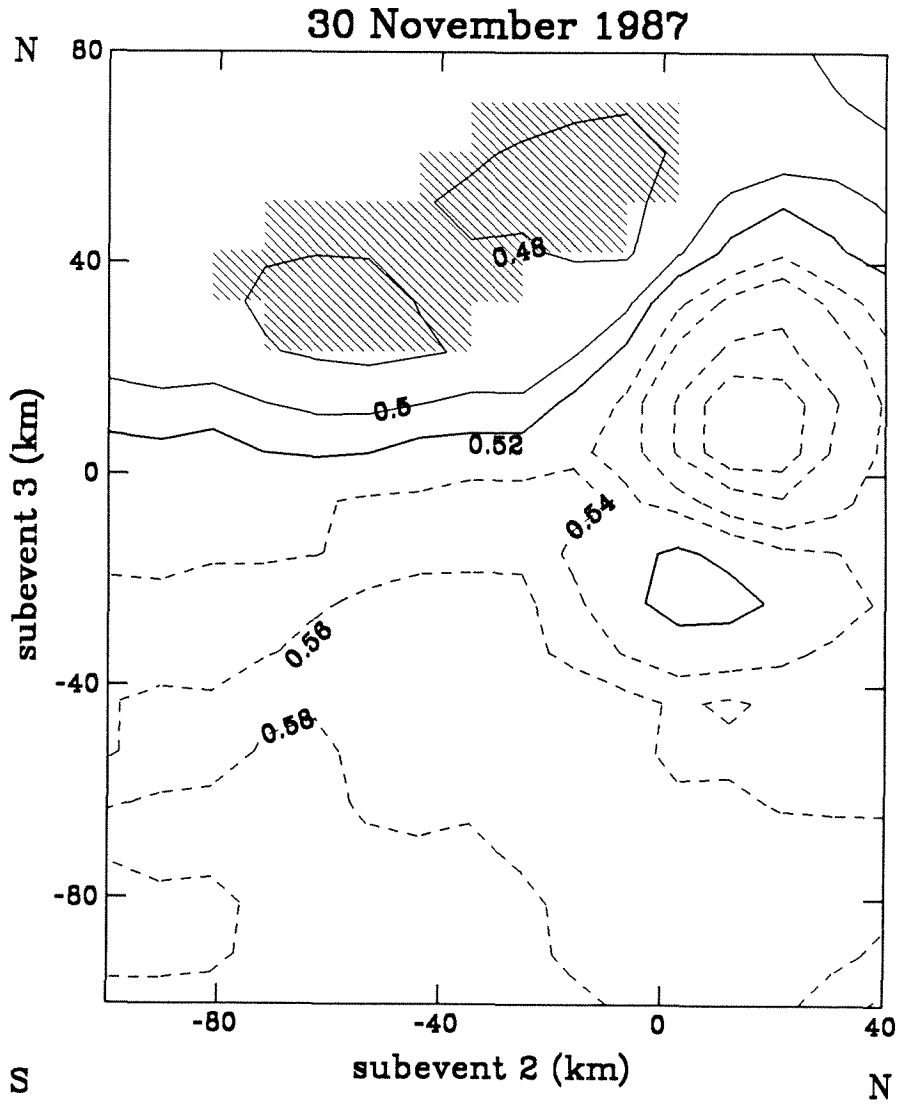

Figure 5.21: Data misfits for the LP data for method N. Contoured are the normalized rms errors for the along strike distance of subevent 3 versus subevent 2 for a fixed centroid depth of 25 km.

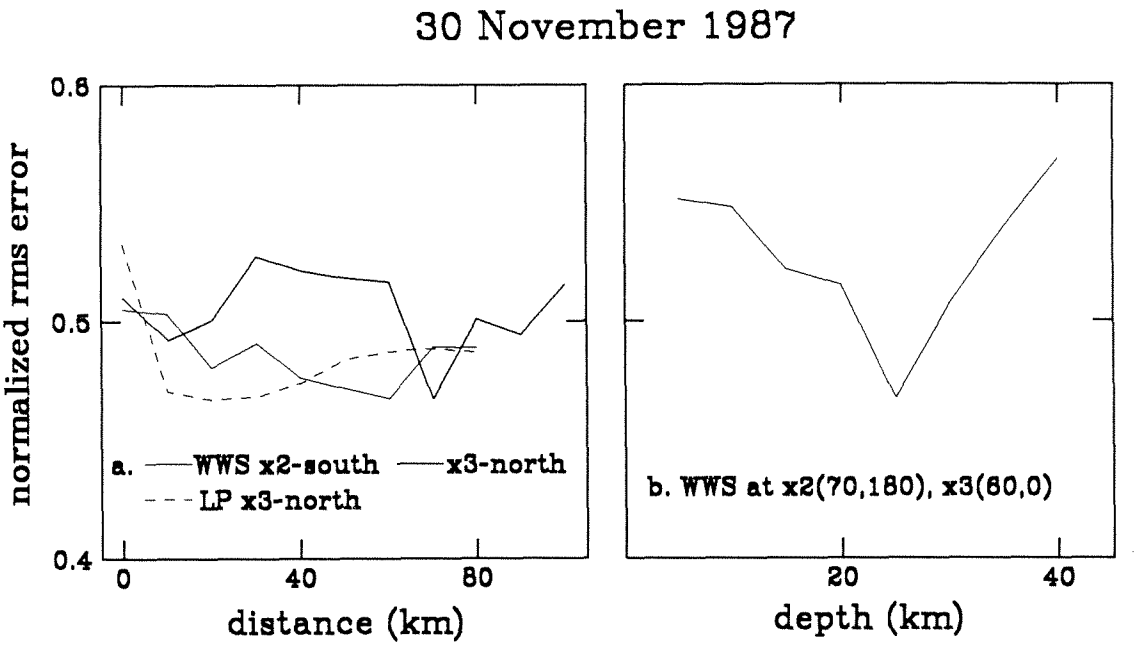

Figure 5.22: Data misfits for the LP (dashed line) and WWS (solid line) data for method N. Plotted are the normalized rms errors versus: a. along strike distance north (thin line) and south (thick line) for a fixed centroid depth of 25 km, and b. centroid depth for a fixed position of subevent 2 at 70 km south and subevent 3 at 60 km north of the epicenter.

south of the epicenter (Figure 5.22a). Figure 5.22b shows that the depth is well constrained at 25 km for these source positions and, in general, is the best depth for most of the multiple-point source models investigated.

The WWS data indicate source positions at 60 km north and 70 km south for subevent 3 and 2, respectively. While the position of subevent 3 is much farther north than the position preferred by the LP data, it is still within the allowable error range. For the same position of subevent 2 at 70 km south, the LP data prefer that

subevent 3 lie between 10–40 km north (Figure 5.22a). A position of subevent 3 at 60 km north for the LP data results in a solution that is inconsistent with the WWS data. As determined from the errors in the LP data, the best position for subevent 3 lies at 20 km north. This solution provides a better overall match to the LP waveform, and the resulting source-time function is consistent with the WWS results.

Figure 5.23 and 5.24 show the resulting focal mechanisms for the two largest subevents, the data and synthetics, and the source-time function for the LP solution — model 2NLP. In general, the synthetics fit the data quite well. Assuming that slip took place on a north-south trend, all three subevents have right-lateral, strike-slip mechanisms. However, their mechanisms differ. The mechanism for subevent 1 (strike 3°, dip 82°, rake 364°) is not too reliable because of its relatively small size. Interestingly enough, it does result in a solution consistent with the first-motion mechanism. The focal mechanism for subevent 2, 2NLP.2, which lies south of the epicenter, is rotated more westerly than the other two mechanisms and dips near vertically. It contrasts with subevent 3, 2NLP.3, which lies to the north and has a roughly north-south strike and dips to the west. 2NLP.2 has approximately the same moment as 2NLP.3. Total moment for this model is 7.7×10^{27} dyne-cm. The source parameters for 2NLP.2 and 2NLP.3 are given in Table 5.7.

For a depth of 25 km and source positions of subevent 2 to the south and subevent 3 to the north, estimates of the error in the focal parameters vary. Formal errors indicate that the focal mechanism for 2NLP.2 is better constrained than 2NLP.3. The different models suggest that for 2NLP.2, the strike and dip may be underestimated

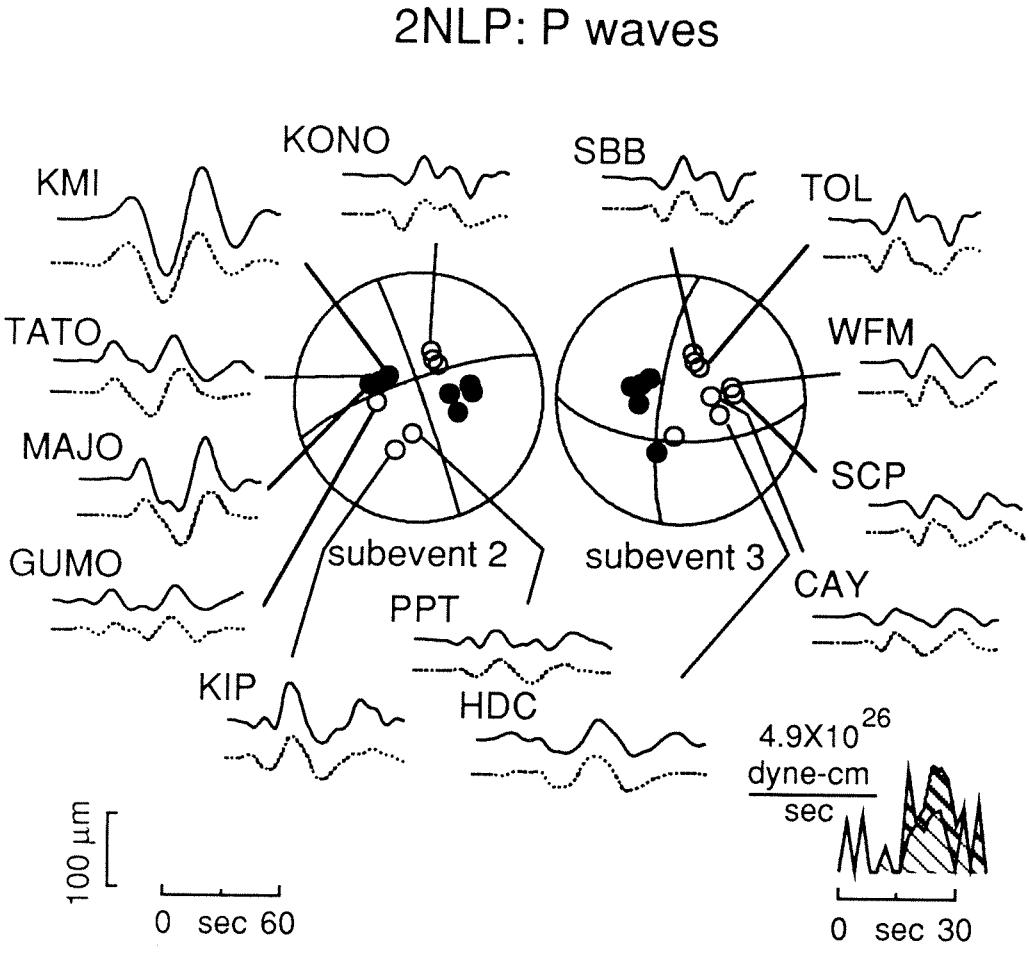

Figure 5.23: 2NLP. Observed (solid line) and synthetic (dashed lines) LP P-wave seismograms. Shown in the center of the figure is the lower hemisphere focal mechanism for the two largest subevents, 2NLP.2 and 2NLP.3. Solid circles represent compressional, and open circles, dilatational first motions. Source parameters are given in Table 5.7. The combined source-time function for 2NLP.1 (unhatched), 2NLP.2 (light hatching), and 2NLP.3 (dark hatching) is shown at bottom right. Time and amplitude scales are shown at bottom left. Amplitudes of the observed and synthetic seismograms are normalized to the identical instrument at a distance of 60° with a peak magnification of 1.

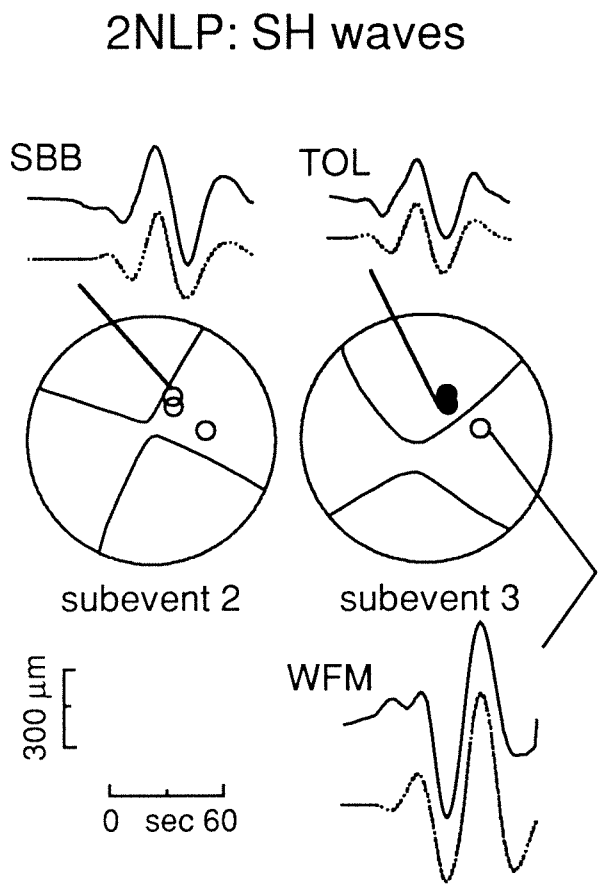

Figure 5.24: 2NLP. Observed (solid line) and synthetic (dashed lines) LP SH-wave seismograms. Symbols are described in Figure 5.23.

Model	Strike (deg)	Dip (deg)	Rake (deg)	Depth (km)	Delay (sec)	Velocity (km/sec)	Dist (km)	Azi (deg)	Moment (dyne-cm)$\times 10^{26}$
FM	170	92	177	10*					
CMT	175	110	172	15*					7.3
2NLP	160	92	168	25	10		70	180	3.2
	188	76	208	25	16		20	0	3.5 (7.7)
2NWWS	171	90	188	25	11		70	180	4.6
	188	98	187	25	20		60	0	2.5 (8.2)
2KLP	177	97	173	20		#	30-60	180	2.0
							90	180	3.8
							20-30	0	0.8 (5.3)
2KWWS	180	94	179	20		#	30-60	180	3.9
							80	180	3.7
							30	0	0.5 (5.6)

* fixed
\# see text.
For abbreviations, see Table 5.4.

Table 5.7: 30 November 1987. Model parameters.

by 5° and 10°, respectively, and rake may vary by ±5°. For 2NLP.3, both the strike and dip may be overestimated by 5° and the rake by 10°. This error range suggests that the two subevents may not be so different.

Figures 5.25 and 5.26 show the WWS results for model 2NWWS. The general shape of the waveforms is well modeled. However, not all of the features are satisfactorily explained. This can be due to several causes. First, least-squares inversion techniques tend to match the largest power in the data. Hence, good fits to smaller moment carrying sources tend to be sacrificed to fit the larger sources. Second, waveforms are poorly fit if arrivals are not coherent enough between stations. Lastly, both receiver and source crustal structure can have an important effect on the observed waveforms.

For many stations, the first arrivals are late. Several stations (SBB, AKU, HDC,

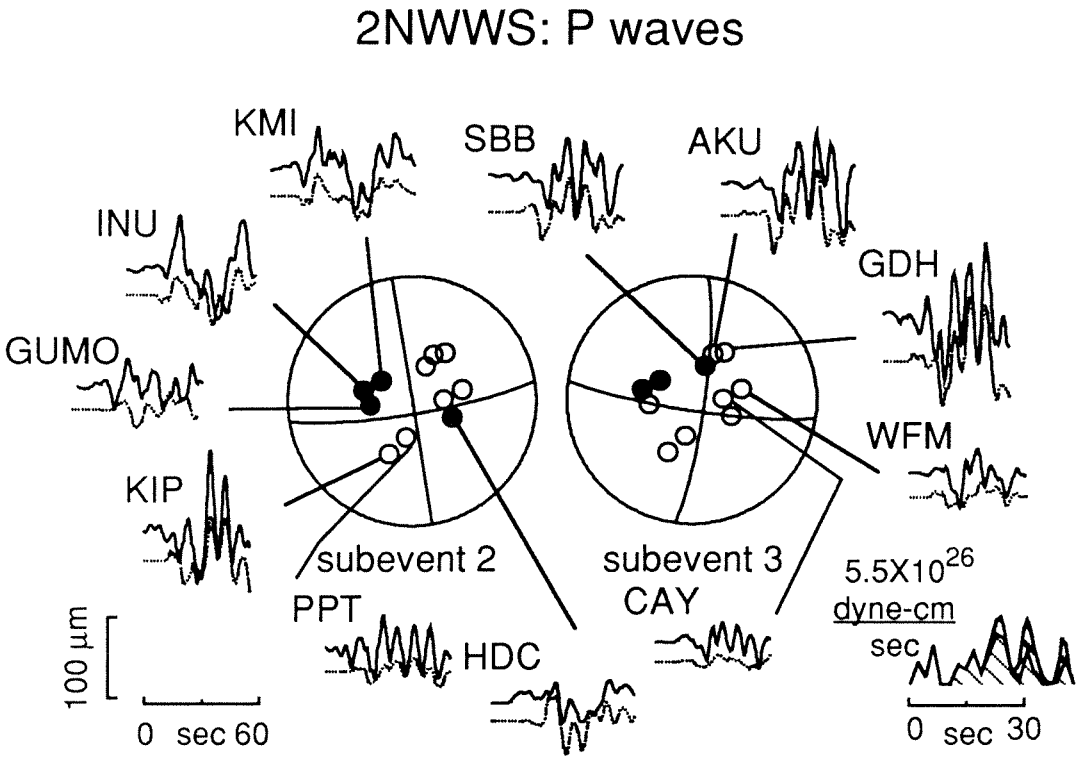

Figure 5.25: 2NWWS. Observed (solid line) and synthetic (dashed lines) WWS P-wave seismograms. Symbols are described in Figure 5.23.

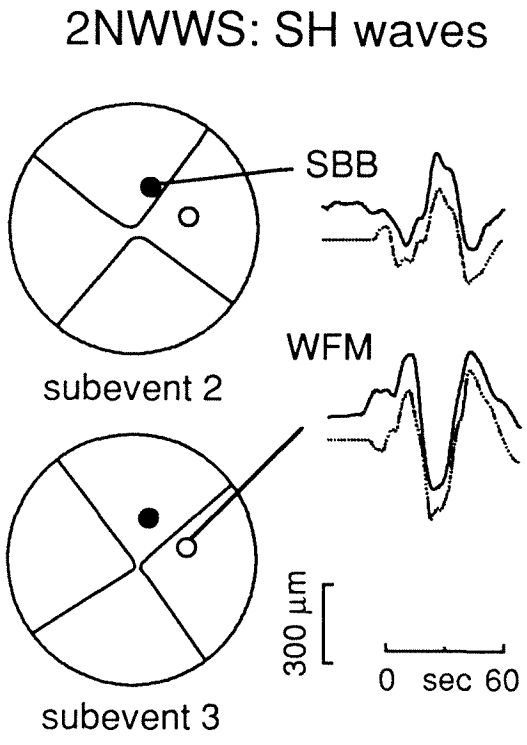

Figure 5.26: 2NWWS. Observed (solid line) and synthetic (dashed lines) WWS SH-wave seismograms. Symbols are described in Figure 5.23.

and GUMO) lie very near P-wave nodes for the first subevent, 2NWWS.1, contributing to the low amplitudes and lateness of the first arrival in the synthetics. Misfits to the data may also indicate that the source at this bandwidth is more complex than a simple, three-point source model.

Slightly less than half of the stations (CAY, PPT, KIP, GUMO, INU) are located on islands. Local crustal structure and water depth vary greatly between these stations. P-waves from strike-slip type earthquakes, however, are more sensitive to source structure (Langston, 1977). Both the 17 and 30 November 1987 earthquakes occurred near the base of the continental slope. In this region, both water depth and crustal structure change rapidly towards the NNE as oceanic crust abuts the Yakutat terrane (von Huene *et al.*, 1979). Such near source heterogeneity will affect the complexity of the signal. This may explain why the WWS waveforms at stations to the NNW are relatively complex compared to the remainder of the data set for both events. The third event of 6 March 1988, modeled below, lies well away from this boundary. Waveform data for that event do not show any substantial difference in complexity with azimuth. Hence, the boundary between the Pacific plate and the Yakutat terrane affects the coherency of the signal and the ability to model all arrivals.

Focal mechanisms for the three subevents indicate strike-slip motion. 2NWWS.1 is modeled as a left-lateral, strike-slip event, while subevents 2 and 3, 2NWWS.2 and 2NWWS.3, respectively, are modeled as right-lateral. As discussed above, the discrepancy is most likely due to resolution and coherency problems of the first arrival. The poor fit of the waveforms to the first arrivals indicates that the focal

mechanism for 2NWWS.1 is unreliable. The focal mechanisms for 2NWWS.2 and 2NWWS.3 indicate right-lateral motion on a north-south trending fault. The strike of 2NWWS.2 trends NNW-SSE and dips vertically, while the strike of 2NWWS.3 trends NNE-SSW with an easterly dip. 2NWWS.2 is roughly twice as large as 2NWWS.3. Total moment for this model is 8.2×10^{27} dyne-cm. Source parameters for 2NWWS.2 and 2NWWS.3 are given in Table 5.7.

Formal errors again indicate that 2NWWS.2 is better resolved than 2NWWS.3 and that the focal mechanisms for 2NWWS are better resolved than for 2NLP. For a depth of 25 km and distances for subevents 2 and 3 similar to the final model, estimates of error in the focal parameters vary. For 2NWWS.2, the strike and dip are perhaps underestimated by 10°, and rake is overestimated by 10°. For 2NWWS.3, the strike and rake may be overestimated by 10° and dip underestimated by 10°. Again, these error bounds would bring the focal mechanisms of 2NWWS.2 and 2NWWS.3 in better agreement with one another.

The LP and WWS data are also modeled using method K to further investigate the above variations and discrepancies in the focal mechanisms and source positions. Here, the fault plane dimensions are comparable to those searched in the previous models. The fault plane extends 40 km to the north and 100 km to the south of the epicenter. For the LP data, inversion for a single source constrains the total source duration to be 36 sec, where $\tau_r = 16$ sec, and $\tau_d = 20$ sec, and a time delay of 10 sec (Figure 5.27). The total duration time is in good agreement with the above results. The source lies at a depth of 10 km and is located 40 km south of the epicenter. The north-south striking fault plane dips to the east much like the CMT solution. This

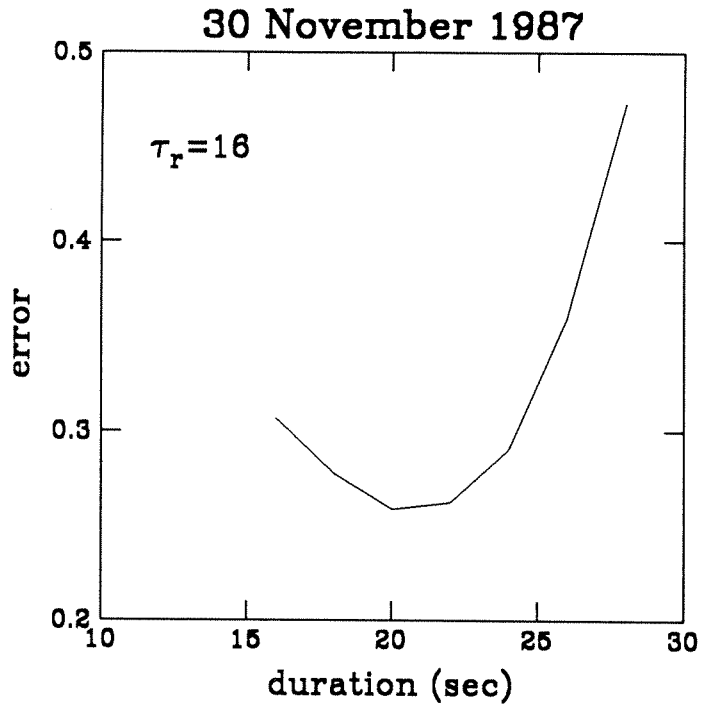

Figure 5.27: Data misfits for the LP data in method K. Plotted is the error versus τ_d of the single best-fitting trapezoidal source function where $\tau_r = 16$.

solution fails to fit the complexities seen in the waveforms (Figure 5.28b). Subsequent iterations using the same parameterization do little to improve the waveform matches (Figure 5.28c).

Systematic variation of the time function shows that the source element that best matches the rise times in the waveform has a much shorter triangular time function of $\tau_r = \tau_d = 5$ sec. Figure 5.28d shows the results for one iteration. Figure 5.29 contours the correlation functions and corresponding best-fit focal mechanisms. Several

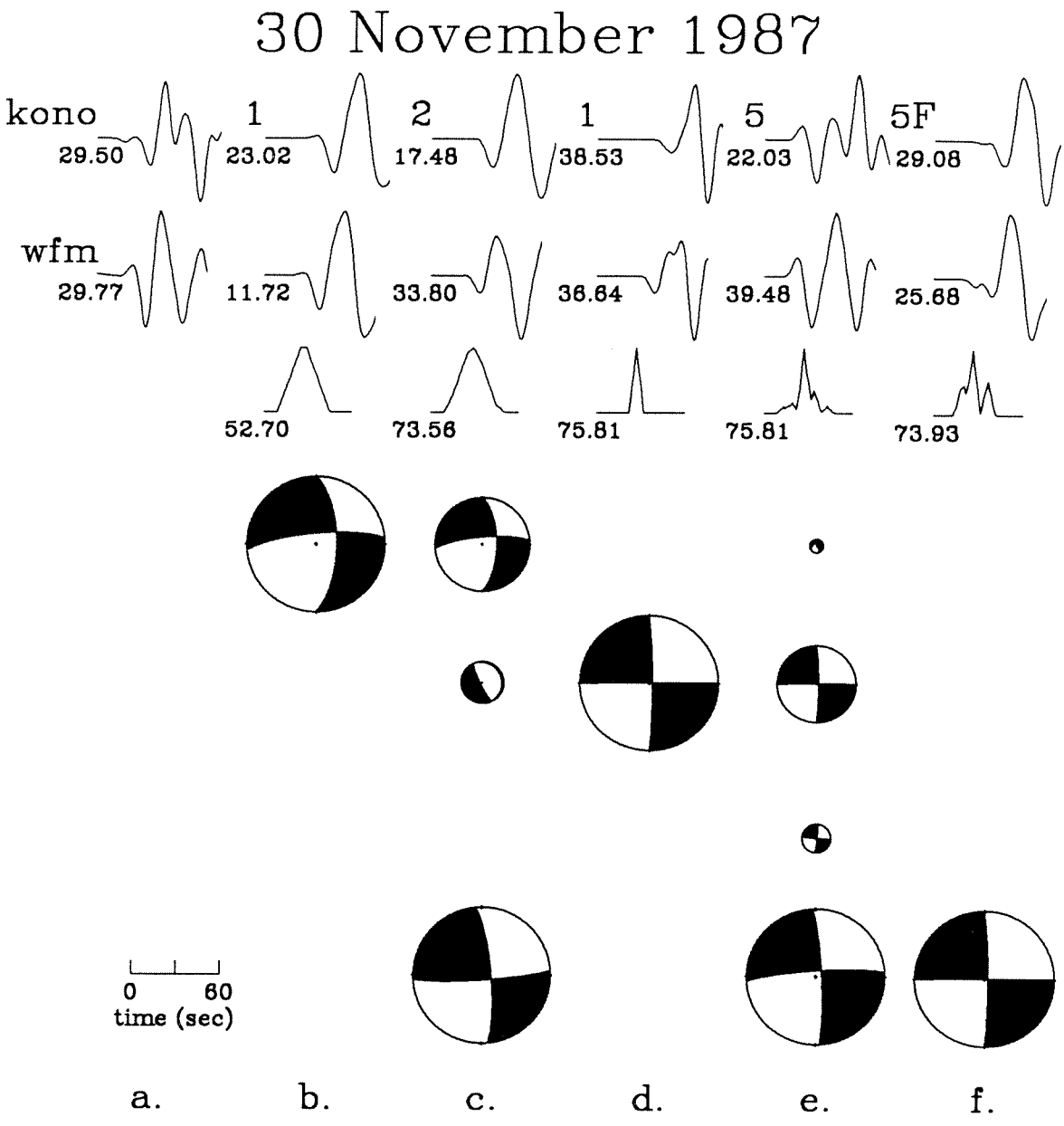

Figure 5.28: Layout is described in Figure 5.13. Shown are: a. data for stations KONO and WFM; synthetics for models with $\tau_r = 16$ and $\tau_d = 20$ sec and time varying focal mechanisms for b. 1 and c. 2 iterations, and $\tau_r = \tau_d = 5$ sec, for d. 1 and e. 5 iterations; and f. synthetics for a fixed focal mechanism for 5 iterations.

isolated peaks on the diagram indicate the complexity of the event. By far, the best correlation occurs at 22 sec at a distance of 90 km south of the epicenter. At this time, the best-fit focal mechanisms are all near vertical, right-lateral strike-slip on the north-south trending plane. Before and after this time, the correlation decreases rapidly, but the mechanism remains stable in an approximately 15 sec time window. Outside this window, the focal mechanism changes rapidly and flips to left-lateral, strike-slip type mechanisms. In general, a large time shift of the data reverses the polarity of the first motions, causing the reverse, in this case, left-lateral, focal mechanisms. The position of the other correlation maxima corresponds to these regions of left-lateral mechanisms. Since previous analysis indicated a right-lateral mechanism for this event, the solutions outside the time window seem unlikely. Hence, the timing of the first subevent appears well constrained. Inside the time window, the correlation does not change rapidly in the along strike direction and suggests a spatial resolution on the order of 30 to 40 km. Hence, the position of the subevent is not very well determined. The best position lies just in front of the rupture front and corresponds to a rupture propagation of a little over 4 km/sec. In the final inversion, the rupture front is allowed to propagate at essentially an infinite speed.

Figure 5.29 illustrates the complexity of the event and suggests that multiple subevents with different mechanisms are needed to explain the data. To test this observation, the focal mechanism is constrained for 5 iterations to that of the initial subevent (subevent 2KLP.1 below). The solution is partly illustrated in Figure 5.28f. In this model, moment release begins at 13 sec, leaving the first portion of the record unmodeled. In general, the synthetics appear mistimed and do not match the

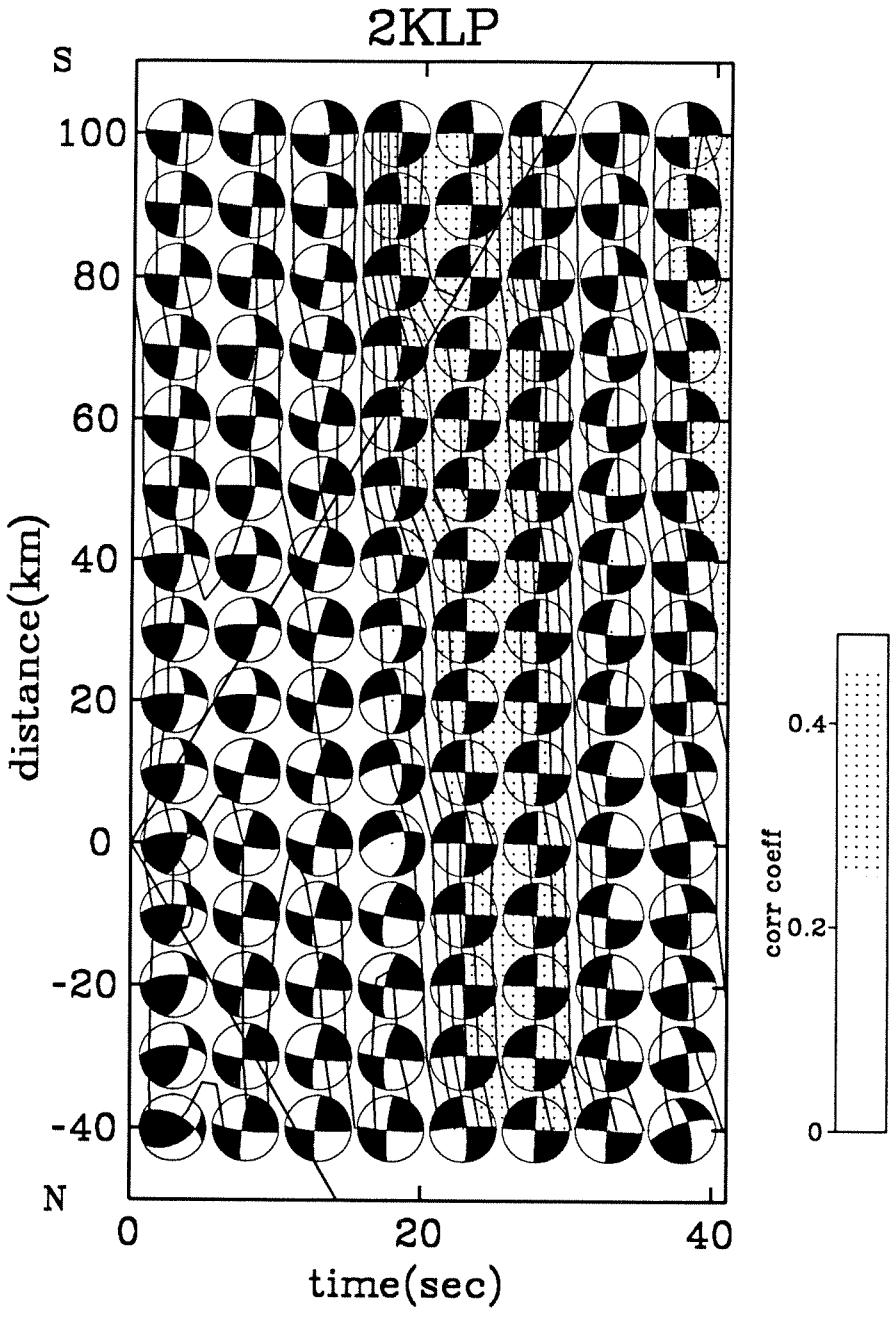

Figure 5.29: 2KLP. Layout is described in Figure 5.14.

complexities of the data. Synthetics for stations to the west have low amplitudes. Additional iterations have too little moment to affect the amplitude and shape of the synthetics significantly. Clearly, fixing the focal mechanism in the inversion is inadequate to explain the waveform data, and some variation in the focal mechanism is necessary.

Model 2KLP allows the focal mechanism to vary in time for 5 iterations. The focal mechanisms for the three largest subevents, 2KLP.1, 2KLP.2, and 2KLP.5 are shown in Figure 5.28e along with the best double-couple sum of all 5 subevents. The two largest subevents, 2KLP.1 and 2KLP.5, have similar near vertical, right-lateral mechanisms on the north-south trending plane. Subevents 2KLP.2 and 2KLP.4 occurring earlier in time have similar mechanisms that are also predominantly strike-slip. With respect to 2KLP.1 and 2KLP.5, their mechanisms are rotated counterclockwise and have very different slip angles.

Figures 5.30 and 5.31 show the data and synthetics for model 2KLP. The focal mechanism shown and given in Table 5.7 is the best double-couple sum of the 5 subevents comprising the solution. The overall match to the waveforms is good. Moment release does not begin for 8 sec; hence, several stations (KIP, GUMO, PPT) are noticeably ill-matched in the beginning of the waveform. In model 2NLP, the beginning of the waveforms is reasonably well-matched by forcing the source-time function to begin at 0 sec. Constraining the first source element to begin within the first 2 or 5 sec also forces moment release to begin early (1 and 4 sec, respectively). However, none of the subevents satisfy the observed first motion data. The signal is too small to be modeled.

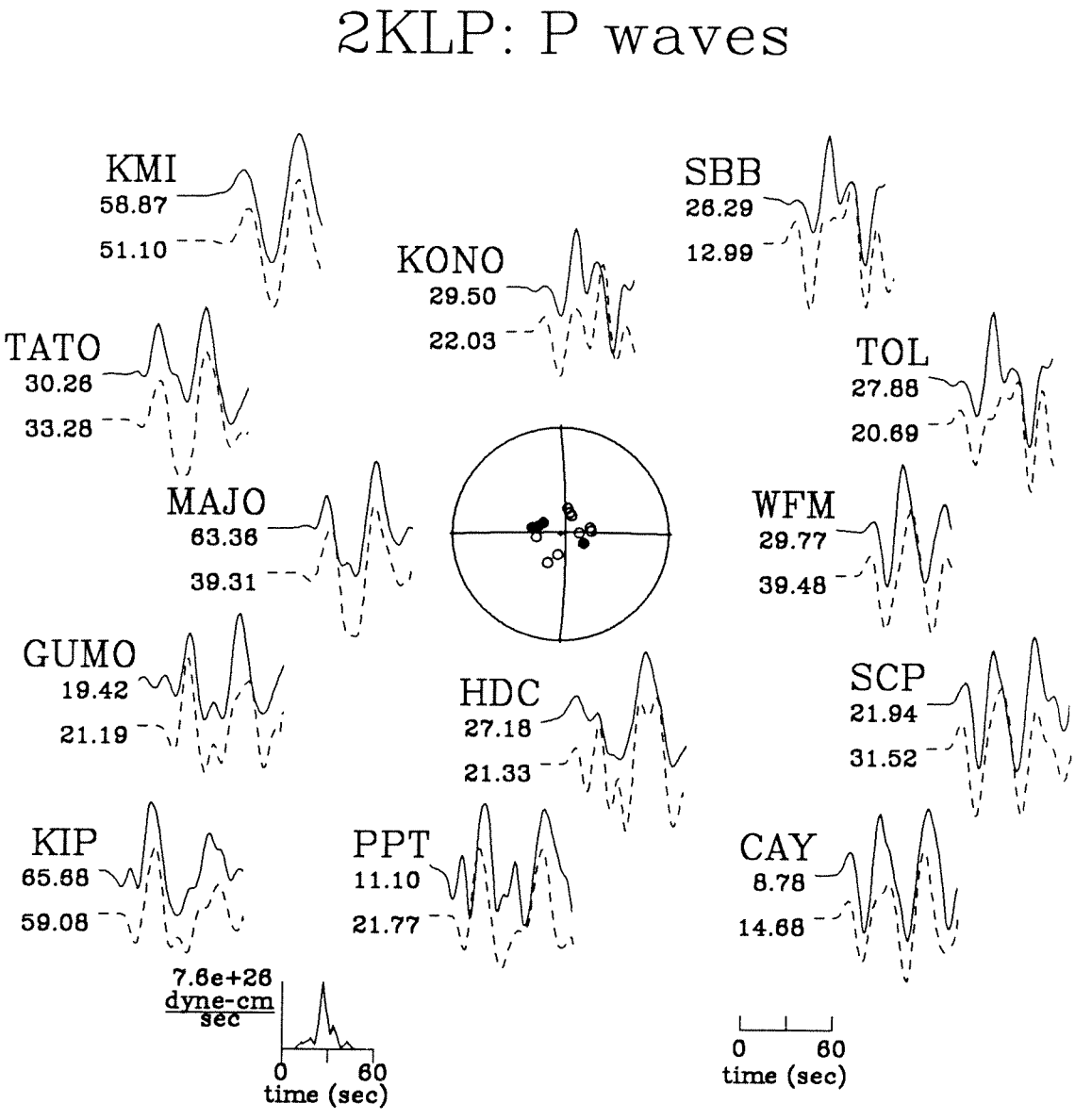

Figure 5.30: 2KLP. Observed (solid line) and synthetic (dashed lines) LP P-wave seismograms. Source parameters are given in Table 5.7. Symbols are described in Figure 5.15.

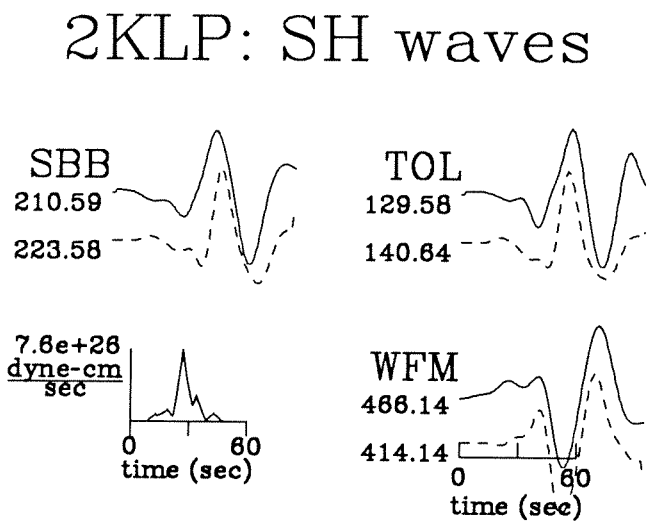

Figure 5.31: 2KLP. Observed (solid line) and synthetic (dashed lines) LP SH-wave seismograms. Source parameters are given in Table 5.7. Symbols are described in Figure 5.15.

In model 2KLP, the largest subevent, 2KLP.1, is located at a depth of 20 km and at a distance of 80 km south of the epicenter. This subevent accounts for 55% of the total moment release. Two of the subevents are located north of the epicenter at a distance of 20–30 km and account for approximately 12% of the total moment release. The best double-couple sum has a scalar moment of 5.3×10^{27} dyne-cm with an 8% nondouble-couple component

Inversion of the WWS data required source elements with a faster rise time and shorter duration ($\tau_r = \tau_d = 3$ sec) to match the data. Similarly to the LP data, first motion times as observed on the broadband or short-period records were initially used as the start times for the data. However, this resulted in almost pure thrust or normal focal mechanisms for the largest subevents. Poor waveform matches suggest that this was caused by mistiming of the data and show the sensitivity of the solution to timing and hence, coherency between the waveforms. Because of the complexity of the event, timing corrections independent of the LP results could not be derived. Hence, instead of using the first-motion timing, the final timing used for the LP records are also used for the WWS records. Inversion with these times resulted in strike-slip type subevents. No additional timing adjustments were used to model the data.

The correlation functions for the WWS data show several peaks (Figure 5.32). The best correlation occurs at 25 sec at a position 40 km south of the epicenter. The corresponding best-fit focal mechanisms are similar to those for the LP data. They are extremely stable in the along strike directions but change rapidly to mechanisms opposite to the best-fit mechanism outside an approximately 15 sec long time window.

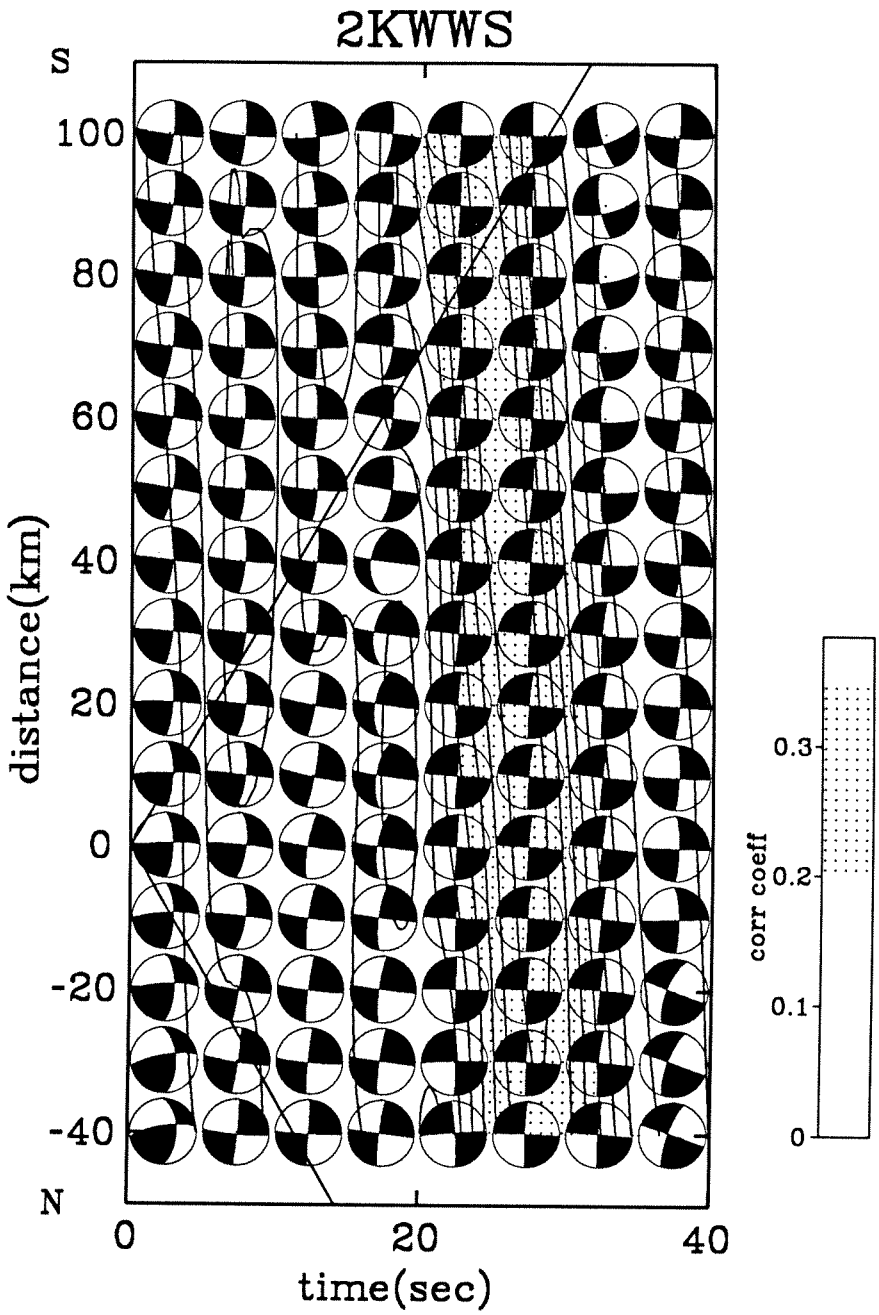

Figure 5.32: 2KWWS. Layout is described in Figure 5.14.

Again, the position of the other correlation maxima corresponds to these regions of opposite mechanisms. However, the pattern of the correlation functions for the WWS data is different from the LP data. Several maxima do occur within the 3.5 km/sec rupture front. For consistency with 1KLP, a rupture velocity of essentially infinite speed is again used here, though in the final model, the solution has no subevents exceeding a speed of 3.5 km/sec.

The WWS data are much more complex than the LP data and cannot be modeled by a single subevent. The final WWS model, model 2KWWS, allows the mechanism to vary in time. Figures 5.33 and 5.34 show the data and synthetics for model 2KWWS. The focal mechanism shown and given in Table 5.7 is the best double-couple sum of the 10 subevents comprising the solution. Overall, the features in the waveforms are adequately modeled. Similarly to 2NWWS, many features are still not explained (see above discussion). Moment release begins late at 11 sec; hence, the beginning portion of the waveforms is not modeled.

In model 2KWWS, the focal mechanisms are consistently right-lateral strike-slip on the north-south trending plane. The difference in strike, dip, and rake between the largest subevents are approximately $\Delta\phi = 2°$, $\Delta\delta = 10°$, and $\Delta\lambda = 10°$. Most of the moment release occurs between 20–60 km south of the epicenter, with the two largest subevents at 40 and 60 km south at a depth of 20 km. Essentially, no moment release occurs to the north. The best double-couple has a scalar moment of 5.6×10^{27} dyne-cm with a 4% nondouble-couple component.

Overall, the above models agree with one another. The earthquake consisted of multiple, right-lateral, strike-slip subevents with different focal mechanisms on a

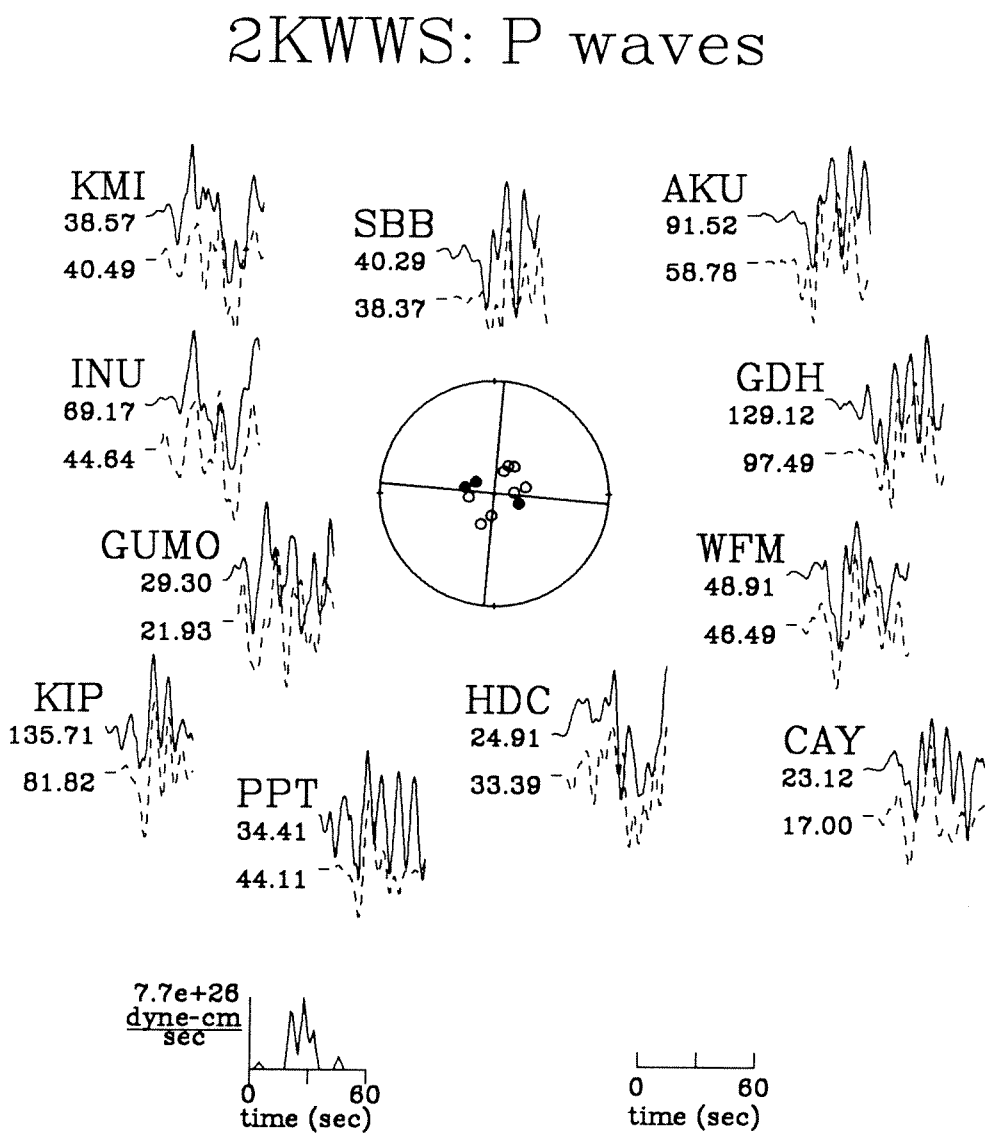

Figure 5.33: 2KWWS. Observed (solid line) and synthetic (dashed lines) WWS P-wave seismograms. Source parameters are given in Table 5.7. Symbols are described in Figure 5.15.

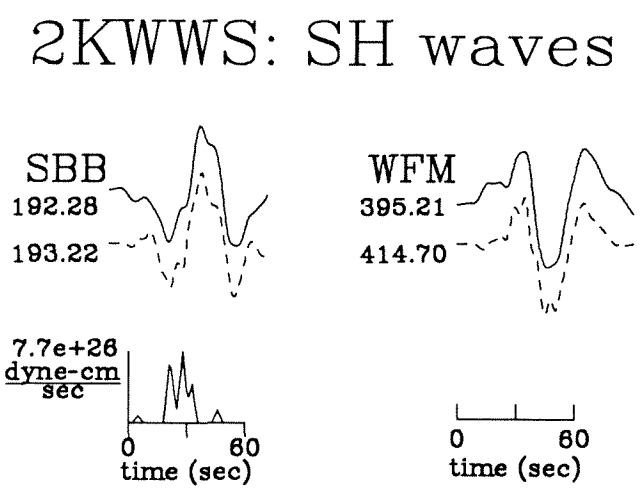

Figure 5.34: 2KWWS. Observed (solid line) and synthetic (dashed lines) WWS SH-wave seismograms. Source parameters are given in Table 5.7. Symbols are described in Figure 5.15.

north-south trending plane at a centroid depth of 20–25 km. Most of the moment release occurred to the south of the epicenter between a distance of 40 to 90 km (Figure 5.35). Moment release begins with a small, poorly resolved subevent. The major portion of the total moment release does not initiate until approximately 15 sec after the first arrival. Total moment release for these models corresponds to $M_w = 7.8$.

The first motion results, using both teleseismic and local data, suggest that the event initiated as a near vertical, right-lateral, strike-slip earthquake trending NNW-SSE. The CMT solution has a NNW-SSE trending plane dipping 70° to the west. The focal mechanism solutions in the above models trend both NNW-SSE and NNE-SSW and dip both to the east and west, but all agree with one another within the errors of

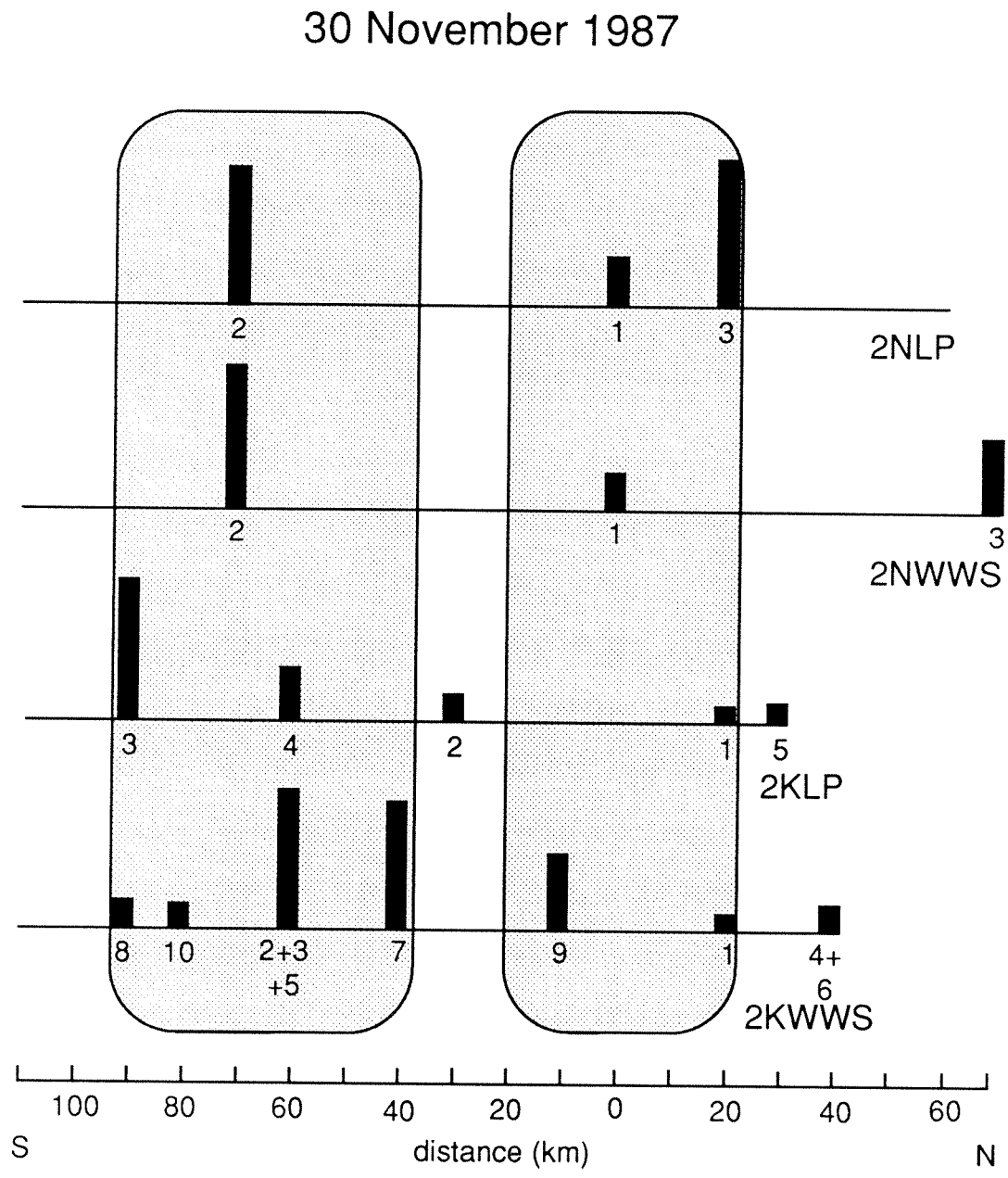

Figure 5.35: Event 2. Symbols are described in Figure 5.20. The number under each subevent indicates the initiation order of the subevent.

their respective models. Modeling using method K suggests that these discrepancies are due to source finiteness and time variations in the focal mechanism. For models 2NLP and 2NWWS, it seems reasonable that the subevents idealized as point sources have a finite extent that is unresolvable from the data using method N. In 2KLP and 2KWWS, positions of individual source elements are not held fixed and are allowed to vary over the fault plane within a distance prescribed by the rupture velocity. For 2KLP, this results in a small amount of moment release bracketing the epicenter and larger moment release subevents at both ends of the fault. For 2KWWS, moment release is distributed over a wider distance range. Their spatial-temporal sequence cannot be easily described by a simple line- or point-source model (Figure 5.35).

The above models indicate that up to 50% of the total moment release occurred near to or north of the epicenter. Estimates of moment release vary between the models and are not well resolved. 2NLP.3 gives the largest estimate but is located 20 km north of the epicenter. 2NWWS.3 is located farther to the north at 60 km. Using the same data set and a fault extended to 90 km to the north, method K shows there is a tendency to place moment release even farther north than 60 km. Positions greater than 40 km are located much farther north than the extent of the aftershock zone and are most likely due to instabilities of the inversion. Constraining the possible rupture extent lowers the total percentage of moment released to the north as the sources become closer to the epicenter.

5.5.3 6 March 1988

Tables 5.8 and 5.9 summarize the data modeled. Inspection of the waveforms suggests that this is the simplest event in the sequence. Unlike the first two events, no

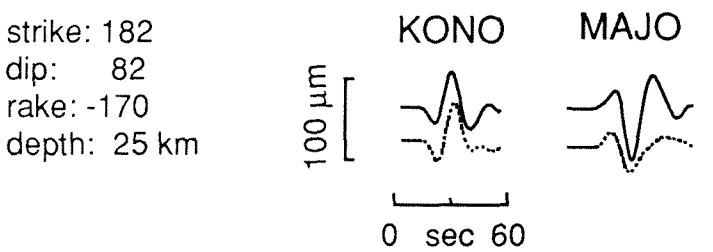

Figure 5.36: Observed (solid line) and synthetic (dashed lines) LP P-wave seismograms for KONO and MAJO for a single point-source model.

precursory arrival is evident on the LP records. The WWS records show a small arrival at the beginning of many records, which has too small an amplitude to model. For method N, trapezoidal source elements of varying rise times and durations are used initially to model the data. Models using triangular source elements with $\tau_r = \tau_d = 2$ sec fit the data the best. The LP data are initially modeled as a single point or line source. As suggested by the aftershock seismicity, sources investigated lie both to the north and to the west of the epicenter. The best-fitting, single source model is a point-source model, which explains most of the data quite well. However, matches of the synthetics to the data for stations at a westerly azimuth are not good. The synthetics are not as impulsive as the data (Figure 5.36) suggesting, a westerly source propagation.

Different combinations of line and point sources were tried next. Both line and point sources are allowed to lie either to the north or west of the epicenter. In general,

Station	Azimuth (deg)	Distance (deg)	Bandpass (Hz)	Type	Weight
KEV	4	53	0.01-0.3	P,SH	1.00,0.30
KONO	16	61		P	0.70
GRFO	18	71		SH	0.18
SBB	23	74	0.01-0.3	P,SH	0.70,0.18
WFM	76	46	0.01-0.3	P,SH	0.70,0.30
SCP*	83	44		P	0.60
CAY	87	86	0.01-0.3	P,SH	0.70,0.30
ANMO*	117	33		SH	0.30
PPT*	187	75	0.01-0.3	P	1.00
KIP	204	38	0.01-0.3	P	1.00
GUMO	263	69		P,SH	0.70,0.30
MAJO	284	54		P	0.70
INU	284	56	0.01-0.3	SH	0.18
TATO	289	72		P,SH	0.70,0.18
BJI	302	63		P,SH	0.60,0.30
CHTO	303	89		P	0.60
HIA	307	54		P	0.60
WMQ	324	71		SH	0.30

* timing problems

Table 5.8: 6 March 1988. Stations for LP models.

Station	Azimuth (deg)	Distance (deg)	Bandpass (Hz)	Type	Weight
KEV	4	53	0.01-1	P,SH	1.00,0.35
SBB	23	74	0.01-1	P,SH	1.00,0.35
WFM	76	46	0.01-1	P,SH	1.00,0.35
CAY	87	86	0.01-1	P	1.00
PPT*	187	75	0.01-1	P,SH	1.00,0.35
KIP	204	38	0.01-1	P,SH	1.00,0.35
GUMO	263	69	0.01-1	P	1.00
INU	284	56	0.01-1	P,SH	1.00,0.35
BJI	302	63	0.01-1	P	0.50
KMI	303	81	0.01-1	P	0.50
HIA	307	54	0.01-1	P,SH	0.50,0.35
LZH	308	72	0.01-1	P	0.50
WMQ	324	71	0.01-1	P,SH	1.00,0.35

* timing problems

Table 5.9: 6 March 1988. Stations for WWS models.

the error in the fit to the data becomes larger if most of the moment release is forced to lie away from the epicentral region. For all models, source depths between 5–40 km and rupture velocities between 0.0–5.0 km/sec are systematically investigated.

The best parameterization consists of one line source propagating to the west and one point source at the epicenter. Figures 5.37a and 5.37b show the misfits between the observed and calculated LP seismograms. As shown in Figure 5.37b, the centroid depth for a fixed rupture velocity of 3.5 km/sec lies near 15–20 km. For a centroid depth of 15 km, the rupture velocity is not well resolved. The least error solution occurs at 3.5 km/sec, but a velocity between 2.0–4.0 km/sec is within the acceptable error range (Figure 5.37a). The WWS data further constrain the centroid depth. Figure 5.37d shows that the source depth for a rupture velocity of 3.5 km/sec is well

Model	Strike (deg)	Dip (deg)	Rake (deg)	Depth (km)	Delay (sec)	Velocity (km/sec)	Dist (km)	Azi (deg)	Moment (dyne-cm)$\times 10^{26}$
FM	170	83	182	10*					
CMT	182	75	192	15*					4.9
3NLP	181	62	186	15		3.5		268	3.2
	184	80	170	15	13				1.7 (4.9)
3NWWS	179	79	187	15		3.5		268	2.9
	189	97	176	15	13				1.5 (4.4)
3KLP	182	74	180	20		3.5#	0-20	180	4.4
						3.5#	40	0	0.5 (3.9)
3KWWS	176	81	189	10		3.5#	0-20	270	4.4
						3.5#	10	90	1.1 (4.3)

* fixed
\# maximum rupture velocity
For abbreviations, see Table 5.4.

Table 5.10: 6 March 1988. Model parameters.

constrained by the WWS data at 15 km. Rupture velocity is not as well constrained — the best solution is at a velocity of 3.5 km/sec but can be as low as 2.0 km/sec (Figure 5.37c).

The preferred LP model, model 3NLP, begins with subevent 3NLP.1 propagating towards the west at a velocity of 3.5 km/sec at a depth of 15 km. Subevent 2, 3NLP.2, begins at 13 sec and is modeled as a point source at a depth of 15 km below the epicenter. It has roughly half the moment as 3NLP.1. The two largest moment releasing episodes occur at a distance of approximately 21 and 35 km from the epicenter and at an azimuth of 268°. Total moment for this model is 4.9×10^{27} dyne $-$ cm. See Table 5.10.

Figures 5.38 and 5.39 show the resulting focal mechanisms for the two subevents, the data, synthetics, and the source-time function for model 3NLP. The synthetics are an excellent fit to the data. One exception is the P-wave at station GUMO.

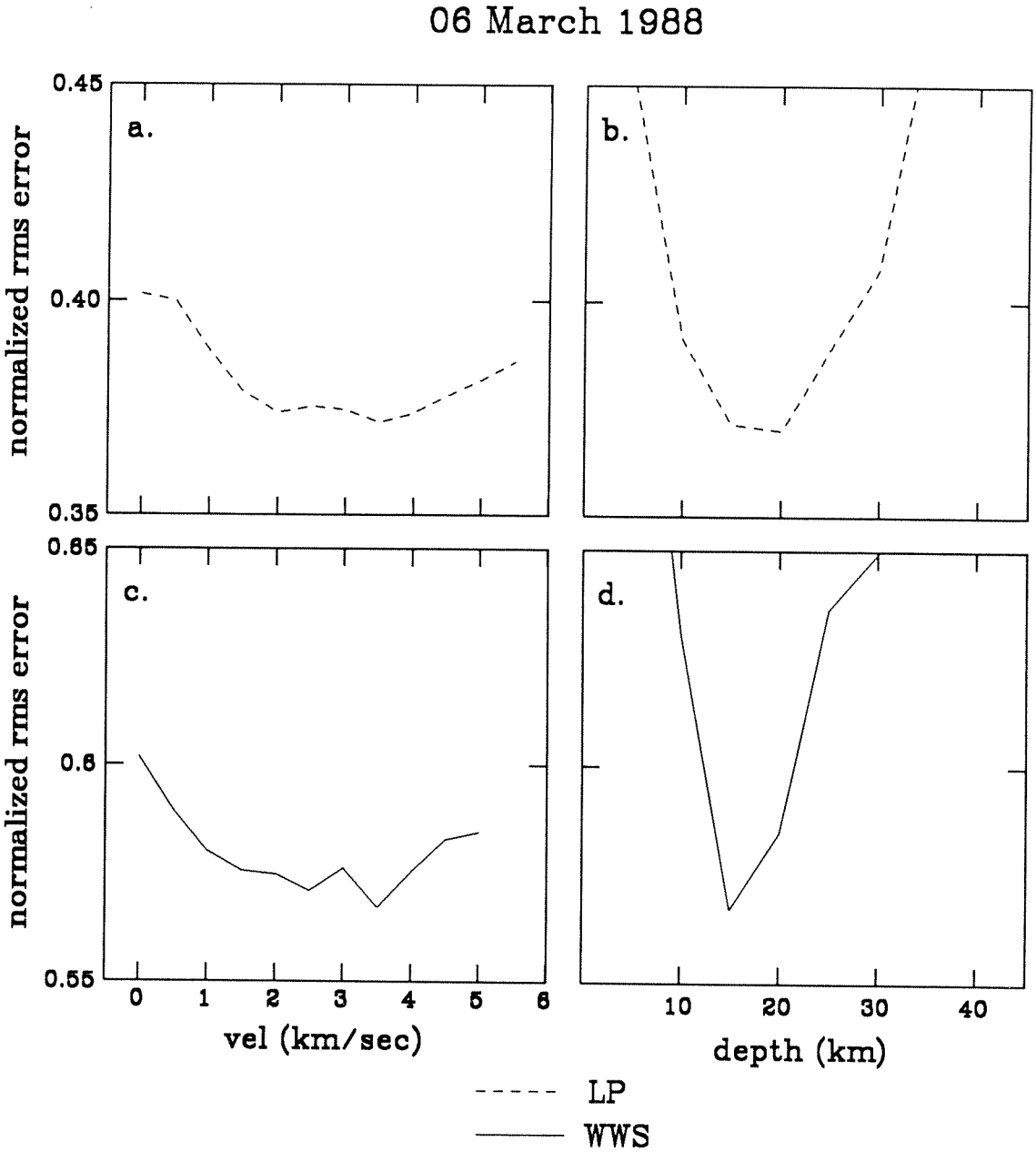

Figure 5.37: Data misfits for method N. Plotted are the normalized rms errors versus: a. velocity for a fixed centroid depth of 15 km, b. centroid depth for a fixed velocity of 3.5 km/sec for the LP data, c. velocity for a fixed centroid depth of 15 km, and d. centroid depth for a fixed velocity of 3.5 km/sec for the WWS data.

GUMO lies near the node of the first subevent, which causes the onset of the event in the synthetic to have a very low amplitude.

The focal mechanisms of the two subevents are very similar. Both subevents are strike-slip with moderate dips. 3NLP.1 is left-lateral rupturing towards the west along a steeply, southerly dipping fault plane. 3NLP.2 is located at the epicenter, which lies at the junction of both the westerly and northerly aftershock seismicity trends. Hence, the sense of motion is ambiguous. For the range of velocities investigated at a fixed, centroid depth of 15 km, the estimates of the focal parameters are stable. For the inferred fault plane for 3NLP.1, the estimates of the strike vary by $\pm 10°$, the dip may be underestimated by 3°, and the rake overestimated by 5°. For the north-south nodal plane for 3NLP.2, the estimates of the strike vary by $\pm 10°$, dip $\pm 2°$, and rake $\pm 2°$.

The final WWS model, model 3NWWS, is in good agreement with model 3NLP. Figures 5.40 and 5.41 show the results for model 3NWWS. The synthetics match most of the features in the data quite well. As shown, both subevents have strike-slip mechanisms. The focal mechanism for subevent 1, 3NWWS.1, is in good agreement with that from model 3NLP.1. The errors are estimated from the range of focal parameters from models with a depth of 15 km for the range of velocities investigated. The estimated error for the focal parameters is $\pm 1°$. Subevent 2, 3NWWS.2, is rotated clockwise with respect to 3NWWS.1, and its focal mechanism is not as well resolved. The strike may be overestimated by 5°, dip by 3° and the slip may vary by $\pm 1°$. 3NWWS.1 again has roughly twice the moment as 3NWWS.2, which begins at 13 sec. Moment release associated with 3NWWS.1 occurs between a distance of 7–

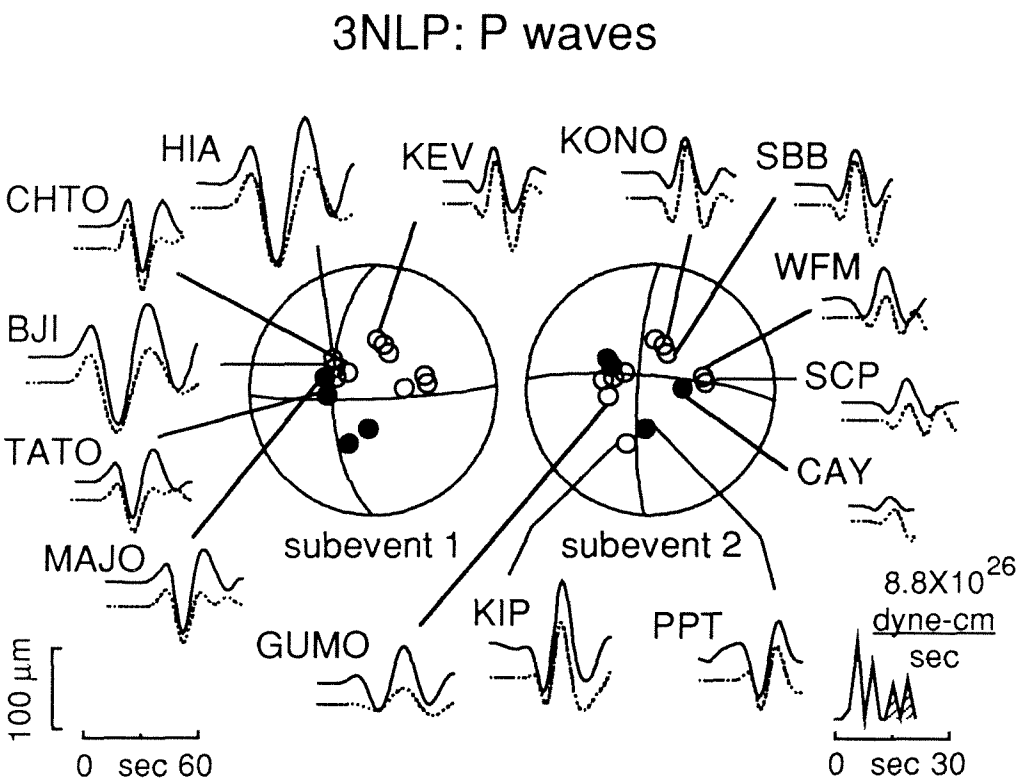

Figure 5.38: 3NLP. Observed (solid line) and synthetic (dashed lines) LP P-wave seismograms. Shown in the center of the figure is the lower hemisphere focal mechanism for the two subevents. Solid circles represent compressional, and open circles, dilatational first motions. Source parameters are given in Table 5.10. The combined source time function for 3NLP.1 (unhatched) and 3NLP.2 (hatched) is shown at bottom right. Time and amplitude scales are shown at bottom left. Amplitudes of the observed and synthetic seismograms are normalized to the identical instrument at a distance of 60° with a peak magnification of 1.

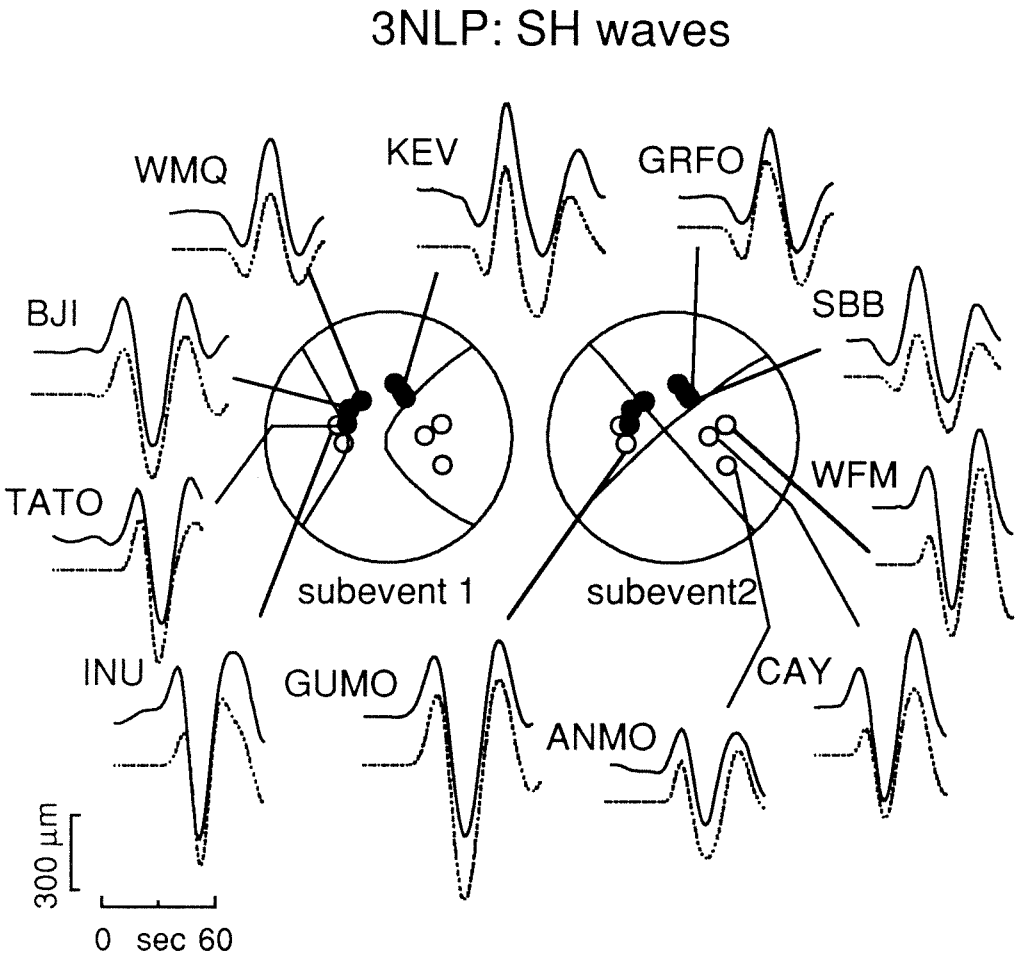

Figure 5.39: 3NLP. Observed (solid line) and synthetic (dashed lines) LP SH-wave seismograms. Symbols are described in Figure 5.38.

42 km from the epicenter at an azimuth of 268°, and has a fairly smooth source time function. Total moment release for this model is 4.4×10^{27} dyne-cm. See Table 5.10.

The LP and WWS data are also modeled using method K. The fault plane dimensions are comparable to those investigated with method N. Moment release along both a north-south and east-west trend is investigated. For the north-south trend, the fault plane extends 110 km to the north and 20 km to the south. For the east-west trend, the fault plane extends 60 km to the west and 10 km to the east. For the LP data, inversion for a single source constrains the total duration to be approximately 20 sec, where $\tau_r = 4$ sec and $\tau_d = 16$ sec (Figure 5.42). This duration is in good agreement with previous results. The source lies at a depth of 10 km and is located at the epicenter. The focal mechanism is similar to the first motion and CMT solution but has a much shallower dip (strike 179°, dip 59°, rake 178°). The model does a good job of modeling the waveform shape, but not the amplitudes. As illustrated in Figure 5.43b, the amplitude of the synthetics for station MAJO is only 40% of the amplitude of the data. An additional iteration improves the amplitude match by adding a small normal event at 6 sec, but does not match the rise time in the data (Figure 5.43c).

Systematic variation of the time function showed that the source element that best matches the rise times in the data had $\tau_r = \tau_d = 2$ sec. For the LP data, the north-south fault plane resulted in the lowest overall errors. Figure 5.43d shows the results for one iteration. Figure 5.44 contours the correlation functions and the corresponding, best-fit focal mechanisms. The diagram indicates that this is a

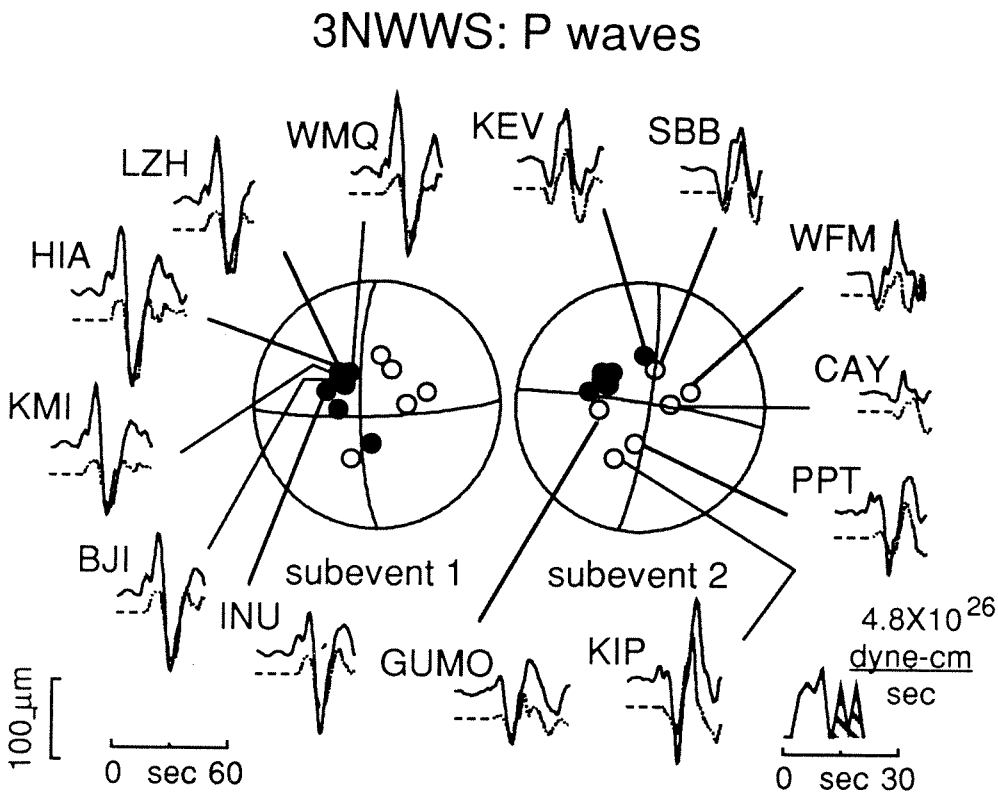

Figure 5.40: 3NWWS. Observed (solid line) and synthetic (dashed lines) WWS P-wave seismograms. Symbols are described in Figure 5.38.

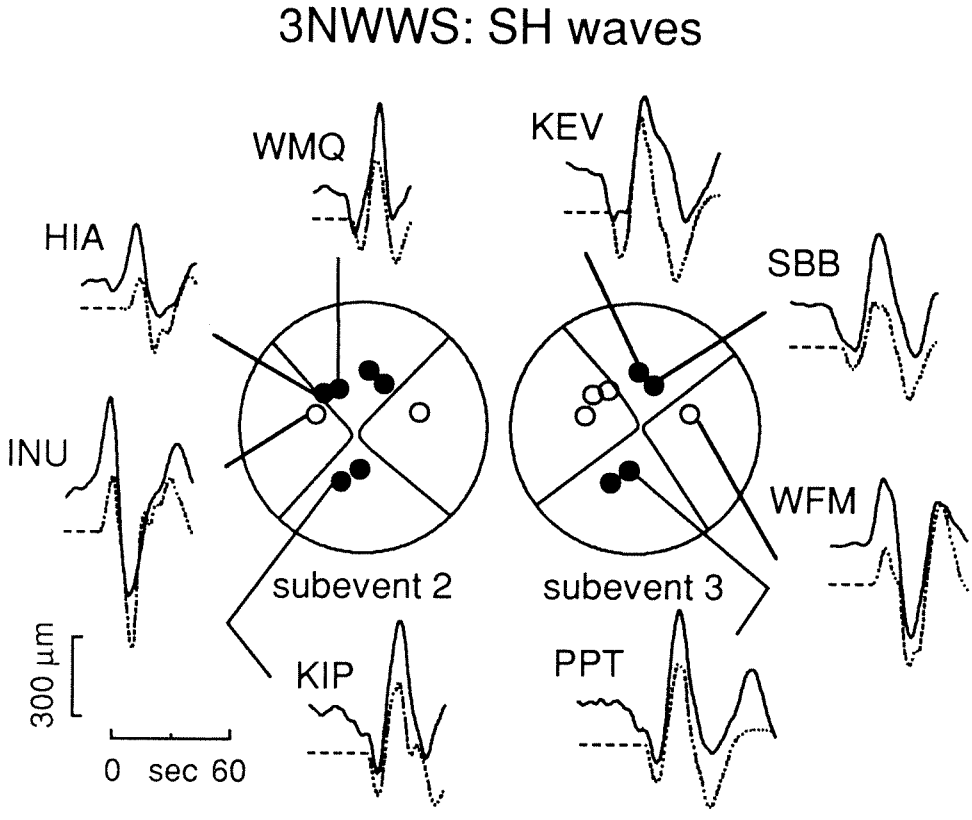

Figure 5.41: 3NWWS. Observed (solid line) and synthetic (dashed lines) WWS SH-wave seismograms. Symbols are described in Figure 5.38.

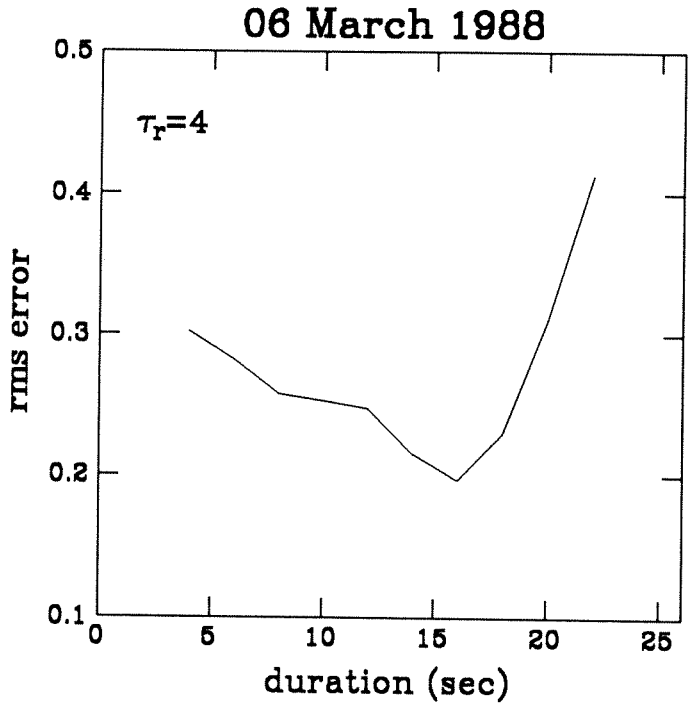

Figure 5.42: Data misfits for the LP data in method K. Plotted is the error versus τ_d of the single best-fitting trapezoidal source function where $\tau_r = 4$.

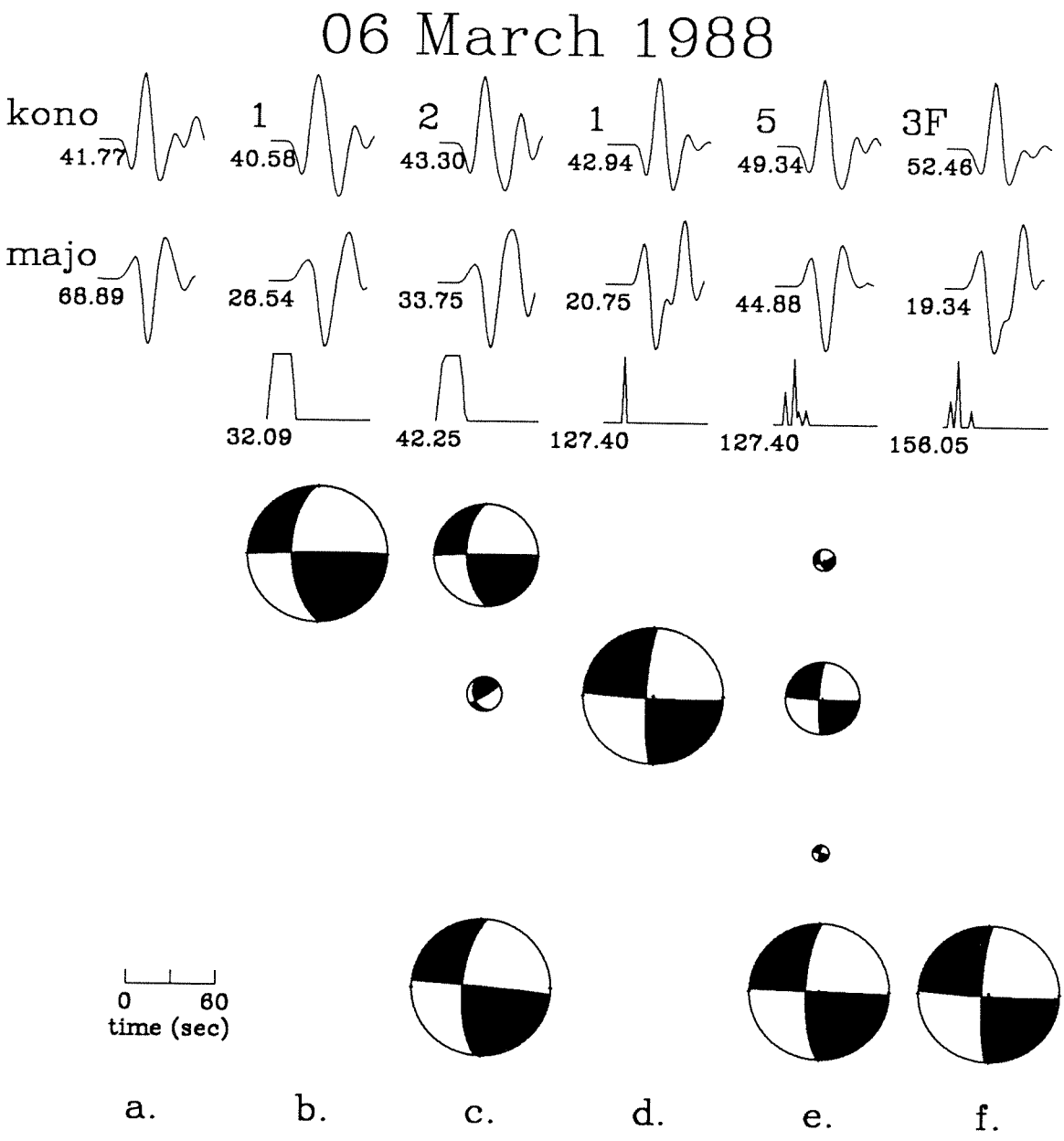

Figure 5.43: Layout is described in Figure 5.13. Shown are: a. data for stations KONO and MAJO; synthetics for models with time varying focal mechanisms and $\tau_r = 4$ and $\tau_d = 16$ for b. 1 and c. 2 iterations, and $\tau_r = \tau_d = 2$ sec for d. 1, and e. 5 iterations; and f. synthetics for a fixed focal mechanism and $\tau_r = \tau_d = 2$ for 3 iterations.

relatively simple event with a focal mechanism that remains stable along the strike of the fault plane during the first 15 sec of the event. After that, the mechanism changes rapidly. The initial subevent is well constrained by the correlation functions to occur at 8 sec.

Model 3KLP allows the focal mechanism to vary in time for 5 iterations. Focal mechanisms for the three largest subevents, 3KLP.1, 3KLP.2 and 3KPL.3, along with the best double-couple sum of the 5 subevents are shown in Figure 5.43e. All subevents have consistently right-lateral, strike-slip mechanisms on the north-south trending plane.

Figures 5.45 and 5.46 show the data and synthetics for model 3KLP. The focal mechanism shown and given in Table 5.10 is the best double-couple sum of the 5 subevents comprising the solution. The SH-wave amplitudes are well matched and so are the P-wave amplitudes for the northern stations. However, amplitudes of the P-wave synthetics for the remainder of the stations are consistently low with respect to the data. Beyond 5 iterations, the amplitude match and overall solution improve, but slowly. Additional subevents have little moment and hence, do not have a significant effect on the solution.

Waveform matches for stations CAY and SCP are also not good. The P-wave first arrivals for both stations have the wrong polarity. In the solution, both stations lie near P-wave nodes for most of the subevents. The low amplitude of the data indicates that CAY is nodal and therefore, does not carry much weight in the inversion. However, in model 3NLP, both SCP and CAY are quite well matched (Figure 5.38). The difference between models 3NLP and 3KLP can be attributed to

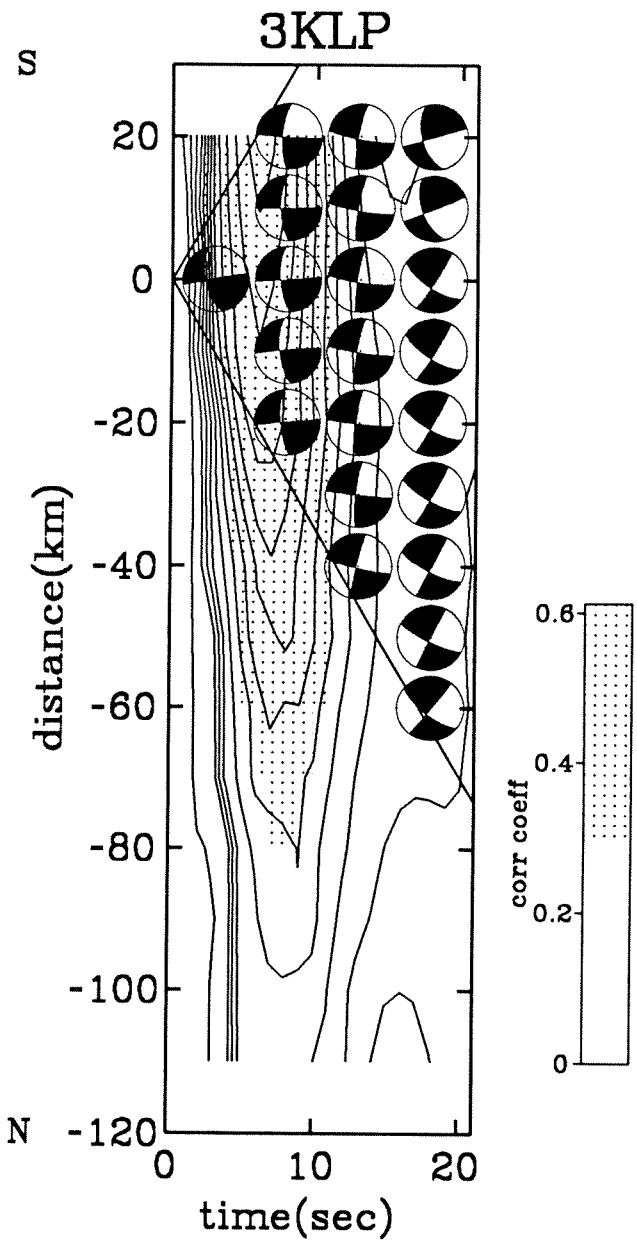

Figure 5.44: 3KLP. Layout is described in Figure 5.14.

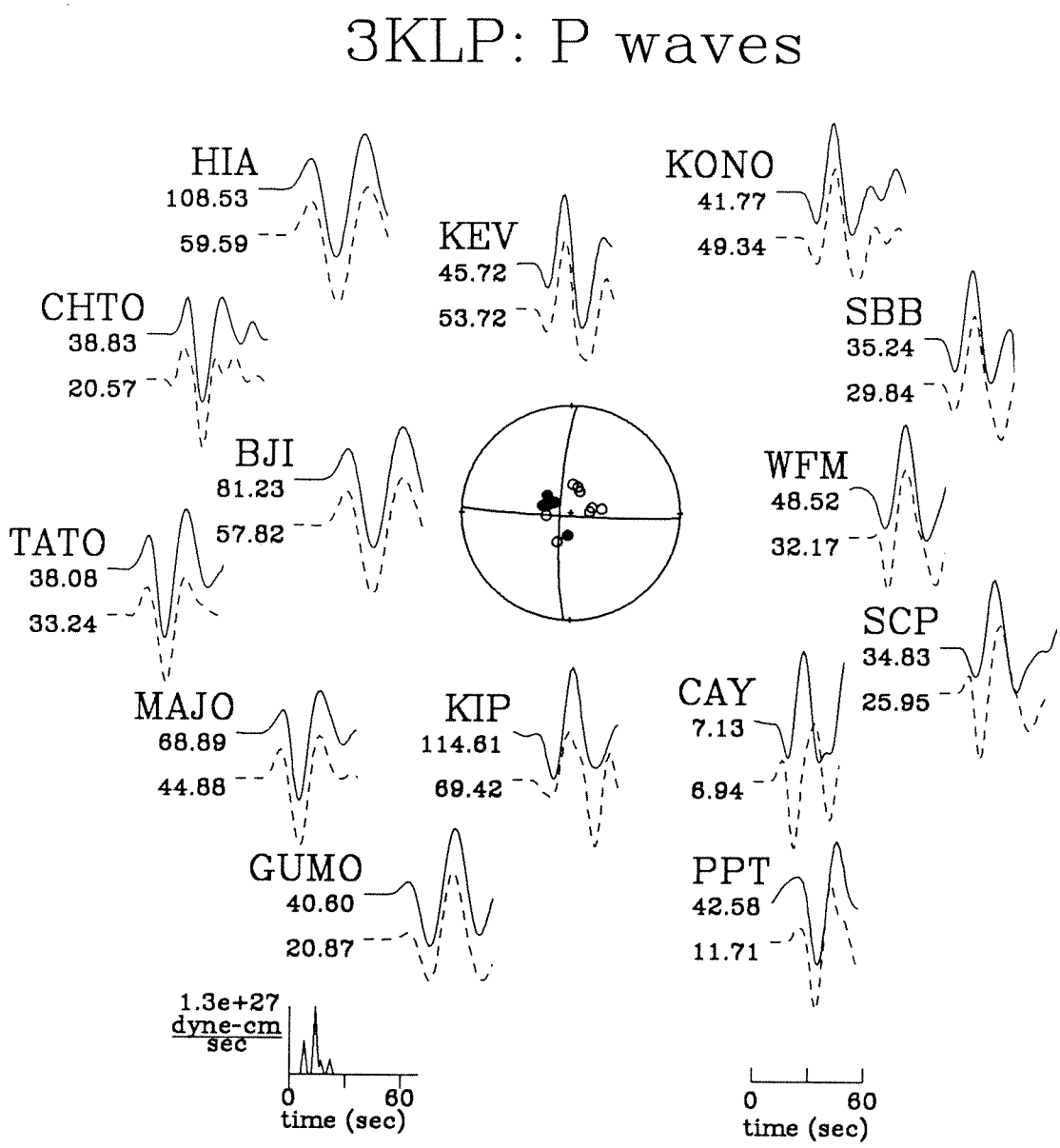

Figure 5.45: 3KLP. Observed (solid line) and synthetic (dashed lines) LP P-wave seismograms. Source parameters are given in Table 5.10. Symbols are described in Figure 5.15.

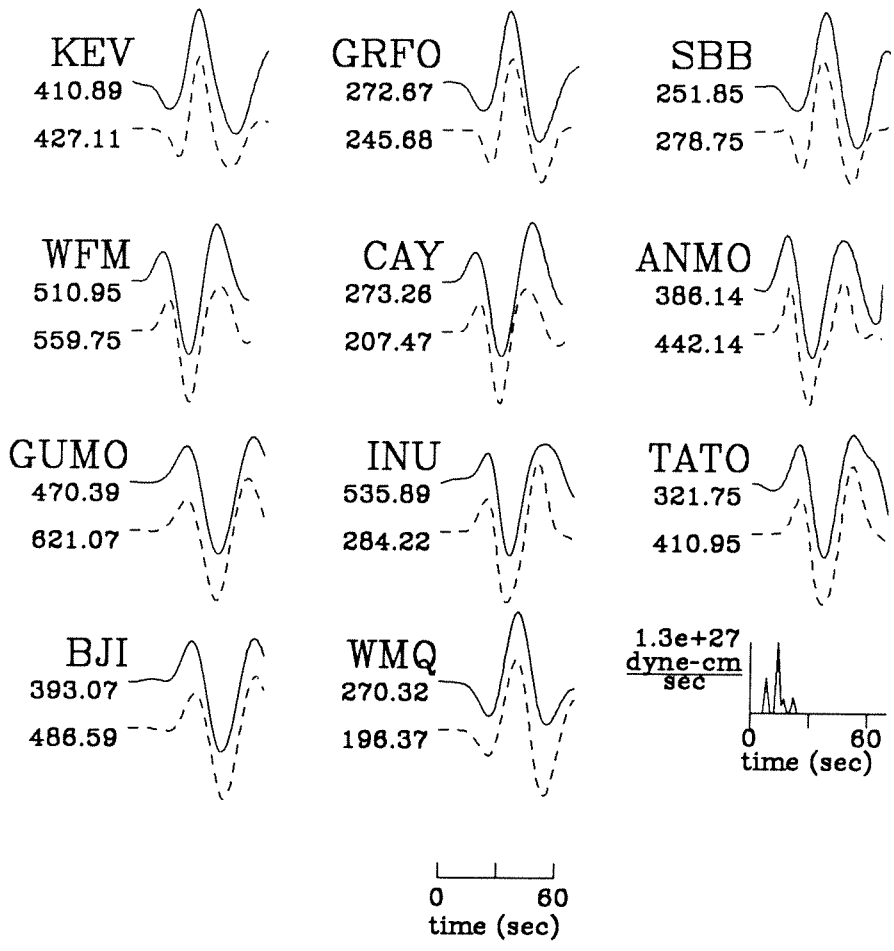

Figure 5.46: 3KLP. Observed (solid line) and synthetic (dashed lines) LP SH-wave seismograms. Source parameters are given in Table 5.10. Symbols are described in Figure 5.15.

differences in the two inversion methods. Method N smooths the solution over the time of the subevent. Hence, the focal mechanism and the source-time function are averaged properties. On the other hand, method K inverts for each source element independently without any constraints. For this data set, the averaging properties of method N help to constrain the solution so that both the first motions and the timing of the main pulse appear to be correct. Note that this cannot be attributed to the different timing used in the final models. Both models start out with the same timing. In the final models, both CAY and SCP in 3KLP are shifted $\delta t = -3$ sec with respect to model 3NLP. Identical timing of the waveforms results in worst matches.

In model 3KLP, most of the moment release occurs at a depth of 20 km and within a distance of 20 km of the epicenter. Only one subevent accounting for a little over 10% of the total moment occurred at a greater distance — 40 km to the north. The best double-couple sum has a scalar moment of 3.9×10^{27} dyne-cm with a very small nondouble-couple component (<1%).

This solution and its correlation functions indicate that a single mechanism should be able to explain most of the data. In Figure 5.43f, the focal mechanism for each subevent is held fixed to that of the largest subevent in 3KLP for 3 iterations. The source-time function for the fixed focal mechanism model matches model 3KLP, and its synthetics explain the waveform data at many of the stations. The first motions in the synthetics for stations CAY and SCP are now correct. The model, however, fails to match the P-wave amplitudes and waveform shapes at stations CHTO, TATO, and MAJO. The amplitude of the synthetics is approximately 50% of the amplitude

of the data. Subsequent iterations did little to improve the errors in the solution or the waveform matches. In general, the variable focal mechanism model, 3KLP, is a much better overall match to the data.

The WWS data are modeled using a source element of longer duration, τ_r = 2 sec and τ_d = 4 sec. The duration of a simple, triangular source element, $\tau_r = \tau_d$ = 2 sec, is too short to match the data, while a source element of τ_r = 4 sec and τ_d = 16 sec is too long. Again, both north-south and east-west trending fault planes are investigated. The fault plane of the preferred model, model 3KWWS, trends east-west. The correlation functions and their corresponding best-fit focal mechanisms are similar to the LP results (Figure 5.47). Within a distance of 20 km of the epicenter, the focal mechanisms are nearly identical during the first 15 sec of the event. Outside this region, the mechanism either rotates or becomes opposite to the best correlated mechanism. As before, even though this appears to be a simple event, a single focal mechanism cannot explain the data.

In model 3KWWS, the focal mechanisms are allowed to vary in time for 5 iterations. Figures 5.48 and 5.49 show the data and synthetics for this model. The focal mechanism shown and given in Table 5.10 is the best double-couple sum of the 5 subevents comprising the solution. The overall match to the waveforms is good, but the amplitudes are underpredicted. For this model, most of the moment release lies within a depth of 10 to 20 km and within a distance of 20 km from the epicenter. The focal mechanisms for the different subevents in the first 10 sec are consistently left-lateral strike-slip on the east-west trending plane with the focal parameters varying up to 10°. The best double-couple sum has a scalar moment of 4.3×10^{27} dyne-cm

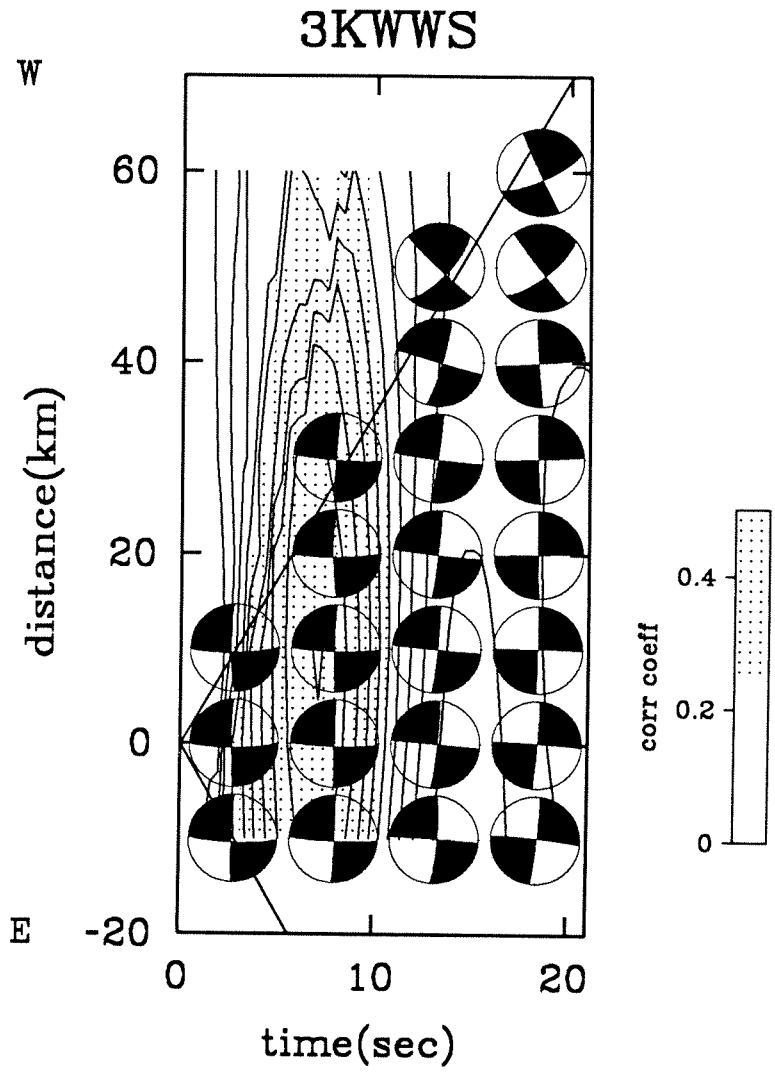

Figure 5.47: 3KWWS. Layout is described in Figure 5.14.

with a large nondouble-couple component of 21%.

The last iteration in the solution introduces the large nondouble-couple component. It improves the errors by 7% from the previous step and noticeably improves the waveforms. This subevent occurs late at 18 sec and has a normal mechanism that is not well resolved. Without it, the best scalar moment remains almost the same, 4.4×10^{27} dyne-cm, but now has a very small, nondouble-couple component, <1%.

Table 5.10 summarizes these models. Event 3 consisted of multiple strike-slip subevents at centroid depths between 10–20 km with varying focal mechanisms. Figure 5.50 shows a spatial comparison of along strike moment release between the models. As illustrated previously, most of the moment release occurs between 6–12 sec and lies in the epicentral region within a radius of 30 km. Total moment release corresponds to an $M_w = 7.7$.

Estimates of the focal parameters differ by $\pm 10°$ for the different models and from the first motion and CMT solution, but all agree within the errors of their respective models. The first motion solution strikes about 10° counterclockwise from the majority of the models. A near north-south strike similar to the above models with a near vertical dip is also allowed by the first motion data. In all of these models, the orientation of the focal mechanisms appears to rotate clockwise with time, contributing to the nondouble-couple component also observed in the CMT solution (Dziewonski *et al.*, 1989b).

Since the epicenter of this event lies at the junction of both a westerly and northerly seismicity trend, the choice of fault planes is ambiguous. Most of the

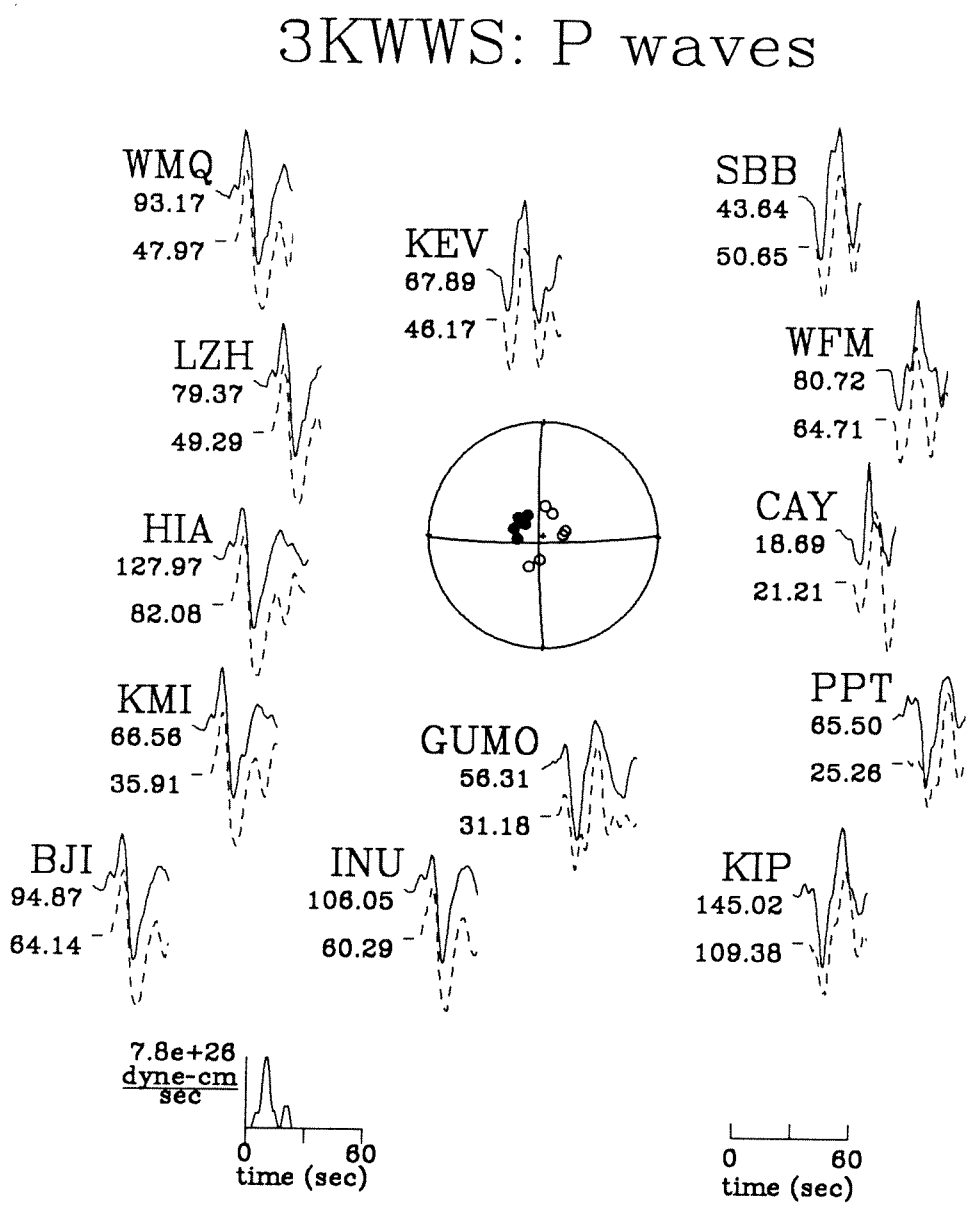

Figure 5.48: 3KWWS. Observed (solid line) and synthetic (dashed lines) WWS P-wave seismograms. Source parameters are given in Table 5.10. Symbols are described in Figure 5.15.

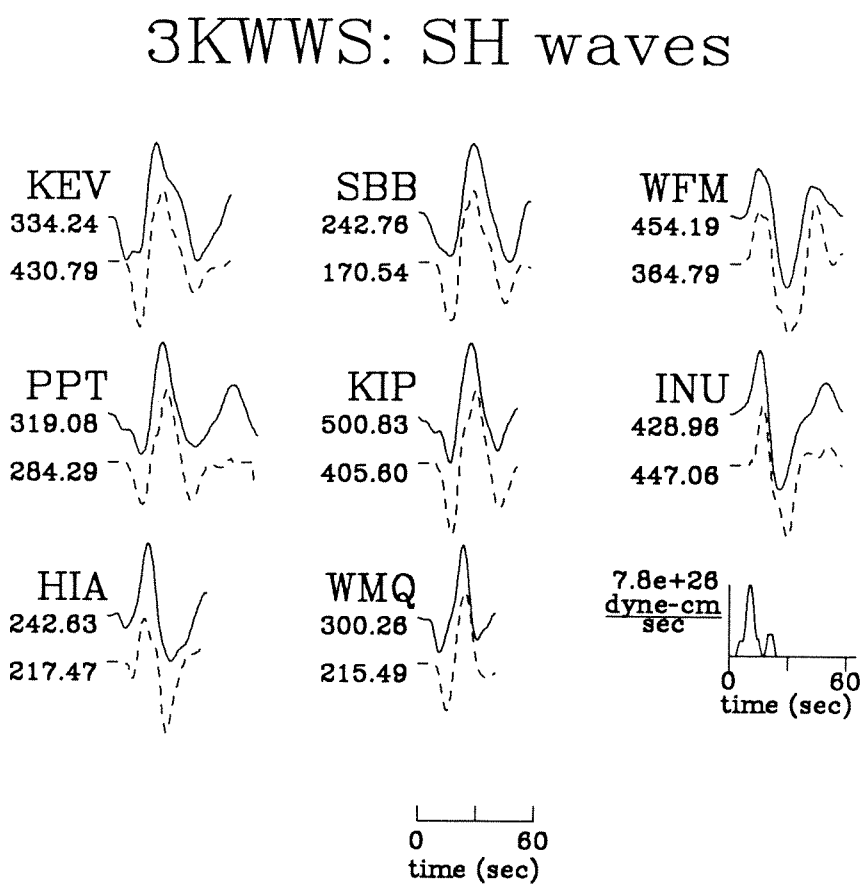

Figure 5.49: 3KWWS. Observed (solid line) and synthetic (dashed lines) WWS SH-wave seismograms. Source parameters are given in Table 5.10. Symbols are described in Figure 5.15.

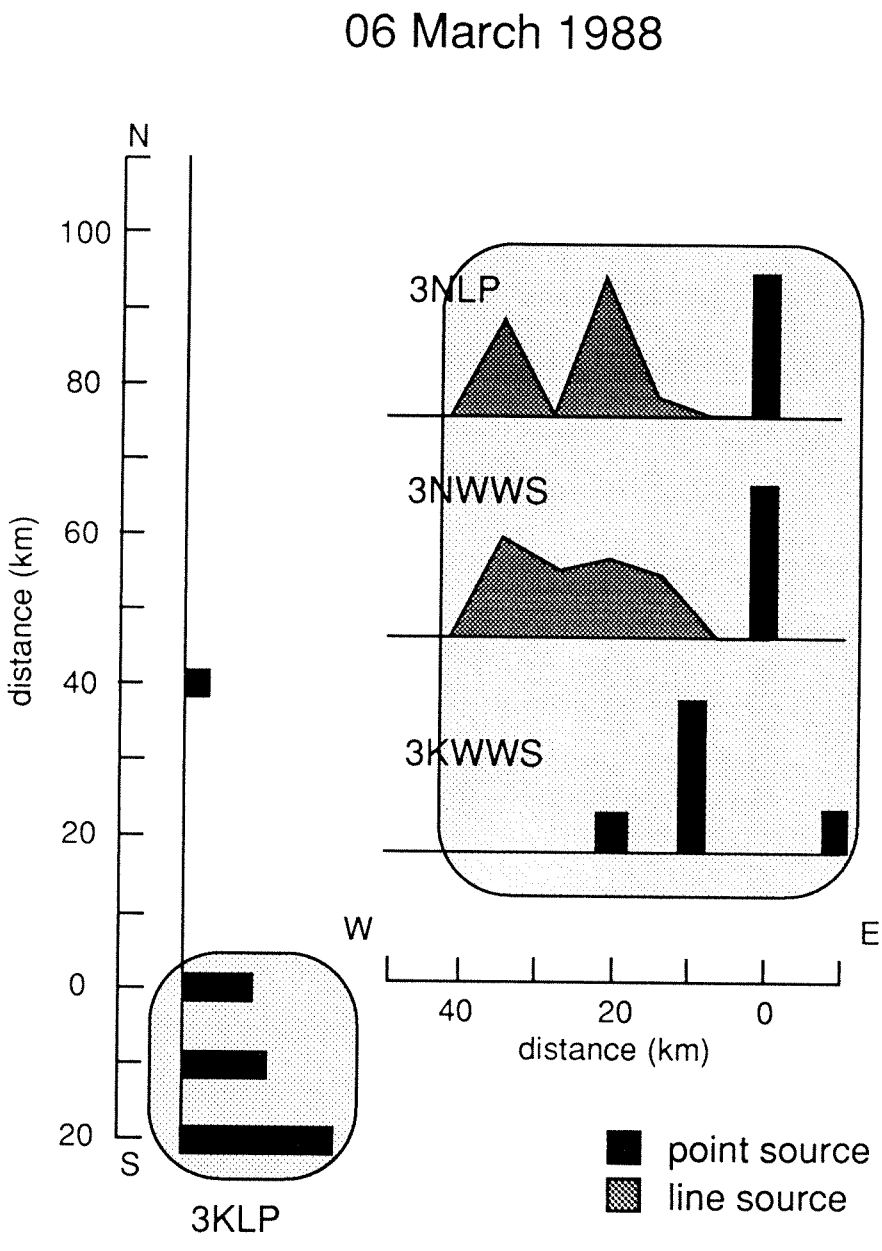

Figure 5.50: Event 3. Symbols are described in Figure 5.20.

seismicity lies along the northerly trend, arguing for the north-south trending nodal plane as the fault plane. However, the majority of the models also suggest that some moment release is associated with the westerly trend. Hence, both trends may have been active during this event.

5.6 Comparison of Methods and Trade-offs

Two different methods, N and K, are used to analyze the data from the Gulf of Alaska earthquakes. The differences between model sets N and K for each event can be largely attributed to how the two methods average the source and how subevents trade off with one another. In both methods, source properties are averaged over the time window of each subevent. For each subevent, the results give the centroid location and focal mechanism over its duration. The modeling in this chapter illustrates the effects of, and trade-offs between, source duration and focal parameters.

In method K, the average source properties of the event are first found from the best-fitting single source. As the duration of this source decreases, positions of the source and focal parameters change. This is illustrated below using results from the LP modeling of Event 1. For this event, as the source duration decreases, the largest subevent becomes deeper, the dip along each nodal plane steepens, and the rake increases. The strike remains stable (Figure 5.51). The depth as well as the lateral position of the source changes since longer source elements average over both a longer period of time and hence, a larger fault area. Differences in focal parameters can be caused by averaging source positions and focal mechanisms that do not remain constant over the duration of the source element. The choice of time constants for

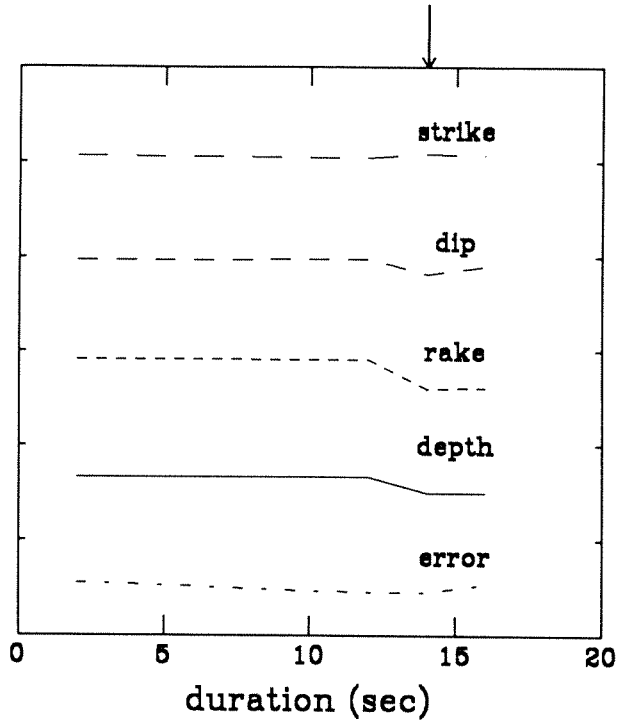

Figure 5.51: Variation of source parameters with duration. Source parameters are normalized to arbitrary levels for display purposes. The arrow marks the duration time of the least error solution.

the source elements is somewhat arbitrary, but is limited on the high end by the duration of the event and on the low end by the high frequency cutoff of the data.

In method N, the source is described by fewer subevents whose positions are either constrained to lie at a point or along a line propagating at a specified rupture velocity. The conditions are more rigid than in method K and result in each subevent averaging over longer time periods and a larger area. This averaging or smoothing

can be desirable since not all of the details in the source are always resolvable. However, for sources that change rapidly in time, it may not result in an accurate picture of the source process. As previously discussed, both time variation in the focal mechanism and in the source positions can alias into the source parameters.

Differences in the models can also be attributed to how the subevents trade-off with one another. In method N, the number of subevents is kept small to limit the trade offs between them. Since the source parameters of each subevent actively interact with one another during the inversion, minimizing the number of free parameters stabilizes the solution. In method K, source parameters of each subevent depend on previous iterations. This problem has been discussed by Young *et al.,* (1989) and Kikuchi and Kanamori (1990) and has been called *path dependence.* Choosing different first subevents or changing the order of iteration changes the iteration path. The new solution can produce divergent but equally valid results. This effect is particularly important for complex events whose correlation functions have maxima with similar values (Young *et al.,* 1989). Event 1 and Event 3 have relatively simple sources whose correlation functions have one well-isolated peak and whose focal mechanisms are stable over a long time window. This suggests that the initial inversion path is stable. On the other hand, the correlation functions for Event 2 have many peaks, suggesting that many different iteration paths can explain the data equally well. Since the focal mechanisms along the secondary peak are left-lateral, which is opposite in sense to the first motion mechanism, and the correlation at the primary peak has a substantially larger amplitude, the first iteration is robust. However, changes in the order of iteration of subsequent subevents may still have some

effect on the final solution.

5.7 Summary of Models

The analyses of the events in this chapter use two data sets, LP and WWS, with different bandwidths to determine the source parameters of each event. The LP instrument response has a narrower bandwidth than the WWS response, and its waveforms appear simpler and are easier to model. However, the narrow, long-period bandwidth limits the resolution of the data. The WWS waveforms, on the other hand, are more complex since they contain a wider range of frequencies that include shorter period signals. This enables more details of the source such as source position and structure of the source-time function to be resolved. For some events using method N, this added resolution helps to distinguish between models.

Using WWS data to model simple events such as Event 1 or Event 3 produces reliable results. For these events, the WWS models can explain most of the waveforms and have solutions that are consistent with the LP models. However, for more complex events such as Event 2, the WWS data cannot be modeled as well as the LP data. The complexity of the waveforms at the higher frequencies cannot be modeled satisfactorily.

The models for each event present similar pictures of the source process. The details of the source process for the different models agree with one another within the errors of the inversion. Features present in all models are the most reliable. These features are summarized below and in Figure 5.52.

Event 1 is the smallest event in the sequence, $M_w = 7.2$. The inferred fault plane

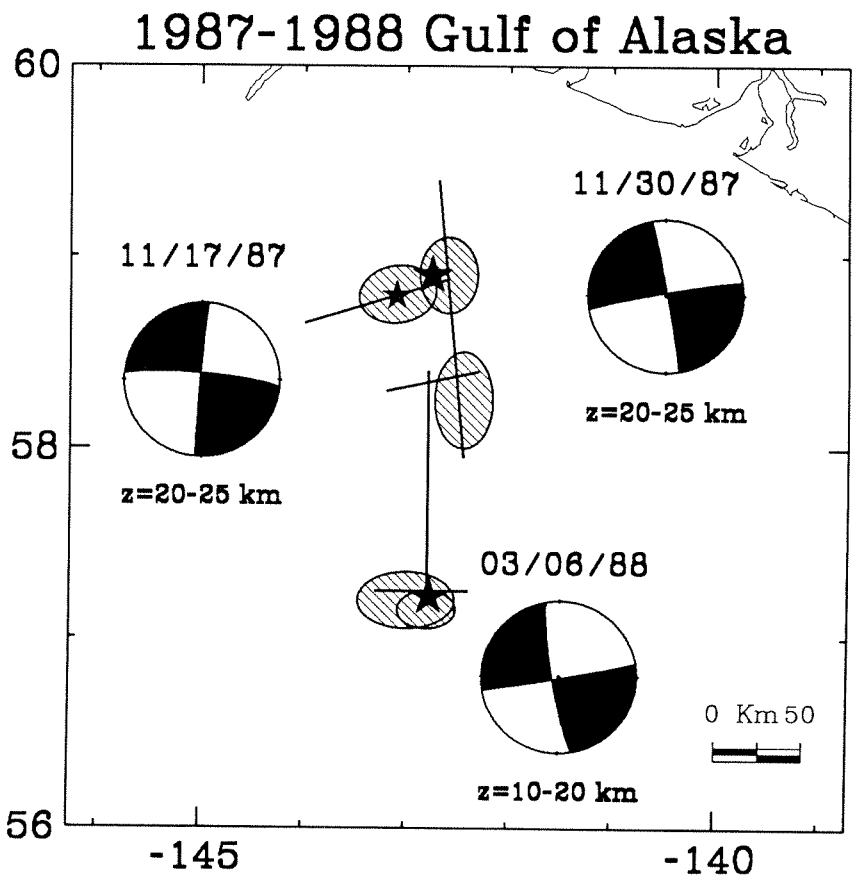

Figure 5.52: Summary of source models for the 1987-88 Gulf of Alaska earthquakes. Lines represent approximate locations of seismic trends (see Figure 5.3). Stars mark the locally determined epicenters. First motion solutions from J. Lahr (personal communication) are also shown. Shaded areas mark the regions of maximum moment release for each event.

is nearly east-west striking with a steep northerly dip. Rupture propagated slowly towards the west at 1 km/sec. Most of the moment release occurred at a depth of 20 km over a fault length of 20 to 40 km. A fault length of 40 km is in good agreement with the rupture length inferred from the aftershock area during the first 24 hr (see Figure 5.4).

Event 2 is the largest and most complicated in the sequence, $M_w = 7.8$. Most of the moment release occurs at a depth of 20 km and is concentrated in two regions. The largest amount of moment release occurs in a region south of the epicenter. Models 2N and 2KLP place most of their moment at 70 and 90 km, respectively, while model 2KWWS distributes the most moment at 40 and 60 km. Additional moment release occurs within 20 km of the epicenter. A total fault length of 110 km is in good agreement with the rupture length inferred from the aftershock area during the first 24 hr (see Figure 5.5).

Event 3 is the second largest in the sequence, $M_w = 7.7$. Moment release lies within 40 km west and 20 km south of the epicenter at a depth of approximately 15 km. Aftershock seismicity suggests that the fault ruptured unilaterally 110 km to the north (see Figure 5.6). However, all models indicate that substantial moment release did not occur north of the epicenter, and the maximum fault length activated was much shorter, approximately 40 km, in the east-west direction.

For the three events, source depth is the best-resolved source parameter. In method N, estimation of source depth is robust and can be resolved within $\Delta z =$ 10 km (Figures 5.7b, 5.22b, and 5.37bd). The difference in depth for each model falls within the errors of the inversions. For Event 1 and Event 2, the centroid depth of

the largest source lies at a depth of z=20–25 km. The third event lies shallower, at a depth of z=10–20 km. These depths are greater than the crustal thickness ($\approx$12 km) and place their centroids in the upper mantle.

All three events have north-south, east-west trending, strike-slip mechanisms. Estimates of the focal parameters for all models are within approximately $\pm 10°$ of a pure vertical, north-south trending strike-slip fault. Modeling using a single focal mechanism could not explain the data for any of the events. For the two simpler events, Event 1 and Event 3, subevents with a single mechanism and a long duration could describe the most prominent features. However, overall duration, amplitude, and timing were substantially better matched when multiple mechanisms were allowed. Since the radiation pattern varies rapidly with azimuth and with change in fault dip for pure, strike-slip type events, even a small change in focal parameters can improve the solution significantly.

For Event 1, the mechanisms of the largest subevent for both 1NLP and 1NWWS agree with each other and with the mechanisms of the largest subevents in 1KLP and 1KWWS. Smaller subevents for models 1KLP and 1KWWS indicate a considerable amount of variability.

The variability in the focal mechanisms for Event 2 indicates the complexity of the source. The largest subevents in models 2K have about $\Delta(\phi, \delta, \lambda) = 10°$ of variability. Focal mechanisms for the largest subevents in models 2N are significantly different from each other and from models 2K, suggesting that models 2N may oversimplify the source. Trade offs that are due to the smoothing of each subevent over time and fault area and the overlap in time between the subevents both affect the results.

The focal mechanisms for Event 3 are consistent with one another. The north-south trending nodal plane dips to the west and the east-west trending plane is near vertical or southerly dipping.

5.8 Discussion

Aftershock seismicity of the Gulf of Alaska earthquakes concentrates primarily in the epicentral regions. For the two largest events and the largest subevent in Event 2, these are regions of apparent structural complexity where east-west and north-south seismicity trends intersect (Figure 5.52). The clustering of seismicity near structural complexities has been observed along other strike-slip faults. Lindh and Boore (1974) noted that the foreshock and mainshock of the 1966 Parkfield-Cholame earthquake lie near a 5° bend in the fault trace. Seismicity concentrated near a step in the fault during the Parkfield aftershock sequence (Eaton *et al.,* 1970) and near fault steps in the Imperial Valley (Johnson and Hadley, 1976; Johnson and Hutton, 1982). The 1987 Superstition Hills earthquake and its aftershocks concentrated at the intersection of two conjugate faults (Magistrale *et al.,* 1989).

Moment release for the Gulf of Alaska events also lies primarily at the intersection of seismicity trends (Figure 5.52). Since the two nodal planes for these subevents have strikes similar to both trends, these subevents cannot always be unambiguously associated with either trend. The epicenter for Event 2 lies at the intersection of an east-west seismicity trend defined by the aftershock sequence of Event 1, and its own north-south trending aftershocks. This suggests that for Event 2, moment release near the epicenter lies along the north-south trend. Moment release to the south of

the epicenter lies near the intersection of the north-south trend and another east-west aftershock trend. Placement of moment release along the east-west trend is within the errors of the inversions. The apparent right-lateral offset of the north-south seismicity trend by the east-west trend is opposite in sense to the focal mechanism solution, but the offset may be unrelated to current activity. An east-west trending rupture with a small lateral extent is also preferred by most models for Event 3, even though the aftershocks lie along a predominantly north-south trend approximately 110 km in length.

In plan view, regions of large moment release for the Gulf of Alaska earthquakes appear to correspond to regions of high aftershock seismicity. This apparent relationship between moment release and aftershock seismicity contradicts observations by other authors. Comparing slip distribution along a two-dimensional fault plane as determined from inversions of strong-motion data to cross sections of aftershock seismicity, several authors have observed that regions of high aftershock seismicity along the fault plane tend to occur outside regions of large slip (Doser and Kanamori, 1986; Hartzell and Heaton, 1986; Wald *et al.,* 1990). This phenomenon has also been observed with teleseismic data where regions of high moment release have the fewest aftershocks (Schwartz *et al.,* 1989, Hwang *et al.,* 1990). Since aftershock depths for the Gulf of Alaska earthquakes are undetermined, the aftershock zone and the mainshock rupture zone possibly have different depths. In this case, the relationship between moment release and aftershock seismicity for the Gulf of Alaska events would be similar to that observed for other events.

Intraplate seismicity tends to occur on pre-existing weak zones (Sykes, 1978).

Seismicity patterns for the Gulf of Alaska earthquakes correlate with the pattern of magnetic lineations (Figure 5.2) suggesting, that aftershock seismicity may be following pre-existing zones of weakness in the crust (Lahr *et al.*, 1988). A similar relationship has also been observed in the southeastern corner of the Gorda plate (Wilson, 1986). For the Gulf of Alaska sequence, seismicity approximately follows the axis of magnetic anomaly 13. Aftershock seismicity lies north of a magnetic discontinuity at approximately 57° (Atwater and Severinghaus, 1989). Neither the right-lateral offset of seismicity seen in the data nor any other east-west trending features are observed in the magnetics.

While the seismicity patterns are controlled by pre-existing weaknesses in the crust, the style of faulting is controlled by the regional stresses. Strike-slip faulting indicates near horizontal PT axes. As suggested by Lahr *et al.* (1988), this can occur in between locked and recently slipped zones of the subducting plate (Figure 5.53). The orientation of the T-axes nearly perpendicular to the axis of the Aleutian trench suggests that the Pacific plate is accommodating tensional stresses induced by the 1964 Great Alaskan earthquake. Compressive horizontal stresses along the northern margin are high because of oblique convergence and subduction of the buoyant Yakutat terrane. The orientation of the PT axes for the Gulf of Alaska earthquakes is consistent with this interpretation.

The hypocenters of these events suggest that faulting extended to at least a depth of 25 km. A seismogenic depth of 25 km is deeper than seen for most strike-slip earthquakes. Seismicity for two large San Andreas earthquakes, the 1986 North Palm Springs, M_s=6.0, and the 1989 Loma Prieta earthquake, M_s=7.1, (Given, 1986;

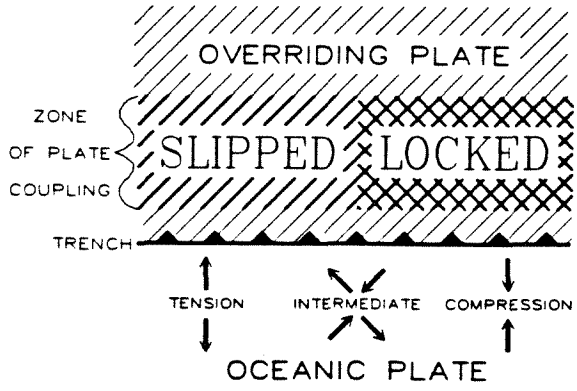

Figure 5.53: Model of stress orientation in an oceanic plate seaward of a plate boundary. Direction of PT axes depends on the state of stress along the boundary. T-axes normal to the boundary reflect tensional stress that is due to recent slippage ("slab pull") while P-axes normal to the boundary reflect compressional stress that is due to a locked boundary. Intermediate stresses occur at the boundary of the locked and slipped zones (from Lahr *et al.* (1988)).

Dietz and Ellsworth, 1990) do extend to depths of 20 km, but both mechanisms have appreciable dip-slip components (Jones *et al.,* 1986; Kanamori and Satake, 1990). More commonly, the seismogenic depth of strike-slip faults in California is approximately 10 km and no deeper than 15 km. For the Gulf of Alaska earthquakes, a depth of 25 km does, however, agree with previous studies of oceanic intraplate seismicity. Wiens and Stein (1983, 1984) observed that the maximum depth of seismicity deepens with increasing lithospheric age and appears to be bounded by the 700°–800°C isotherm. Isotherms derived from a standard plate cooling model (Parsons and Sclater, 1977) suggest that for a crustal age of 35 My in the Gulf of Alaska (Atwater and Severinghaus, 1989), the maximum depth of seismicity is

approximately 30 km (Figure 5.54). The difference in depth reflects the rheological differences between oceanic and continental crust.

To estimate slip and stress drop along the fault, estimates of the fault parameters such as length, l, and width, w, are needed. These parameters are usually estimated from the aftershock distributions. For Event 1 and Event 2, aftershock lengths are in good agreement with fault lengths derived from rupture models. Event 3, however, has an aftershock length much longer than that derived from rupture models. Below, l is assumed to be equivalent to the aftershock lengths for Event 1 and Event 2, but both aftershock length and modeled rupture length are used to bound estimates of slip and stress drop for Event 3.

Fault width is more difficult to estimate since aftershock depths for these events were not determined. Assuming an l/w aspect ratio of 2 would place the largest events well into the upper mantle at depths of 50–70 km. However, the studies of Wiens and Stein (1983, 1984) suggest that seismicity in the region would not extend below 30 km. GLORIA images from the region also indicate that rupture did not reach the surface (Bruns *et al.,* 1989). Hence, the fault width is probably less than 30 km. Here, the fault width is assumed to be approximately 25 km.

Slip is calculated from

$$u = \frac{\mathrm{M_o}}{\mu l w},$$

where $\mathrm{M_o}$ is moment, μ is rigidity, l is fault length, and w is fault width. Stress drop for a long-shallow, strike-slip fault is given by Knopoff (1958) as

$$\Delta\sigma = \frac{(2\mu\bar{u})}{(\pi w)},$$

where $\bar{u}$ is the average dislocation. Rigidity and fault width are assumed to be

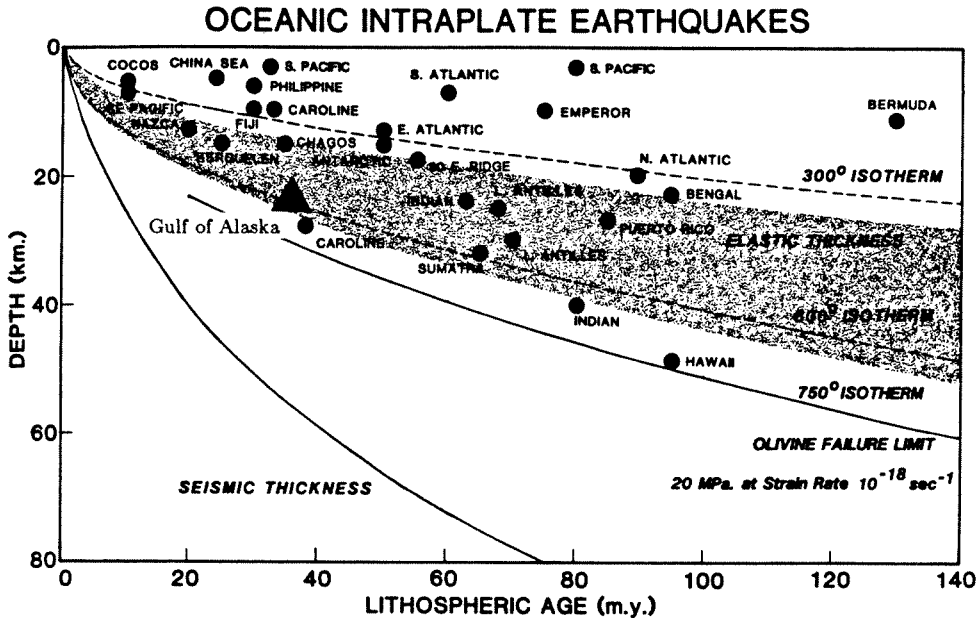

Figure 5.54: Intraplate earthquake depths are shown on a depth-age plot of the ocean lithosphere. Isotherms are calculated from a standard lithospheric cooling model (Parsons and Sclater, 1977). Stippled region denotes the range of estimates of the flexural elastic thickness (Watts *et al.*, 1980). Seismic thickness is taken from Rayleigh wave dispersion data by Leeds *et al.* (1974). The failure limit is the lower limit at which 20 MPa deviatoric stress can be sustained, calculated for a dry olivine rheology (Goetze and Evans, 1979) and a strain rate of 10^{-18}/sec. After Wiens and Stein (1983).

4.2×10^{11} dyne/cm^2 and 25 km, respectively. For Event 1, assuming that l =40 km and $M_o = 7 \times 10^{26}$ dyne-cm, then u = 1.7 m and $\Delta\sigma$ = 18 bars. For Event 2, assuming that l = 140 km and $M_o = 7 \times 10^{27}$ dyne-cm, then u = 4.8 m and $\Delta\sigma$ = 51 bars. For Event 3, an aftershock length of l = 110 km and $M_o = 4 \times 10^{27}$ dyne-cm gives u = 3.5 m and $\Delta\sigma$ = 37 bars. Assuming a much shorter fault length of l = 40 km, then u = 9.5 m and $\Delta\sigma$ = 102 bars.

A stress drop of 102 bars for Event 3 is high with respect to the stress drop estimated for Event 1 and Event 2. However, within the errors of the data, both estimates of stress drops for Event 3 and the estimate for Event 2 are consistent with other intraplate events, while the stress drop for Event 1 is more similar to interplate events (Kanamori and Anderson, 1975). Stress drop varies by up to a factor of 5 between these events.

Source spectra for the events are calculated between the periods of 1 to 20 sec from broadband, short, and intermediate period GDSN and GEOSCOPE records using the method of Houston and Kanamori (1986). The spectrum is corrected for instrument response, geometrical spreading, radiation pattern, and the free-surface receiver effect. The density and P-wave velocity within the crust is taken here to be 2.8 gm/cm^3 and 6.5 km/sec, respectively. The attenuation is corrected, assuming $t^* = 0.7$ sec.

The calculation of the radiation pattern factor for strike-slip earthquakes is not straightforward. For strike-slip earthquakes, many stations lie near nodes. This tends to lower the average amplitude of the radiation factor in comparison to other focal mechanisms. Energy from near source scattering, which radiates away from

the source at similar take off angles as the P-wave, may also increase the overall amplitude of the waveform, especially at nodal stations. Hence, the actual source-station geometry is not used to calculate the radiation pattern factor. Instead, the value of the radiation pattern factor for each station is averaged over the focal sphere for a range of take off angles from 0° to 50° (see Zhuo and Kanamori, 1987).

The average moment rate spectra shown in Figure 5.55 are calculated from 16, 15, and 11 records for the 3 events, respectively, and are shown along with the theoretical spectra for an ω^{-2} model. For Event 1 (Figure 5.55a), the spectral level drops sharply below 0.2 hz. A similar but not as sharp a drop is seen in the spectra for Event 2 below 0.1 hz (Figure 5.55b). Event 3 does not show such a spectral drop.

All three spectra have spectral levels higher than predicted by the ω^{-2} model. As discussed above, a radiation pattern factor that underestimates the true P-wave radiation pattern will overestimate the amplitude of the source spectra. Houston (1990) also tried to correct for strike-slip radiation pattern effects for the 1989 Macquarie Ridge earthquake but spectral amplitudes were still 2 to 3 times higher than were seen for similar thrust events along subduction zones. The high amplitudes for the Gulf of Alaska events, however, do agree with observations of other intraplate earthquakes. Zhuo and Kanamori (1987) observed that at periods of 1 and 2 sec, the average spectral amplitudes of intraplate events are 2 to 4 times larger than those of subduction-zone events with the same M_w, and are roughly equivalent at 5 and 10 sec. Compared to the average subduction zone event, spectral amplitudes for the Gulf of Alaska events are up to 6 times higher at these frequencies. This comparison

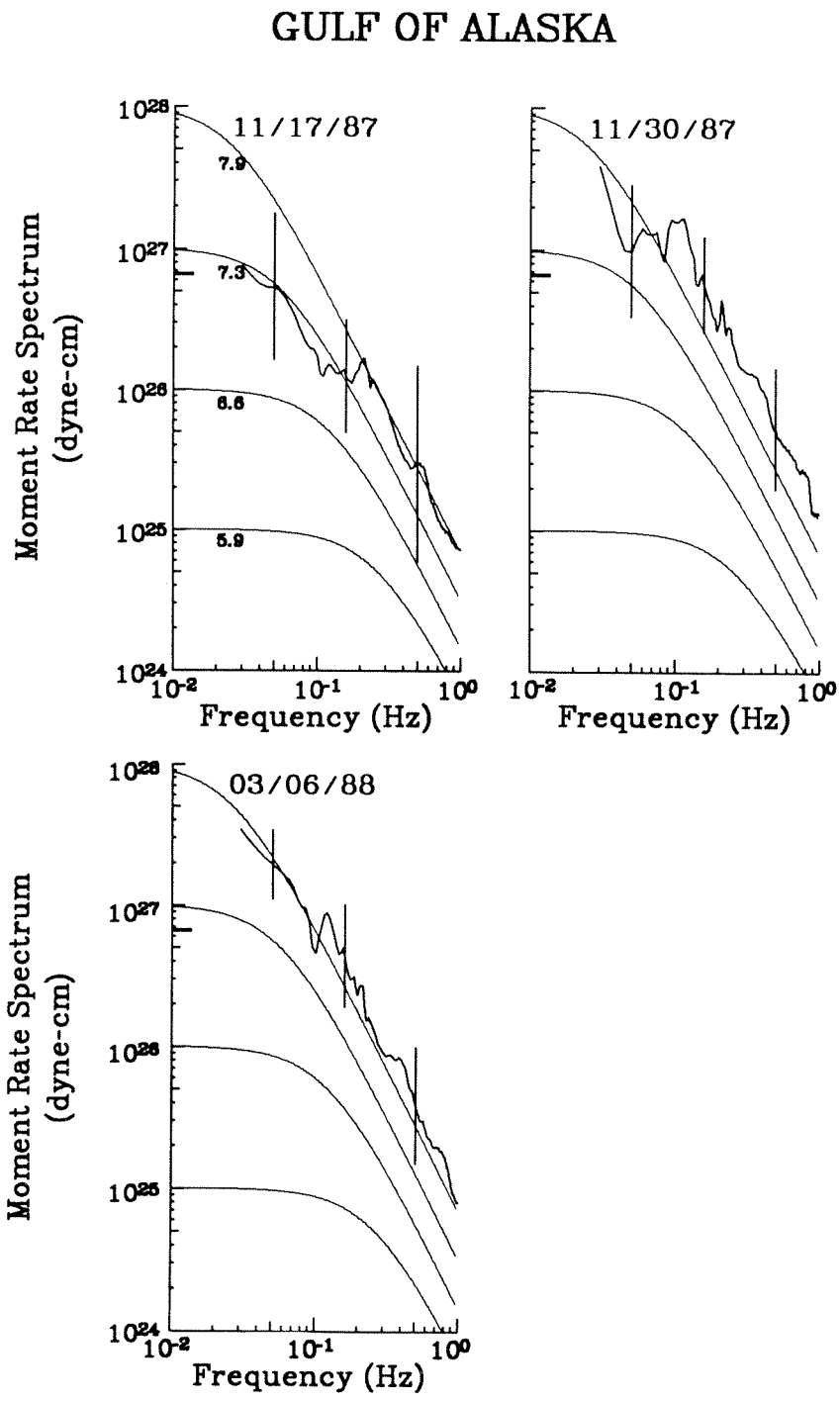

Figure 5.55: Average moment rate spectra for the a. 17 November 1987, b. 30 November 1987, and c. 6 March 1988 earthquakes. Theoretical spectra for an ω^{-2} model are shown with thin lines. The vertical bars show the standard deviation at selected frequencies.

is not robust since Zhuo and Kanamori (1987) did not include strike-slip earthquakes in their analysis.

In comparison to thrust and normal faulting events, these strike-slip events have short durations. Figure 5.56 plots seismic moment versus source process time for several large earthquakes. Circles representing thrust and normal faulting events fall along an empirical relation found by Furumoto and Nakanishi (1983) with moment proportional to the cube of the source process time. Triangles represent 4 large strike-slip events, Event 2 (τ = 36 sec, $M_o = 7 \times 10^{27}$ dyne-cm), Event 3 (τ = 20 sec, $M_o = 4 \times 10^{27}$ dyne-cm), the 1989 Macquarie Ridge earthquake (τ = 30 sec, $M_o = 1.6 \times 10^{28}$ dyne-cm) (Satake and Kanamori, 1990), and the 1976 Guatemala earthquake (τ = 90 sec, $M_o = 2.6 \times 10^{27}$ dyne-cm) (Kanamori and Stewart, 1978; Kikuchi and Kanamori, 1990).

The Guatemala earthquake falls within the scatter for normal and thrust faulting events. The remainder of the strike-slip events form a separate group whose source process times are much shorter, implying shorter rupture lengths. Rupture lengths for these events are indeed shorter than what is observed for most strike-slip events. These earthquakes, the Gulf of Alaska and the Macquarie Ridge earthquakes, are also large events occurring in oceanic environments. Centroid depths below the Moho indicate that these events ruptured into the upper mantle. The above suggests that oceanic lithosphere has a higher strength than continental lithosphere and results in events with larger moment release per unit area than similar continental events.

The Northern Gulf of Alaska is tectonically very similar to the Izu Peninsula, Japan. Both the Northern Gulf of Alaska and the Izu Peninsula represent active ac-

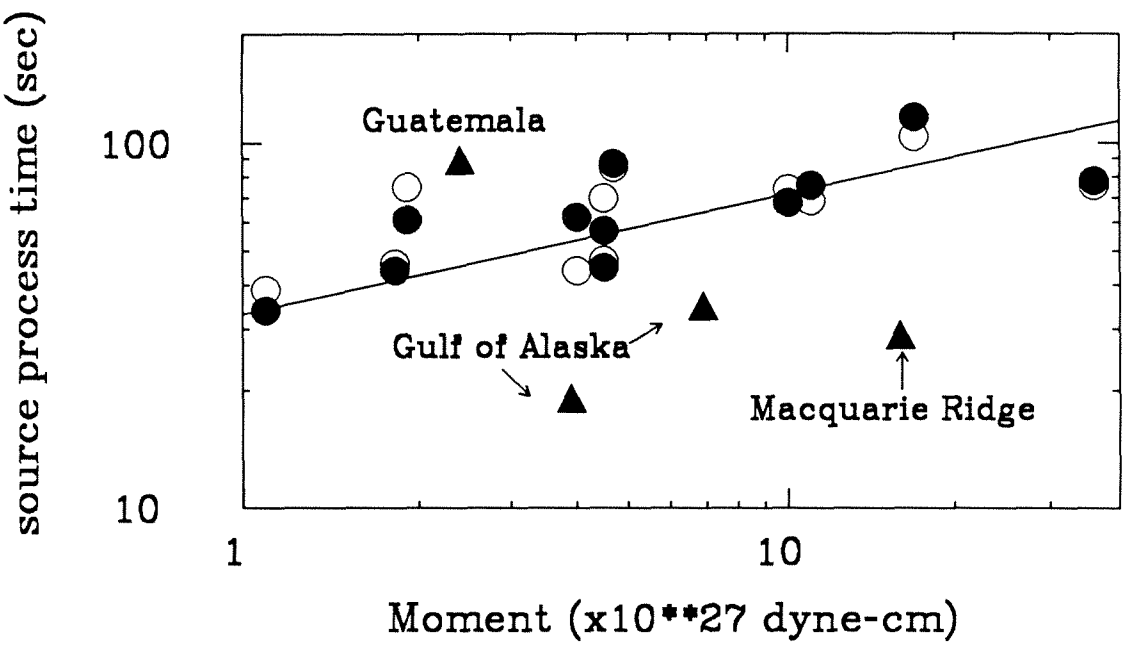

Figure 5.56: Relation between seismic moment and source process time for normal and reverse faulting events (circles) and several strike-slip faulting events (triangles). Filled circles indicate source-process times determined from a linear inversion technique, and unfilled circles from Furumoto's method (Zhang and Kanamori, 1988). References for source parameters for strike-slip events are in the text. The solid line is an empirical relation for low-angle thrust-fault earthquakes obtained by Furumoto and Nakanishi (1983), where $M_o = 2.5 \times 10^{22} \tau^3$.

cretionary margins. In this region of Central Japan, the Philippine Sea (PHS) plate is colliding with the Eurasian plate along the Sagami and Suruga trough (Figure 5.57). Collision brings the buoyant Izu-Bonin ridge against the microcontinental margin, resulting in uplift and folding along the margins as well as internal deformation of the Izu block (Matsuda, 1978; Somerville, 1978; Shimazaki and Somerville, 1979). Collision of the Izu-Bonin ridge is the major controlling factor in the deformation of the Izu block (Le Pichon and Huchon, 1987; Ukawa, 1982, 1989; Nakamura *et al.*, 1984). Unlike the PHS, seismic activity in the Northern Gulf of Alaska is not occurring within the colliding terrane. The lack of seismicity within the Yakutat block suggests that the continental make-up of the block is more resistant to internal fragmentation. Even the Transition fault, a major structural feature, does not appear to be activated by or during this sequence. The oceanic crust in the Izu block may be weak because of the composite nature of its volcanic and volcaniclastics, while weaknesses in the oceanic crust in the Gulf of Alaska may have been inherited during the crustal formation process (Lahr *et al.*, 1988).

5.9 Conclusion

The 1987-88 Gulf of Alaska earthquakes illustrate some of the difficulties of modeling strike-slip earthquakes. Nonplanar crustal structure in the source region for Event 1 and Event 2 results in waveform complexities at shorter periods that are not well modeled for stations that lie to the north-northwest. The modeling done here also illustrates the sensitivity of the solution to variations in the focal parameters of the subevents. In all events, models using a single focal mechanism could not explain

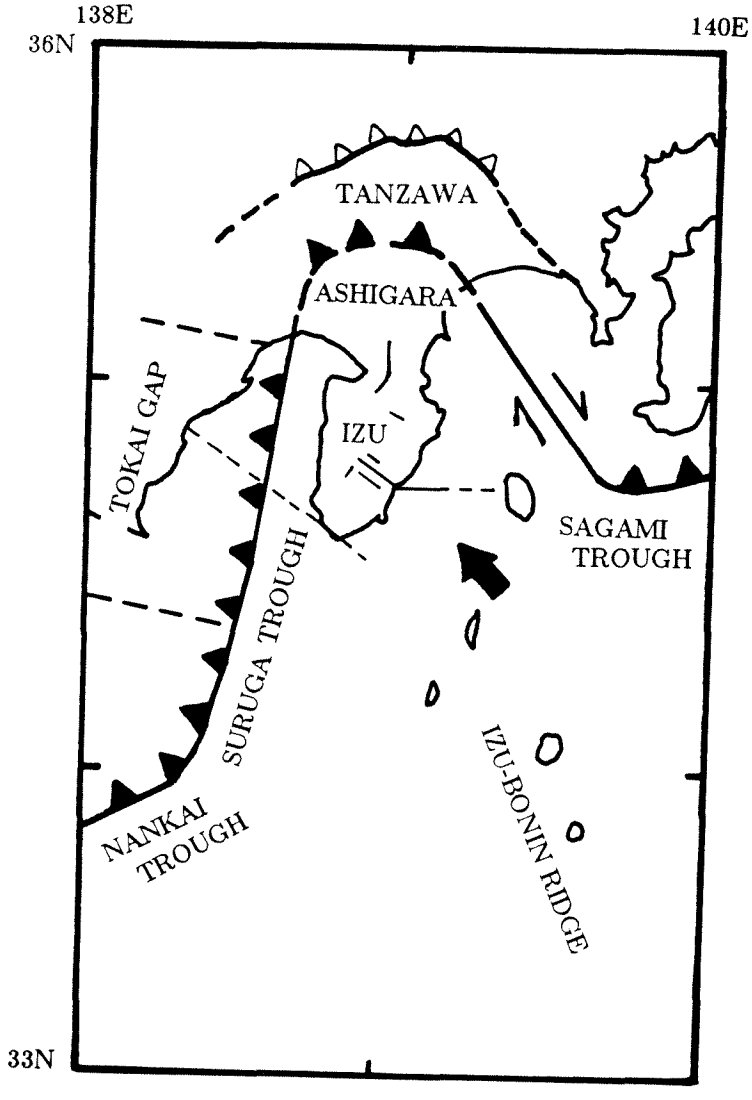

Figure 5.57: Map of tectonic features in central Japan. The solid arrow shows the relative direction of the Philippine Sea plate with respect to the Eurasian plate. The Philippine Sea plate brings the Izu-Bonin ridge and Izu block against the microcontinental margin. Collision results in subduction along the western margin and folding and uplift along the northern margin.

important features in the data. A time varying mechanism was needed to explain both the LP and WWS data. Method K showed that variations of only $\pm 10°$ are necessary and results in a nondouble-couple component typically <1%, and never more than 8%. In addition, solutions are not unique. All models result in grossly similar solutions that agree with one another within the errors of the inversion. Differences in the models illustrate that different combinations of source time, placement, size, and focal mechanisms can explain the data equally well.

All the models accounted successfully for the LP data. Complex source processes and crustal heterogeneities hindered efforts to model the WWS data robustly for Event 1 and Event 2. However, the main features in the data set were modeled. Event 3 has the simplest waveforms of the earthquakes studied and could be modeled at both bandwidths.

Source parameters agree with previous studies that indicate almost pure, vertical, NS-EW conjugate strike-slip faulting. Centroid depths are well constrained and are deeper than are observed for similar continental interplate events. These events also have shorter rupture lengths and shorter source process times than are observed for most large earthquakes. Similarities in source characteristics to another large, strike-slip, oceanic earthquake, the 1989 Macquarie Ridge earthquake, show that large oceanic strike-slip events can rupture into the upper mantle and can release more moment per unit area than similar crustal events. This may reflect the rheological difference between oceanic and continental lithosphere.

Moment release for these events did not occur smoothly along the entire aftershock length of the faults (Figure 5.52). Most of the moment release for Event 2

is confined to two regions along the fault. A large, lateral extent for Event 3 as implied by the aftershock data is not supported by the body-wave modeling results. In general, most of the moment release occurs near the epicenter and/or regions of intersecting seismic trends. This suggests that regions of structural complexities — fault zone intersections or step-overs, are regions of large moment release and are likely nucleation points for large earthquakes.

Bibliography

Abrahamson, N.A., B.A. Bolt, R.B. Darragh, J. Penzien, and Y.B. Tsai (1987). The SMART 1 accelerograph array (1980-1987): A review, *Earthquake Spectra 3,* 263–281.

Aki, K. and K.L. Larner (1970). Surface motion of a layered medium having an irregular interface due to incident plane SH waves, *J. Geophys. Res. 75,* 933–954.

Anderson, D.L. (1985). Accelerated plate tectonics, *Science 187,* 1077–1079.

Anderson, H.J. and J. Zhang (1990). Long-period seismic radiation from the May 23, 1989 Macquarie Ridge earthquake: Evidence for coseismic slip in the mantle? Submitted to *J. Geophys. Res.*

Atwater, T. and J. Severinghaus (1989). Tectonic maps of the northeast Pacific, in *The Geology of North America N, The Eastern Pacific Ocean and Hawaii,* E.L. Winterer, D.M. Hussong, and R.W. Decker, Editors, Geological Society of America, Boulder, CO, pp. 15–20.

Bard, P.-Y. and M. Bouchon (1980). The seismic response of sediment-filled valleys. Part 1. The case of incident SH waves, *Bull. Seism. Soc. Am. 70,* 1263–1286.

Bent, A.L., D.V. Helmberger, R.J. Stead, and P. Ho-Liu (1989). Waveform modeling of the November 1987 Superstition Hills earthquake, *Bull. Seism. Soc. Am. 79,* 500–514.

Bolt, B. and S.-J. Chiou (1987). Strong motion array analysis of the November 14 1986 Taiwan earthquake (Abstract), *XIX General Assembly of the International Union of Geodesy and Geophysics 1,* 303.

Boore, D.M., K.L. Larner, and K. Aki (1971). Comparison of two independent methods for the solution of wave scattering problems: response of a sedimentary basin to incident SH waves, *J. Geophys. Res 76,* 558–569.

Boyd, T.M. and J.L. Nábělek (1988). Rupture process of the Andreanof Islands earthquake of May 7, 1986, *Bull. Seism. Soc. Am. 78,* 1653–1673.

Braunmiller, J. and J. Nábělek (1990). Rupture process of the Macquarie Ridge earthquake of May 23, 1989, *Geophys. Res. Lett. 17,* 1017–1020.

Bravo, M.A., F.J. Sanchez-Sesma, and F.J. Chavez-Garcia (1988). Ground motion on stratified alluvial deposits for incident SH waves, *Bull. Seism. Soc. Am. 78,* 436–450.

Bruns, T.R. (1979). Late Cenozoic structure of the continental margin, northern Gulf of Alaska, in *The Relationship of Plate Tectonics to Alaska Geology and Resources, Proceedings, Alaska Geological Society Symposium, Anchorage, 1977,* A. Sisson, Editor, Anchorage, Alaska Geological Society, pp. 11–130.

Bruns, T.R. (1983). Model for the origin of the Yakutat block, an accreting terrane in the northern Gulf of Alaska, *Geology 11,* 718–721.

Bruns, T.R., P.R. Carlson, A.J. Stevenson, M.A. Fisher, H.F. Ryan, and D.M. Mann (1989). GLORIA images for the Gulf of Alaska and British Columbia: subduction zones, transforms, and channels (abstract), *EOS, Trans. Am. Geophys. Union 70,* 1338.

Bruns, T.R. and W.C. Schwab (1983). Structure maps and seismic stratigraphy of the Yakataga segment of the continental margin, northern Gulf of Alaska, *U.S. Geological Survey Misc. Field Studies Map MF-1424,* 4 sheets, 20 pp., scale 1:250,000.

Buland, R. and J. Taggart (1981). A mantle wave magnitude for the St. Elias, Alaska, earthquake of 28 February 1979, *Bull. Seism. Soc. Am. 71,* 1143–1159.

Butler, R., G.S. Stewart, and H. Kanamori (1979). The July 27, 1976 Tangshan, China earthquake — a complex sequence of intraplate events, *Bull. Seism. Soc. Am. 69,* 207–220.

Chen, K.C. and J.H. Wang (1986). The May 20, 1986 Hualien, Taiwan earthquake and its aftershocks, *Bull. Inst. Earth Sci., Academia Sinica 6,* 1–13.

Das, S. and B.V. Kostrov (1990). Inversion for seismic slip rate history and distribution with stabilizing constraints: application to the 1986 Andreanof Islands earthquake, *J. Geophys. Res. 95,* 6899–6913.

Deschamps, A., P. Bernard, M. Bezzeghoud, T. Monfret, and B. Romanowicz (1988). The Alaskan earthquakes of November 17 and 30, 1987: Very long period and

broad band analysis of quasi-real time teletransmitted Geoscope data, *EOS, Trans. Am. Geophys. Union 69,* 400.

Dietz, L.D. and W.L. Ellsworth (1990). The October 17, 1989 Loma Prieta, California earthquake and its aftershocks: geometry of the sequence from high-resolution locations, *Geophys. Res. Lett. 17,* 1417–1420.

Doser, D.I. and H. Kanamori (1986). Depth of seismicity in the Imperial Valley region (1977-1983) and its relationship to heat flow, crustal structure, and the October 15, 1979, earthquake, *J. Geophys. Res. 91,* 675–688.

Dziewonski, A.M., T.-A. Chou, and J.H. Woodhouse (1981). Determination of earthquake source parameters from waveform data for global and regional seismicity, *J. Geophys. Res. 86,* 2825–2852.

Dziewonski, A.M., G. Ekstrom, J.H. Woodhouse, and G. Zwart (1989a). Centroid-moment tensor solutions for October-December 1987, *Phys. Earth Planet. Inter. 54,* 10–21.

Dziewonski, A.M., G. Ekstrom, J.H. Woodhouse, and G. Zwart (1989b). Centroid-moment tensor solutions for January-March 1988, *Phys. Earth Planet. Inter. 54,* 22–32.

Dziewonski, A.M. and G. Zwart (1990). The Macquarie Ridge earthquake of 23 May 1989, *EOS, Trans. Am. Geophys. Union 70,* 1196.

Eaton, J.P., M.E. O'Neill, and J.N. Murdock (1970). Aftershocks of the 1966 Parkfield-Cholame, California, earthquake: A detailed study, *Bull. Seism. Soc. Am. 60,* 1151–1197.

Ekström, G. and B. Romanowicz (1990). The 23 May 1989 Macquarie Ridge earthquake: A very broad band analysis, *Geophys. Res. Lett 17,* 993–996.

Engdahl, E.R., S. Billington, and C. Kisslinger (1989). Teleseismically recorded seismicity before and after the May 7, 1986 Andreanof Islands, Alaska, earthquake, *J. Geophys. Res. 94,* 15481–15498.

Engeln, J.F, D.A. Wiens, and S. Stein (1986). Mechanisms and depths of Atlantic transform earthquakes, *J. Geophys. Res. 91,* 548–577.

Espinosa, A.F., R. Husid, and A. Quesada (1976). Intensity distribution and source parameters from field observations. The Guatemalan earthquake of February 4, 1976, a preliminary report, *U.S. Geol. Surv. Prof. Pap. 1002,* 52–66.

Frankel, A. and L. Wennerberg (1989). Rupture process of the M_S 6.6 Superstition Hills earthquake determined from strong-motion recordings: application of tomographic source inversion, *Bull. Seism. Soc. Am. 79,* 515–541.

Fuis, G.S., W.D. Mooney, J.H. Healy, G.A. McMechan, and W.J. Lutter (1982). Crustal structure of the Imperial Valley Region, in *The Imperial Valley, California, earthquake of October 15, 1979, U.S. Geol. Surv. Prof. Pap. 1254,* 25–50.

Furumoto, M. and I. Nakanishi (1983). Source times and scaling relations of large earthquakes, *J. Geophys. Res. 88,* 2191–2198.

Given, D.D. (1986). Master event relocations of the North Palm Springs earthquake sequence of July 1986 (abstract), *EOS, Trans. Am. Geophys. Union 67,* 1089.

Goetze, C. and B. Evans (1979). Stress and temperature in the bending lithosphere as constrained by experimental rock mechanics, *Geophys. J. R. Astron. Soc. 59,* 463–478.

Gutenburg, B. and C.F. Richter (1954). *Seismicity of the Earth and Associated Phenomena,* Princeton Univ. Press, Princeton, N.J., 310 pp.

Hanks, T.C. and C.R. Allen (1989). The Elmore Ranch and Superstition Hills earthquakes of 24 November 1987: Introduction to the special issue, *Bull. Seism. Soc. Am. 79,* 231–238.

Hartzell, S.H. and T.H. Heaton (1986). Rupture history of the 1984 Morgan Hill, California, earthquake from the inversion of strong motion records, *Bull. Seism. Soc. Am. 76,* 649–674.

Herrin, E. (1968). Introduction to '1968 Seismological Tables for P Phases', *Bull. Seism. Soc. Am. 58,* 1193–1241.

Ho, C.S. (1986). A synthesis of the geologic evolution of Taiwan, *Tectonophysics 125,* 1–16.

Houston, H. (1986). Source characteristics of large earthquakes at short periods, *Ph.D. Dissertation,* California Institute of Technology, Pasadena, California, 129 pp.

Houston, H. (1990). Broadband source spectrum, seismic energy, and stress drop of the 1989 Macquarie Ridge earthquake, *Geophys. Res. Lett. 17,* 1021–1024.

Houston, H. and E.R. Engdahl (1989). A comparison of the spatio-temporal distribution of moment release for the 1986 Andreanof Islands earthquake with relocated seismicity, *Geophys. Res. Lett. 16,* 1421–1424.

Houston, H. and H. Kanamori (1986). Source spectra of great earthquakes: Teleseismic constraints on rupture process and strong motion, *Bull. Seism. Soc. Am. 76,* 19–42.

Houston, H. and H. Kanamori (1987). Comparison of strong-motion spectra with teleseismic spectra for large subduction-zone earthquakes, *Bull. Seism. Soc. Am. 80,* 913-934.

Houston, H. and H. Kanamori (1990). Comparison of strong-motion spectra with teleseismic spectra for three magnitude 8 subduction zone earthquakes, *Bull. Seism. Soc. Am. 80,* 913–934.

Hwang, L.J. and H. Kanamori (1986). Of the May 7, 1986 Andreanof Islands Earthquake Source Parameters, *Geophys. Res. Lett. 13,* 1426–1429.

Hwang, L.J. and H. Kanamori (1987). Correction to 'Source parameters of the May 7, 1986 Andreanof Islands earthquake,' by Lorraine J. Hwang and H. Kanamori, *Geophys. Res. Lett 14,* 170.

Hwang, L.J. and H. Kanamori (1989). Teleseismic and strong-motion source spectra from two earthquakes in eastern Taiwan, *Bull. Seism. Soc. Am. 79,* 935–944.

Hwang, L.J., H. Magistrale, and H. Kanamori (1990). Teleseismic source parameters and rupture characteristics of the 24 November 1987, Superstition Hills earthquake, *Bull. Seism. Soc. Am. 80,* 43–56.

Jacob, K.H. (1984). Estimates of long-term probabilities for great earthquakes in the Aleutians, *Geophys. Res. Lett. 11,* 295–298.

Johnson, C.E. and D.M. Hadley (1976). Tectonic implications of the Brawley earthquake swarm, Imperial Valley, California, January 1975, *Bull. Seism. Soc. Am. 66,* 1131–1144.

Johnson, C.E. and L.K. Hutton (1982). Aftershocks and preearthquake seismicity, in *The Imperial Valley, California, Earthquake of October 15, 1979, U.S. Geol. Surv. Profess. Paper 1254,* 59–76.

Jones, L.M., L.K. Hutton , D.D. Given, and C.R. Allen (1986). The North Palm Springs, California earthquake sequence of July 1986, *Bull. Seism. Soc. Am. 76,* 1830–1837.

Joyner, W.B. (1975). A method for calculating nonlinear seismic response in two dimensions, *Bull. Seism. Soc. Am. 65,* 1337–1357.

Joyner, W.B. and A.T.F. Chen (1975). Calculation of nonlinear ground motion response in earthquakes, *Bull. Seism. Soc. Am. 65,* 1315–1336.

Kanamori, H. (1977). The energy release in great earthquakes, *J. Geophys. Res. 82,* 2981–2987.

Kanamori, H. and D.L. Anderson (1975). Theoretical basis of some empirical relations in seismology, *Bull. Seism. Soc. Am. 65,* 1073–1095.

Kanamori, H. and J.W. Given (1981). Use of long-period surface waves for rapid determination of earthquake source parameters, *Phys. Earth Planet. Inter. 27,* 8–31.

Kanamori, H. and K. Satake (1990). Broadband study of the 1989 Loma Prieta earthquake, *Geophys. Res. Lett. 17,* 1179–1182.

Kanamori, H. and G.S. Stewart (1978). Seismological aspects of the Guatemala earthquake of February 4, 1976, *J. Geophys. Res. 83,* 3427–3434.

Kawakatsu H. (1989). Centroid single force inversion of seismic waves generated by landslides, *J. Geophys. Res. 94,* 12363–12370.

Kedar, S. and T. Tanimoto (1990). Moment of the Macquarie Island earthquake from free oscillation data, *EOS, Trans. Am. Geophys. Union 71,* 558.

Kikuchi, M. and Y. Fukao (1985). Iterative deconvolution of complex body waves from great earthquakes — the Tokachi-Oki earthquake of 1968, *Phys. Earth Planet. Inter. 37,* 235–248.

Kikuchi, M. and H. Kanamori (1982). Inversion of complex body waves, *Bull. Seism. Soc. Am. 72,* 491–506.

Kikuchi, M. and H. Kanamori (1990). Inversion of complex body waves - III, submitted to *Bull. Seism. Soc. Am.*

King, J.L. and B.E. Tucker (1984). Observed variations of earthquake motion across a sediment-filled valley, *Bull. Seism. Soc. Am. 74,* 137–151.

Kisslinger, C. (1985). Seismicity patterns in the Adak Seismic Zone and the short term outlook for a major earthquake, in *Minutes of the National Earthquake Prediction Council, September 8 & 9, Anchorage, Alaska,* C.F. Shearer, Editor, U.S. Geological Survey Open File Report, 86–92, 120–134.

Knopoff, L. (1958). Energy release in earthquakes, *Geophys. J. 1,* 44–52.

Kohler, W.M. and G.S. Fuis (1986). Travel-time, time-term, and basement depth maps for the Imperial Valley Region, California, from explosions, *Bull. Seism. Soc. Am. 76,* 1289–1303.

Lahr, J.C., R.A. Page, C.D. Stephens, and D.H. Christensen (1988). Unusual earthquakes in the Gulf of Alaska and fragmentation of the Pacific plate, *Geophys. Res. Lett. 15,* 1483–1486.

Lahr, J.C. and G. Plafker (1980). Holocene Pacific-North American plate interaction in southern Alaska: Implications for the Yakataga seismic gap, *Geology 8,* 483–486.

Langston, C.A. (1977). The effect of planar dipping structure on source and receiver responses for constant ray parameter, *Bull. Seism. Soc. Am. 67,* 1029–1050.

Langston, C.A. and D.V. Helmberger (1975). A procedure for modelling shallow dislocation sources, *Geophys. J. R. Astron. Soc. 42,* 117–130.

Le Pichon, X. and P. Huchon (1987). Central Japan triple junction revisited, *Tectonics 6,* 35–45.

Leeds, A.K., E.G. Kausel, and L. Knopoff (1974). Variations of upper mantle structure under the Pacific Ocean, *Science 186,* 141–143.

Li, V.C. and C. Kisslinger (1984/85). Stress transfer and nonlinear stress accumulation of subduction-type plate boundaries — Applications to the Aleutians, *Pure Appl. Geophys. 122,* 812–830.

Liaw, Z.S., C. Wang, and Y.T. Yeh (1986). A study of aftershocks of the 20 May 1986 Hualien earthquakes, *Bull. Inst. Earth Sci., Academia Sinica 6,* 15–27.

Lindh, A. and D.M. Boore (1974). The relation of the Parkfield foreshocks to the initiation and extent of rupture, *Earthquake Notes 45,* 54.

Lyzenga, G.A., A. Raefsky, and B.H. Hager (1986) Time-predictable earthquake recurrence at subduction zones? (abstract), *EOS, Trans. Am. Geophys. Union 67,* 904.

Magistrale, H., L. Jones, and H. Kanamori (1989). The Superstition Hills, California, earthquakes of 24 November, 1987, *Bull. Seism. Soc. Am. 79,* 239–251.

Matsuda, T. (1978). Collision of the Izu-Bonin arc with central Honshu: Cenozoic tectonics of the Fossa Magna, Japan, in *Geodynamics of the Western Pacific,* S. Uyeda, R.W. Murphy, and K. Kobayashi, Editors, Japan Scientific Societies Press, 409–421.

McCann, W.R., S.P. Nishenko, L.R. Sykes, and J. Krause (1979). Seismic gaps and plate tectonics: Seismic potential for major plate boundaries, *Pure Appl. Geophys. 117*, 1082–1147.

McCann, W.R., O.J. Perez, and L.R. Sykes (1980). Yakataga Gap, Alaska: Seismic history and earthquake potential, *Science 207,* 1309–1314.

Mendoza, C. and S.H. Hartzell (1988). Aftershock patterns and main shock faulting, *Bull. Seism. Soc. Am. 78,* 1438–1449.

Minster, J.B. and T.H. Jordan (1978). Present-day plate motions, *J. Geophys. Res. 83,* 5331–5354.

Mogi, K. (1968). Development of aftershock areas of great earthquakes, *Bull. Earthquake Res. Inst. Tokyo Univ. 46,* 175–203.

Nábělek, J. (1984). Determination of earthquake source parameters from inversion of body waves, *Ph. D. Dissertation,* Massachusetts Institute of Technology, 360 pp.

Nábělek, J. (1985). Geometry and mechanism of faulting of the 1980 El Asnam, Algeria, earthquake from inversion of teleseismic body waves and comparison with field observations, *J. Geophys. Res. 90,* 12713–12728.

Nakamura, K., K. Shimazaki, and N. Yonekura (1984). Subduction, bending and eduction. Present and Quaternary tectonics of the northern border of the Philippine Sea plate, *Bull. Soc. Geol. France 26,* 221–243.

Parsons, B. and J.G. Sclater (1977). An analysis of the variation of ocean floor bathymetry and heat flow with age, *J. Geophys. Res. 82,* 803–827.

Perez, O.J. and K.H. Jacob (1980). Tectonic model and seismic potential of the eastern Gulf of Alaska and Yakataga seismic gap, *J. Geophys. Res. 85,* 7132–7150.

Plafker, G. (1969). Tectonics of the March 27, 1964 Alaska earthquake, *U.S. Geol. Surv. Prof. Pap. 543-I,* 74 pp.

Plafker, G. (1971). Possible future petroleum resources of Pacific margin Tertiary basin, Alaska, in *Future Petroleum Provinces of the United States — Their Geology and Potential,* I.H. Cram, Editor, Am. Assoc. Pet. Geol. Mem. 15, v.1, pp. 120–135.

Plafker, G. (1976). Tectonic aspects of the Guatemala earthquake of 4 February 1976, *Science 193,* 1201–1208.

Plafker, G. (1983). The Yakutat block: An actively accreting tectonostratigraphic terrane in southern Alaska, *Geol. Soc. Am. Abs. with Prog. 15,* 406.

Plafker, G. (1987). Regional geology and petroleum potential of the northern Gulf of Alaska margin, in *Circum-Pacific Council for Energy and Mineral Resources, Earth Science Series, v. 6,* Houston, Texas, pp. 229–268.

Plafker, G., T. Hudson, T. Bruns, and M. Rubin (1978). Late Quaternary offsets along the Fairweather fault and crustal plate interactions in southern Alaska, *Can. J. Earth Sci. 15,* 805–816.

Plafker, G., G.R. Winkler, W.L Coonrad, and G. Claypool (1980). Preliminary geology for the continental slope adjacent to OCS Lease sale 55, eastern Gulf of Alaska: Petroleum resource implications, *U.S. Geol. Surv. Open File Rep. 80–1089,* 72 pp.

Satake, K. and H. Kanamori (1990). Fault parameters and tsunami excitation of the May 23, 1989, Macquarie ridge earthquake, *Geophys. Res. Lett. 17,* 997–1000.

Schwab, W.C., T.R. Bruns, and R. von Huene (1980). Structural interpretation of magnetic lineaments in the northern Gulf of Alaska, *U.S. Geol. Surv. Misc. Field Studies Map MF-1245,* scale 1:1,500,000.

Schwartz, S.Y., J.W. Dewey, and T. Lay (1989). Influence of fault plane heterogeneity on the seismic behavior in the Southern Kurile Islands Arc, *J. Geophys. Res. 94,* 5637–5649.

Sharp, R.V., K.E. Budding, J. Boatwright, M.J. Ader, M.G. Bonilla, M.M. Clark, T.E. Fumal, K.K. Harms, J.J. Lienkaemper, D.M. Morton, B.J. O'Neill, C.L. Ostergren, D.J. Ponti, M.J. Rymer, J.L. Saxton, and J.D. Sims (1989). Surface faulting along the Superstition Hills fault zone and nearby faults associated with the earthquakes of 24 November 1987, *Bull. Seism. Soc. Am. 79,* 252–281.

Shimazaki, K. and P. Somerville (1979). Static and dynamic parameters of the Izu-Oshima, Japan earthquake of January 14, 1978, *Bull. Sesm. Soc. Am. 69,* 1343–1378.

Sipkin, S.A. (1989). Moment-tensor solutions for the 24 November 1987 Superstition Hills, California earthquake, *Bull. Seism. Soc. Am. 79,* 493–499.

Somerville, P. (1978). The accommodation of plate collision by deformation in the Izu block, Japan, *Bull. Earthq. Res. Inst. 53,* 629–648.

Stonely, R. (1967). The structural development of the Gulf of Alaska sedimentary province in southern Alaska, *Geological Society of London Quarterly Journal 123*, 25–27.

Sykes, L.R. (1971). Aftershock zones of great earthquakes, seismicity gaps, and earthquake prediction for Alaska and the Aleutians, *J. Geophys. Res. 76,* 8021–8041.

Sykes, L.R. (1978). Intraplate seismicity, reactivation of preexisting zones of weakness, alkaline magmatism and other tectonism postdating continental fragmentation, *Rev. Geophys. Space Phys. 16,* 621–668.

Sykes, L.R., J.B. Kisslinger, L. House, J.N. Davies, and K.H. Jacob (1981). Rupture zones and repeat times of great earthquakes along the Alaska-Aleutian arc, 1784–1980, in *Earthquake Prediction, An International Review; Maurice Ewing Series, 4,* D.W. Simpson and P.B. Richards, Editors, American Geophysical Union, Washington, D.C., pp. 73–80.

Tarr, R.S. and L. Martin (1912). The earthquakes at Yakutat Bay, Alaska in September 1899, *U.S. Geol. Surv. Prof. Paper 69*, 135 pp.

Tichelaar, B.W. and L.J. Ruff (1990). Rupture process and stress-drop of the great 1989 Macquarie Ridge earthquake, *Geophys. Res. Lett. 17,* 1001–1004.

Tocher, D. (1960). The Alaska earthquake of July 10, 1958: movement on the Fairweather fault and field investigation of southern epicentral region, *Bull. Seism. Soc. Am. 50*, 267–292.

Tsai, Y.B., T.L. Teng, J.M. Chiu, and H.L. Liu (1977). Tectonic implications of the seismicity in the Taiwan region, *Mem. Geol. Soc. China 2,* 13–41.

Ukawa, M. (1982). Lateral stretching of the Philippine Sea plate subducting along the Nankai-Suruga Trough, *Tectonics 1*, 543–571.

Ukawa, M. (1989). Collision and fan-shaped compressional stress pattern around the Izu Block at the northern edge of the Philippine Sea Plate (abstract), *EOS, Trans. Am. Geophys. Union 70,* 470.

Vidale, J.E. and D.V. Helmberger (1988). Elastic finite-difference modeling of the 1971 San Fernando, California earthquake, *Bull. Seism. Soc. Am. 78,* 122–141.

von Huene, R., G.G. Shor, Jr., and J. Wageman (1979). Continental margins of the eastern Gulf of Alaska and boundaries of tectonic plates, *Mem. Am. Assoc. Petrol. Geol. 29,* 272–290.

Wald, D.J., D.V. Helmberger, and S.H. Hartzell (1990). Rupture process of the 1987 Superstition Hills earthquake from the inversion of strong motion data, *Bull. Seism. Soc. Am. 80*, 1079–1098.

Wald, D.J. and P.G. Somerville (1988). Simulation of accelerograms of the 1987 Superstition Hills earthquake sequence, paper presented at Seismol. Soc. Am. meeting, Honolulu, 24–27 May 1988.

Watts, A.B., J.H. Bodine, and M.S. Steckler (1980). Observations of flexure and the state of stress in the oceanic lithosphere, *J. Geophys. Res. 85,* 6369–6376.

Wiens, D.A. and S. Stein (1983). Age dependence of oceanic intraplate seismicity and implications for lithospheric evolution, *J. Geophys. Res. 88,* 6455–6468.

Wiens, D.A. and S. Stein (1984). Intraplate seismicity and stresses in young oceanic lithosphere, *J. Geophys. Res. 89,* 11442–11464.

Williams, P.L. and H.W. Magistrale (1989). Slip along the Superstition Hills fault associated with the 24 November 1987 Superstition Hills, California, earthquake, *Bull. Seism. Soc. Am. 79,* 390–410.

Wilson, D.S. (1986). A kinematic model for the Gorda Deformation Zone as a diffuse southern boundary of the Juan de Fuca plate, *J. Geophys. Res. 91,* 10259–10269.

Wong, T.L. and M.D. Trifunac (1974). Surface motion of a semi-elliptical alluvial valley for incident plane SH waves, *Bull. Seism. Soc. Am. 64,* 1389–1408.

Yeh, Y.T., C.L. Tsai, K.C. Chen, and K.L. Wen (1988). An investigation of two destructive Hualien earthquakes in 1986 in the Taiwan area, *Bull. Inst. Earth Sci. Academia Sinica,* in press.

Young, C.J., T. Lay, and C.S. Lynnes (1989). Rupture of the 4 February 1976 Guatemalan earthquake, *Bull. Seism. Soc. Am. 79,* 670–689.

Zhang, J. and H. Kanamori (1988). Source finiteness of large earthquakes measured from long-period Rayleigh waves, *Phys. Earth Planet. Inter. 52,* 56–84.

Zhuo, Y. and H. Kanamori (1987). Regional variation of the short-period (1 to 10 second) source spectrum, *Bull. Seism. Soc. Am. 77,* 514–529.